Reduced-Complexity Modeling for Control and Nonlinear Analysis of Transitional Flows

A DISSERTATION
SUBMITTED TO THE FACULTY OF THE GRADUATE SCHOOL
OF THE UNIVERSITY OF MINNESOTA
BY

Aniketh Kalur

IN PARTIAL FULFILLMENT OF THE REQUIREMENTS
FOR THE DEGREE OF
DOCTOR OF PHILOSOPHY

Maziar S. Hemati

August, 2021

© Aniketh Kalur 2021
ALL RIGHTS RESERVED

Acknowledgements

At the outset, I would like to thank my adviser, Prof. Maziar S. Hemati; without him, this work wouldn't exist. Prof. Hemati let me fly with my ideas, often reeling me in when I deviated from course, calmly guided me, and always had my back during turbulent times. Throughout these years, he challenged me scientifically, provided critical scientific feedback, encouragement, and valuable life and research lessons which I will carry along.

I would also like to thank Prof. Peter Seiler for his guidance, patience, engaging discussions, and most importantly, for setting a high standard, which I will always aspire to reach. I would also like to thank Prof. Andrew Lamperski and Prof. Krishnan Mahesh for the exciting discussions that came from being part of my committee. I am honored and will be forever grateful.

During these beautiful years, I was fortunate to have the company of some of the most brilliant people at work and in life. I want to acknowledge Aditya Madabhushi for his time, patience, and effort. A big thanks to him for engaging me in impromptu discussions over walks, dinners, and drinks and for the countless proofs he was always ready to discuss with me. A special thanks to Dr. Mengying Wang, Dr. Huaijin Yao, and Dr. Yiyang Sun for all the fruitful whiteboard discussions in the lab. I would also like to thank my current lab mates Talha Mushtaq, Nick Conlin, Johnathan Smith, and Leonid Heide for the academically stimulating environment they helped create. A warm thanks to John Jackson, Dr. Praveen Kumar, and Dr. Narendra Singh for discussing life, work, and philosophy during our regular coffee walk on campus and other get together. I want to thank Dr. Kerry Sun for his company and attending many practice talks and seminars throughout these years. I would also like to thank Dr. Sreevatsa Anantharamu for stimulating the discussion on POD, DMD, and related methods.

Many of my friends have made this journey enjoyable and unforgettable—the folks in Minneapolis, Chicago, Boston, and India—you all know who you are. I want to acknowledge the river Mississippi for keeping me company in all my runs; it was the melodic sound of water flowing that energized me and always brought me back to equilibrium.

Lastly, but importantly I would like to acknowledge my family for their support and my wife Kavya for sitting through numerous practice talks and teaching me the science of making "good" presentations. I want to acknowledge both my family and Kavya's belief that Kavya's effort led to the successful completion of this work!

Dedication

To,

Dadu *for planting the seed of curiosity and leading by example*,

Amma, Nanna and Animesh *for always believing*,

Kavya *for teaching me to live and not just exist*,

You *since you dared to read.....all the best!*

Abstract

The predominant causes for transition to turbulence in wall-bounded shear flows are transient energy growth and nonlinear interactions resulting from the governing linear and nonlinear dynamics. This work addresses both the problem of (i) minimizing transient energy growth (TEG) arising from non-modal dynamics and (ii) accounting for nonlinear interactions while performing stability analysis. This work aims to delay the transition and perform analysis to predict stability boundaries for the onset of turbulence—both with the help of reduced-complexity modeling.

In part I, the first problem is addressed by developing control-oriented reduced-order models (COROMs) for designing controllers that minimize maximum transient energy growth (MTEG). The COROMs are developed on the linearized channel flow system using proper orthogonal decomposition and balanced truncation in conjunction. The COROMs enable the development of MTEG minimizing controllers, which otherwise were intractable due to the large dimension of the channel flow system. The performance of the designed controllers is investigated in response to optimal perturbations.

In part II, the second problem is addressed by accounting for the nonlinear interactions for stability analysis. Typically in fluid flows, modeling the behaviour of nonlinear interactions exactly is notoriously difficult. Here, instead of using the exact nonlinear dynamics, the input-output properties of the nonlinearity are written as quadratic constraints. The stability analysis of only the linear dynamics is subject to the aforementioned quadratic constraints resulting in linear matrix inequalities (LMIs). These LMIs enable stability analysis by estimating the region of attraction and the largest permissible perturbation in the nonlinear setting. The utility of the proposed framework is demonstrated on nonlinear low-order models of transitional flows such as the Couette flow. Further, two algorithms are developed, both these algorithms enable solving LMIs with quadratic constraints such that the predicted stability margins can be further improved. Finally, the application of the proposed framework in analyzing the stability of reduced-order viscous Burgers equations, is demonstrated. The viscous Burgers equation is a canonical yet simple model to demonstrate the applicability of the proposed framework. Since the viscous Burgers system has a quadratic convective nonlinearity

which introduces transition and change in stability, similar to the Navier-Stokes. The stability of the Burgers equation is studied using the proposed framework and its results are benchmarked against methods like the sum-of-squares method.

Contents

List of Tables

List of Figures

Chapter 1

Introduction

1.1 Introduction

Interaction between engineered systems and fluid flows (both liquid and gases) is ubiquitous in the world around us, e.g., pipelines, cars, ships, airplanes, wind turbines, medical devices, etc. The human civilization has now relied on these engineered systems for meeting essential needs such as energy generation, transportation, and health monitoring. With an increase in dependency on systems that interact with fluids, it is paramount to understand how these systems are affected by changes in the fluid flows regime.

Traditionally fluid flow regimes are characterized as laminar, transitional, or turbulent. A characteristic of the laminar flow regime is that the the fluid particle undergo smooth passage with little or no mixing with adjacent layers. While in a transitional flow, we witness the start of velocity fluctuations and the start of mixing, and in a fully turbulent flow regime, the velocity fluctuations are large and the fluid undergoes chaotic mixing. These flow regimes can be seen by observing water flowing from a tap; when the tap is appropriately open, the water flows smoothly in a steady stream (almost looking like glass); this is the laminar flow regime. When the tap is further opened, to increase the flow rate, we see the water start to oscillate back and forth (sprinkle) intermittently, breaking the glass-like flow—this is the transitional regime. Further increasing the flow rate causes a jet of water sprinkling all over while undergoing chaotic mixing on many scales; this is the turbulent flow regime. These regimes are characterized based on a

dimensionless parameter called Reynolds number (Re), Re is the ratio of inertial forces to viscosity. These flow regimes are also observed in everyday engineering systems on large and small scales alike.

In nature, turbulent flows are the rule, and laminar flows are rare, as fluid flows interacting with an object easily transition to turbulence due to friction or other environmental disturbances. It has been shown that the turbulent flow regime has detrimental effects on engineering systems as it greatly increases skin friction drag [SH01]. In subsonic transport aircraft, skin friction drag contributes to 50% of the drag encountered [TRS90], leading to increased operational and maintenance costs. Given the ubiquitous existence and nature of turbulent flows, it is important to control the fluid flow to prevent transition to turbulence. The main motivation of this work is to enable control and analyze stability of fluid flows.

Preventing transition through design or configuration changes is referred to as *flow control*. A precursor to flow control is to have the ability to understand how the transition occurs, and this problem directly relates to studying the stability of fluid flows and is known as *stability analysis*.

Flow control: is the ability to impart change in fluid flow regimes through configuration or design changes, to obtain benefits such as drag reduction, noise reduction, increasing lift, etc. Control of fluid flows can be done in one of three ways [Hem06], namely,

1. *Passive flow control* involves changing the flow configuration by either reshaping wings/lift surfaces, adding riblets, etc. These methods do not require the addition of external energy in the flow and are appropriately called passive flow control methods. Due to their passive nature, these control methods are easy to implement, but they cannot react to fluid flow changes.

2. *Open-loop active flow control* requires energy in the system using actuators like fluid injectors, plasma actuators, etc. This flow control method typically operates in an open-loop fashion by affecting change using actuators to impart energy in the flow. However, the control method does not have the ability to react to changing flows.

3. *Feedback flow control* is a type of active flow control that uses sensor data in

feedback to react to changes in the flow. These control methods are typically more expensive and complicated to implement as they need the information of the flow state to implement desired changes effectively. In this work, only feedback flow control methods will be used, which will be the focus of chapter 3.

Stability Analysis: The dynamical evolution of fluid flows are governed by infinite-dimensional partial differential equations (PDEs) called the Navier-Stokes equations (NSE). These equations are notoriously difficult to study primarily due to their large dimensional nature and nonlinear behavior. Therefore, stability analysis is the study of the behavior of the NSE and their response to disturbances, which provides information on how and when the flow will change from laminar to turbulent.

Stability analysis includes identifying stability boundaries of the governing system, and this may include (but is not restricted to) identifying the envelope in which system trajectories will remain around an equilibrium point, identifying the size of the perturbations that can destabilize the system, and estimating the possible energy growth in the system. We will see in chapters 4 and 5, as we estimate the above-mentioned parameters to analyze the stability of nonlinear transitional flows.

1.2 Motivation and Challenges

To study stability of the fluid flows and performing feedback flow control effectively is the main motivation of this thesis. To achieve both these tasks is non-trivial since the NSE are infinite-dimensional and nonlinear partial differential equations. Therefore, analyzing stability and controlling fluid flows remains an open area of research due to the challenges involved. The NSE, in very few cases, has an analytical solution, and hence these equations are typically solved using computational fluid dynamics (CFD) tools such as direct numerical simulations (DNS). The DNS discretizes the domain of interest up to the desired resolution and provides information on velocity, temperature, pressure, and other quantities of interest at every point in the domain while resolving small and large scale structures in the flow. The DNS requires expensive computational resources like supercomputers running for a long duration to resolve the flow accurately. However, using DNS for control and stability analysis of fluid flows is not reasonable due to the computational expense involved. Hence, alternate efficient methods must be

identified to enable the analysis and control of fluid flows.

This work aims to address the two main challenges associated with analyzing and controlling flows governed by the NSE, i.e., the dimensionality and nonlinearity of the NSE, and hence the thesis is organized as two parts. In the first part of the thesis, we address dimensionality using reduced-order modeling such that effective flow control can be performed (see chapter 3 for more details). The second part of the thesis deals with accounting for the complex nonlinear interactions using a reduced-complexity framework which enables stability analysis while accounting for the nonlinear terms without their full-complexity (see chapters 4, 5). The next few sections, briefly introduces the concept of reduced-order modeling and reduced-complexity modeling while placing the context of the current work in the literature.

1.3 Challenge 1: Dimensionality

The NSE are PDEs; when they are discretized in space and time, they typically result in high-dimensional systems. Solving the resulting system is computationally intractable in most cases as DNS generates data in order of a few 100 Gigabytes to a few 100 Terra bytes, depending on the applications and flow geometry. This large dimensionality gets even more challenging for applications of feedback flow control, as it is unrealistic to expect to use models obtained from DNS for feedback control. However, early on, it was observed that the flow phenomena could be realistically represented using certain dominating modes instead of every mode [Lum67]. The main idea was to leverage the use of underlying structures to obtain an equivalent low-dimensional representation. This observation leads to the burgeoning field of reduced-order modeling for fluid flow applications.

1.3.1 Reduced-order modeling

The idea behind reduced-order modeling (ROM) is to reduce the degrees of freedom of a large dimensional system; the large dimensional system is often referred to as a full-order model (FOM). The ROM with a reduced number of degrees of freedom should capture the dynamics of the FOM. It is also important to note that apart from a small approximation error in the dynamics, the ROM should typically also satisfy

important properties that are characteristic to the FOM. These properties could include conservation of quantities, stability, passivity, etc. The ROM is typically obtained mathematically, using an alternate set of basis to represent the system, hoping that the alternate basis requires fewer states to represent the dynamics of the FOM while satisfying its intrinsic properties.

The proper orthogonal decomposition (POD) is one such basis often used to obtain ROMs in fluid systems. POD was initially introduced to the fluid dynamics community by Lumley in 1967, where a random vector representing turbulent fluid flows was decomposed into a deterministic basis that captured the kinetic energy accurately—the POD basis [Lum67]. Apart from capturing the most energetically relevant modes, the POD basis is also attractive because it is robust while dealing with nonlinearities while being a linear operation. An excellent overview of POD analysis can be found in [BHL93]. As with every method, the POD has its own shortcoming. Since the modes selected by the POD procedure are shown to be the most energetic (kinetic) modes in an average sense, these modes are not typically the most dynamically relevant.

One ROM method that can capture dynamically relevant modes is based on the respective modes' slow-fast decomposition (based on time scales). This method retains the most relevant slowly decaying modes while modes corresponding to the fast modes are neglected. As expected, the slow-fast decomposition tends to approximate the system dynamics well. However, it fails to capture the input-output dynamics of the system, which are especially important in cases where control is being used. To overcome this drawback, a method proposed to accurately capture input-output properties of the system was introduced by Moore [Moo81]. The author proposes to use balance truncation—which uses information of both inputs and outputs before discarding system states. Balance truncation uses a similarity transform to transfer the system into a coordinate system where the most controllable and observable states are retained, proving to be an effective ROM method for control applications. An additional challenge with balanced truncation is that even though it is readily applicable for moderate size systems, the method becomes prohibitively expensive for large-scale systems such as fluid flows, where the dimensions of the states are typically of the order of 10^3 or more.

To enable balanced model reduction for large-scale systems, Willcox and Peraire provide a method to obtain balanced model reduction via the POD [WP02]. The authors

in [WP02] propose using the POD kernel to obtain an approximation of the associated Grammians, thereby enabling obtaining balancing transformation for large systems with multiple inputs. This method is demonstrated on a two-dimensional NACA 0012 airfoil operating in unsteady motion. However, for fluid systems with many outputs, the balanced model reduction via POD becomes intractable. To overcome this issue, Rowley in [Row05] proposes calculating the balancing transformation without explicitly computing the aforementioned Grammians. Rowley proposes the method of output projection onto POD modes; to facilitate calculation of the balancing transformations for systems with a large number of outputs; the efficacy of this method is demonstrated on the linearized channel flow problem.

Lastly, we briefly discuss the dynamic mode decomposition (DMD) algorithm due to the promise of data-driven reduced-order modeling. The DMD enables the decomposition of time-resolved data into Spatio-temporal modes. The DMD enables obtaining a best-fit linear operator that approximates the infinite-dimensional Koopman operator, enabling approximation of a finite-dimensional nonlinear system without explicit linearization. The DMD method has shown promise in data-driven modeling and approximation for fluid systems like cylinder flow [HWR14, Tu13], jets in crossflow [RMB$^+$09], screeching supersonic jet [JSN14].

In the context of wall-bounded shear flows, which is the fluid flow model of interest in this work, it is well established that the linear part of the NSE contributes to non-modal amplification of perturbations leading to energy growth on transient time scales [SH01, TE05]. In part one of this work, the first challenge of dimensionality reduction of fluid flows is addressed by introducing control-oriented reduced-order models (COROM) for developing special controllers—that specifically minimize the non-modal energy growth in wall-bounded shear flows. The work proposed here uses concepts from balanced model reduction and output projection to develop reduced-order models that can retain the energy of the original system even after the states are truncated. The COROM detailed in chapter 3 enables developing controllers that minimize non-modal amplification of energy in the linearized channel flow system; developing these feedback control methods would typically not be possible due to the large dimensionality of the channel flow system. Lastly, DNS simulations show that even though the controllers minimize energy growth, secondary instabilities caused by the nonlinear terms will lead the system to

transition. Hence it is also important to account for nonlinear effects in the system. This leads to the second challenge and will be addressed in the next section.

1.4 Challenge 2: Nonlinearity

The NSE has linear and nonlinear terms; the nonlinear term arises due to convective acceleration due to a change in velocity over space. These nonlinear terms are responsible for the transport phenomena observed in fluid flows, where energy is transported between various scales. Most convective flows, regardless of being turbulent or not, will contain the convective nonlinear terms. Little is known about these nonlinear terms, even for simple geometries, especially at high Re. The TEG mechanism drives the system trajectories to the edge of the stability, after which secondary instabilities, due to the nonlinearity, drive the system to instability. Therefore, a simple linear analysis (where nonlinear terms are neglected) tends to over predict the critical Re_c for transition [SH01, SB14, RH93a] often failing in agreement with results obtained from experiments and DNS. To completely understand the transition scenarios, the nonlinear terms have to be accounted for.

The interplay between the linear and nonlinear terms has often been modeled as a feedback mechanism, where the nonlinear block feeds into the linear block and vice versa; this is also known as a Lur'e decomposition in robust control literature [SP05]. Many works in the literature have leveraged this feedback mechanism (shown in Fig. 1.1) to study the nonlinear NSE. One such method is the Resolvent analysis framework [SM13, MS10, JB05], which treats the nonlinear terms as an implicit forcing on the linear dynamics. This perspective greatly simplifies the resulting analysis problem, as only the linear system, described by the input-output properties of the linear resolvent operator, needs to be analyzed. The resolvent analysis provides information on how fluctuations in a time-averaged flow are attenuated or amplified from nonlinear effects within the context of turbulent flows. Resolvent analysis has been successfully employed to study various flows[THB$^+$19], including pipe flows [SM13], open cavity flows [SLC$^+$19], and flows over riblets [CL19].

Related methods have been proposed to account for the nonlinearity in NSE more directly. The passivity framework is effective in flow control based on the nonlinear

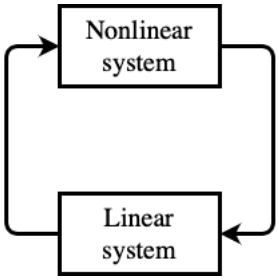

Figure 1.1: Illustration of the Lur'e feedback system

NSE [HJS16, Dam16, Dam19]. In these studies, the passivity property [Kha02] of the nonlinear terms in the incompressible NSE is leveraged to design a controller to stabilize the linear system; however, it is shown that due to the passivity property, the controller stabilizes the nonlinear fluid flow. Further advances have been made in input-output methods to study performance, worst-case amplification, stability, and transition for NSE using dissipation inequalities [AVGaP19]. Dissipation inequalities derived from NSE can be posed as linear matrix inequality (LMI) problems, which are then solved using convex optimization methods to analyze various wall-bounded shear flows. These techniques generalize the classical energy-based analysis approaches [Jos76] and have close ties with nonlinear Lyapunov stability analysis approaches developed for NSE based on sum-of-squares (SOS) optimization [GC12].

The Lyapunov based methods for analysis are very powerful since it is still one of the most popular methods used for analyzing a wide variety of nonlinear systems. Additionally, the Lyapunov methods also provide guarantees and certificates on performance, which is essential especially in fluid flows, since the exact solutions to NSE are not available in most cases.

1.4.1 Reduced-complexity analysis

In part II of this thesis, the reduced-complexity analysis addresses the second challenge of accounting for the nonlinear terms in stability and system analysis. The nonlinear terms are accounted for using the input-output properties of the nonlinearities, which are then added as constraints to Lyapunov-based linear matrix inequalities, thereby accounting for the effects of the nonlinear terms while only using system information from the linear part of the system.

This greatly reduces the complexity of the analysis problem by accounting for the nonlinear terms without their full complexity. Accounting for the exact behavior of the nonlinear terms is challenging as their behavior is difficult to model. The proposed framework enables obtaining results with guarantees and does not require multiple computationally expensive numerical simulations.

1.5 Overview of the Thesis

- Chapter 2 provides a control-theoretic overview of preliminaries like the stability of linear systems around equilibrium points, transient energy growth, linear matrix inequalities, Lyapunov stability, state-space representation, and overview of feedback-control.

- Chapter 3 addresses the 1^{st} challenge of dimensionality reduction by developing a control-oriented reduced-order modeling framework that enables developing special controllers that minimizing the maximum transient energy growth in the linearized channel flow system.

- Chapter 4 addresses the 2^{nd} challenge of including nonlinear terms for stability analysis by developing a reduced-complexity framework that uses quadratic constraints to account for nonlinear terms in the analysis of fluid flows.

- Chapter 5 further develops the quadratic constraints framework to improve our predictions by generalizing the reduced-complexity framework to ellipsoidal sets. We show that the generalization over ellipsoidal sets helps improve the accuracy of the predictions.

- Chapter 6 demonstrates how to extend the quadratic constraints framework for nonlinear analysis of the viscous Burgers equation.

- Chapter 7 provides concluding remarks and addresses possible avenues for future work.

1.6 Overview of Contributions

- Developed a control-oriented reduced-order modeling framework for fluid flows. The framework enables approximating energy of the full-order system after states have been truncated to reduce system size. This work resulted in the following publications:

  - A. Kalur and M. S. Hemati; Control-oriented model reduction for minimizing transient energy growth in shear flows; *AIAA Journal*, 2020
  - A. Kalur and M. S. Hemati; Reduced-Order Models for Feedback Control of Transient Energy Growth; *AIAA Flow Control Conference*, 2018

- Developed a reduced-complexity framework that accounts for quadratic nonlinear terms using quadratic constraints obtained from the nonlinear term's lossless property and other input-output properties. Formulated the problem of using spherical Lyapunov sets for stability analysis, transient energy growth analysis, and obtaining insights into flow physics using the quadratic constraints framework.

  - A. Kalur, P. Seiler and M. S. Hemati; Nonlinear Stability Analysis of Transitional Flows using Quadratic Constraints, *Physical Review Fluids*, 2021.
  - A. Kalur, P. Seiler and M. S. Hemati; Stability and Performance Analysis of Nonlinear and Non-Normal Systems using Integral Quadratic Constraints, accepted at *AIAA Aerospace Sciences Meeting*, 2020.

- Improve the proposed reduced-complexity modeling framework using constraints generalized to ellipsoidal sets instead of spherical sets. The ellipsoidal sets problem is solved with an iterative algorithm and a one-shot algorithm, which improve estimates compared to previously used spherical sets.

  - A. Kalur, T. Mushtaq, P. Seiler, M. S. Hemati; Estimating Regions of Attraction for Transitional Flows using Quadratic Constraints, in press, *IEEE Control Systems Letters (L-CSS)*

  - A. Kalur, T. Mushtaq, P. Seiler, M. S. Hemati; Estimating Regions of Attraction for Transitional Flows using Quadratic Constraints, *IEEE Conference on Decision and Control* (accepted), 2021

- We finally test the framework on the Burgers equations, which is a nonlinear PDE, and study the system's stability.

Chapter 2

Control Theoretic Preliminaries

2.1 Introduction

In this work, the problem of control-oriented reduced-order modeling and stability analysis using the proposed reduced-complexity framework for fluid flows have been approached from a system theoretic standpoint. Broadly this work leverages concepts from control and system theory and applies it to fluid flow applications. We briefly introduce the reader to some of the control theoretic concepts in this chapter. Here, we introduce the concept of stability analysis, linear matrix inequalities, and controller synthesis, as we will apply these concepts to fluid flow systems.

2.2 Stability of Linear Systems

Considering a simple linear time invariant (LTI) system of the form

$$\dot{\mathbf{x}} = A\mathbf{x}, \tag{2.1}$$

with an initial condition $\mathbf{x}_0 = \mathbf{x}(t_0)$. Then the system in Eq. (2.1) is *globally asymptotically stable* if the trajectories of the system $\mathbf{x}(t) \to 0$ as $t \to \infty$ given any initial condition $\mathbf{x}_0$. Given the linearized state-space equation in Eq. (2.1), the system response is given by $\mathbf{x}(t) = e^{A(t-t_0)}\mathbf{x}_0$. It can be seen that since the system response depends on the exponential of A, the state matrix A being Hurwitz is a necessary and sufficient

condition for the system to be *globally asymptotically stable* [Kha02].

Alternatively we also define the stability of a system around the equilibrium point $\mathbf{x} = \mathbf{0}$. This definition of stability helps understand how the systems solution is changing around the origin. It should also be noted if the equilibrium point $\mathbf{x} \neq 0$, then without loss of generality, the equilibrium point can be shifted to the origin via a change of variable [Kha02]. Therefore, we define the stability around the origin as shown in [Kha02] below.

Definition 1. *Let* $\mathbf{x} = 0$ *be an equilibrium point of Eq.* (2.1)*, the system is*

1. *is stable if for an* $\epsilon > 0$ *there is a* $\delta(\epsilon) > 0$ *such that* $\|\mathbf{x}_0\| < \delta \implies \|\mathbf{x}(t)\| < \epsilon \ \forall t \geq 0$.

2. *unstable if it is not stable.*

3. *asymptotically stable if it is stable and* δ *can be chosen such that* $\|\mathbf{x}_0\| < \delta \implies \lim_{t\to\infty} \mathbf{x}(t) = 0$.

An intuitive explanation for this is as follows. If the initial conditions lie within a ball of radius δ such that $\|\mathbf{x}_0\| < \delta$, then if the system is stable the state trajectories would remain inside a bigger ball of radius ϵ around the origin i.e., $\|\mathbf{x}(t)\| < \epsilon$. If the system trajectory cannot remain in the ball of radius ϵ around the origin, then the system is unstable. A special case of stability is *asymptotic stability*, where the trajectory not only remains inside the ϵ ball but it guarantees that the trajectories will converge to the origin as $t \to \infty$.

We will see in chapters 4 and 5 that determining the radius of the two balls, the one in which the initial conditions lie (δ-ball), and the ball that encapsulates the system trajectories (ϵ-ball) is important to characterize the system's stability. This becomes more important for systems that have nonlinear interactions that are typically hard to model explicitly. Identifying the two balls of radius ϵ and δ is called the challenger-answer problem [Kha02].

2.3 Transient Energy Growth and System Non-normality

In this section, we define the system's energy, the notion of transient energy growth, and non-normality. More generally, the energy E of the system in Eq. (2.1) is given by

$E := \mathbf{x}^T W \mathbf{x}$, where $W = W^T \succ 0$ is the weighting matrix to represent different energy metrics such as kinetic energy. Without loss of generality, we can find a transformation such that $\hat{\mathbf{x}} = W^{\frac{1}{2}}\mathbf{x}$ implying $E := \|\hat{\mathbf{x}}\|^2$. Throughout this work, we define $E := \mathbf{x}^T\mathbf{x}$, such that the states have been transformed to have a weighting matrix $W = I$, where $I \in \mathbb{R}^{n\times n}$ is the identity matrix. For conciseness of notation, we drop the notation of using hat on the states to show the application of the transformation.

The system in Eq. (2.1) is said to have a maximum energy growth of unity if the state matrix A is normal [WM07]. A normal matrix is defined as follows:

Definition 2. *A matrix $A \in \mathbb{C}^{n\times n}$ is normal if it commutes with its adjoint such that $AA^* = A^*A$, where A^* denotes the conjugate transpose of the matrix.*

When the state matrix A is non-normal its eigenvectors almost parallel to each other, then the system will hold energy growth on transient times scales despite being asymptotically stable [TE05]. This growth of energy on transient time scales is called transient energy growth (TEG) and is characteristic in wall-bounded fluid flows [SH01, TE05], which are the system of interest in this work. The TEGs maximum value or peak is referred to as maximum transient energy growth (MTEG). The MTEG represented by Θ is defined as,

$$\Theta := \max_{t>0} \max_{\|\mathbf{x}_0\|=1} \|\mathbf{x}(t)\|^2. \tag{2.2}$$

.

Lemma 1. *[WM07] The maximum transient energy growth, Θ, of the system in Eq.* (2.1) *is unity if and only if $A + A^T \prec 0$.*

Proof. Sufficient condition: if the rate of change of system energy with time is negative definite i.e., $d\|\mathbf{x}\|^2/dt < 0,\ \forall t > 0$ and all $\{\mathbf{x}(t) : \|\mathbf{x}(0\|) = 1\}$, then max $\{\|\mathbf{x}(t)\| : t \geq 0\} = \|\mathbf{x}_0\| = 1$. The rate of change of energy is given as:

$$\frac{d\|\mathbf{x}(t)\|^2}{dt} = \mathbf{x}(t)^T(A + A^T)\mathbf{x}(t) \tag{2.3}$$

this is negative only if $A + A^T \prec 0,\ \forall \mathbf{x}(t),\ t \geq 0$

Necessary condition: if $A+A^T \not\prec 0$, then there exists an $\mathbf{x}$ such that $\mathbf{x}^T(A+A^T)\mathbf{x} > 0$, which implies that there exist a $\mathbf{x}(0)$ such that $\mathbf{x}^T(A+A^T)\mathbf{x} > 0$ at $t = 0$. Therefore, $\|\mathbf{x}(t)\|^2 > 1$ for $t > 0$, so it is necessary that $A + A^T \prec 0$ □

In the case of $A+A^T \not\prec 0$, the initial perturbation that causes the MTEG is referred to as the *optimal perturbation* or *worst-case disturbance* and is denoted by $\mathbf{x}_0^{\text{opt}}$. The transient energy growth, which is characteristic of the linear operators in wall-bounded shear flows, has been shown to drive the system to the edge of the stability region, after which secondary nonlinear instabilities take over [TTRD93, Cha02]. Therefore, TEG is necessary for transition, and minimizing the MTEG would be desirable to delay or prevent sub-critical transition (see chapter 3 for MTEG minimizing control).

The system's energy is another metric to characterize the stability of the system, initially proposed by Lyapunov in his seminal work in 1890, where he proposed the notion characterizing the system's stability based on how some "metric" of the systems energy changes in time. This is also known as Lyapunov's direct method [Kha02]. This formulation is detailed in Section 2.4.3, and since it directly leads to the concepts of linear matrix inequalities (LMIs), we will first introduce the readers to the concept of LMIs.

2.4 Linear Matrix Inequalities

A linear matrix inequality (LMI) has the form [BEFB94b]

$$F(\boldsymbol{\xi}) := F_0 + \sum_{i=1}^{m} \xi_i F_i > 0, \tag{2.4}$$

where, $\boldsymbol{\xi} \in \mathbb{R}^m$ is the variable and $F_i = F_i^T \in \mathbb{R}^{n\times n}$ is a symmetric matrix with $i = 1, \cdots, m$. The LMI in Eq. (2.4) stands for $F(\boldsymbol{\xi})$ being positive definite, more specifically, if there exist a nonzero vector $\mathbf{w} \in \mathbb{R}^n$, then $\mathbf{w}^T F(\boldsymbol{\xi})\mathbf{w} > 0$. Similar, extensions can be made for nonstrict LMIs such that $F(\boldsymbol{\xi}) \succeq 0$. It should be noted that any nonstrict LMI can be converted to an equivalent LMI, where the resulting LMI has its strict version as feasible—a *strictly feasible LMI* [BEFB94a]. The strict

inequality can be used to obtain feasible solutions for nonstrict inequalities under special circumstances. In this work, we deal with non-strict LMIs.

The power of LMIs is that multiple LMIs can be expressed as a single LMI and hence there is no distinction between a single LMI or multiple LMIs [BEFB94a]. The formation of LMIs with variables as convex optimization problems enables solving for the variables using algorithms like ellipsoidal and interior-point methods to obtain solutions in polynomial time [BV04]. It can be seen that many problems in systems theory and control can be posed as LMIs with matrix variables.

2.4.1 Schur Complement

Posing problems as LMIs is extremely powerful since nonlinear (convex) inequalities can be converted to LMIs using the Schur complements. At the same time, additional constraints also can be added to the LMIs. The Schur complements basic idea, inspired from [BEFB94a], is sketched out in the next few lines as an example, e.g., given the nonlinear matrix inequalities $R(x) \succ 0$ and $Q(x) - S(x)^T R(x)^{-1} S(x) \succ 0$, these inequalities can be represented as an LMI of the following form:

$$\begin{bmatrix} Q(x) & S(x) \\ S(x)^T & R(x) \end{bmatrix} \succ 0. \tag{2.5}$$

More formally the Schur complement for strict inequalities for general matrices of the form $A = A^T \in \mathbb{R}^{n \times n}$, $B \in \mathbb{R}^{n \times m}$, and $C = C^T \in R^{m \times m}$ is stated as the following conditions being equivalent [CF21]:

1. $\begin{bmatrix} A & B \\ B^T & C \end{bmatrix} \prec 0.$
2. $A - BC^{-1}B^T \prec 0,\ C \prec 0.$
3. $C - B^T A^{-1} B \prec 0,\ A \prec 0.$

An illustration of using Schur complement can be seen in the following example: the maximum singular value or 2-norm of a matrix $Z(x) \in \mathbb{R}^{p \times q}$, which is affinely dependent

on x, can be upper bounded by 1, i.e., $\|Z(x)\|_2 < 1$ [BEFB94a]. This can be enforced using the Schur complement as follows

$$\begin{bmatrix} I & Z \\ Z^T & I \end{bmatrix} \succ 0. \tag{2.6}$$

Which results in $I - ZZ^T \succ 0$ and is equivalent to $\|Z\|_2 < 1$.

So far we have shown the Schur complement for strict inequalities, however, the Schur complement for non-strict inequalities states that the following conditions are equivalent [CF21]:

1. $\begin{bmatrix} A & B \\ B^T & C \end{bmatrix} \preceq 0.$
2. $A - BC^\dagger B^T \preceq 0$, $C \preceq 0$, $B(I - CC^\dagger) = 0$, where $C^\dagger$ is Moore-Penrose Pseudo inverse of C.
3. $C - B^T A^\dagger B \preceq 0$, $A \preceq 0$, $B^T(I - AA^\dagger) = 0$, where $A^\dagger$ is Moore-Penrose Pseudo inverse of A.

The ability to write nonlinear (convex) inequalities as LMIs extends itself to various applications in control theory and optimization, as will be seen in later parts of this document.

2.4.2 Generalized Eigenvalue Problem

Another important concept we will frequently encounter is the generalized eigenvalue problem (GEVP), which aims to determine the maximum (minimum) generalized eigenvalue of a pair of matrices that affinely depend on a variable. The GEVP can be cast as a quasi-convex optimization problem, with convex LMI constraints and a quasi-convex objective. The general form of the GEVP as an optimization problem is

$$\begin{aligned} \text{minimize} \quad & \lambda && (2.7)\\ \text{subject to} \quad & \lambda B(x) - A(x) \succ 0, && (2.8)\\ & B(x) \succ 0, && (2.9)\\ & C(x) \succ 0, && (2.10) \end{aligned}$$

where, $A,\ B,\ C$ are symmetric matrices that are affine functions of x [BEFB94a].

2.4.3 LMIs in Stability Analysis

One of the first known LMIs originated in 1890 from Russian mathematician Aleksandr Mikhailovich Lyapunov. Lyapunov, while studying the stability of dynamical systems, determined that system stability can be studied using the notion of energy of the system; this is also known as the *direct method*. Formally this result is stated as a theorem shown below,

Theorem 1. *[Kha02] Let* $\mathbf{x} = 0$ *be an equilibrium point of Eq.* (2.1)*. Let* $V : \mathbb{R}^n \to \mathbb{R}$ *be a continuously differentiable function such that*

$$V(0) = 0 \text{ and } V(\mathbf{x}) > 0 \ \forall \mathbf{x} \neq 0 \quad (2.11)$$

$$\dot{V}(\mathbf{x}) \leq 0, \ \forall \mathbf{x} \in \mathbb{R}^n \quad (2.12)$$

then, $\mathbf{x} = 0$ *is stable. Moreover, if*

$$\dot{V}(\mathbf{x}) < 0, \ \forall \mathbf{x} \in \mathbb{R}^n \quad (2.13)$$

then the $\mathbf{x} = 0$ *is globally asymptotically stable.*

Proof. See theorem 4.1 proof in [Kha02]. □

Lyapunov proposed using a quadratic energy functions of the form $V(\mathbf{x}) = \frac{1}{2}\mathbf{x}^T P \mathbf{x}$ with $P = P^T \succ 0$. He showed that the system in Eq. (2.1) is globally asymptotically stable if and only if $\frac{dV(\mathbf{x})}{dt} = \mathbf{x}^T(A^T P + PA)\mathbf{x} < 0$. Intuitively, the Lyapunov function

V is a measure of energy in the system; therefore, the condition in Eq. (2.13) in the theorem 1 implies that the energy decreases along any system's trajectory. This condition gives rise to the Lyapunov inequality

$$A^T P + PA \prec 0. \tag{2.14}$$

The above inequality is used to study the stability of systems by searching for a positive-definite P that satisfies Eq. (2.14).

Following the proposition of the Lyapunov inequality for stability, numerous extensions have used LMIs to study the system's stability [Kha02], analysis of nonlinear systems using quadratic constraints [MR97], design of robust control laws [JJW91], etc.

2.4.4 LMI for MTEG Analysis

Given a stable linear system of the form in Eq. (2.1), then the MTEG, Θ of the system is unity if and only if $A + A^T \prec 0$ [WM07]. Conversely, if $\Theta > 1$, i.e., a system holds transient energy growth, then $A + A^T \not\prec 0$. This condition can be used to study if the linear systems hold TEG or not; however, estimating the MTEG in the system is important.

The authors in [WM07] demonstrate that an upper bound q for θ can be found using Lyapunov functions. The argument to obtain an upper bound q on the Θ considers using bounding ellipsoids on system trajectories to estimate q. The argument is as follows. Assume $V(\mathbf{x}) = \mathbf{x}^T P\mathbf{x}$ is a Lyapunov function for a given system with $I \preceq P \preceq qI$. If the initial condition $\mathbf{x}_0$ lies in the ellipsoid $\{\mathbf{x} : \mathbf{x}^T P\mathbf{x} \leq 1\}$, then $\mathbf{x}(t)$ remains in this level set for all $t \geq 0$ [Bla99, WM07]. Thus $\mathbf{x}(t)^T P\mathbf{x}(t) \leq \mathbf{x}(0)^T P\mathbf{x}(0)$. Combining this with $I \preceq P \preceq qI$ yields $E(t) \leq \mathbf{x}(t)^T P\mathbf{x}(t) \leq \mathbf{x}(0)^T P\mathbf{x}(0) \leq qE(0)$. Therefore, $\Theta \leq q$ [Che84].

The least upper bound q^* is defined as $q^* := \lambda_{max}(P)\lambda_{max}(P^{-1})$ such that $P = P^T \succ 0$ and P satisfies $A^T P + PA \prec 0$. The problem of estimating q^* can be formulated as that of minimizing the condition number of P and is obtained by solving the following GEVP [WM07, BEFB94a]:

$$
\begin{aligned}
q^* := \text{minimize} \quad & q \\
\text{subject to } & \mathrm{I} \preceq P \preceq q\mathrm{I}\ , \\
& A^T P + PA \prec 0.
\end{aligned}
\tag{2.15}
$$

Here, the bounds $I \preceq P \preceq qI$ ensure that $\lambda_{max}(P)/\lambda_{min}(P) \leq q$. This optimization with LMI constraints and a linear cost involving variables (P, q) is known as a semidefinite program (SDP). The LMI constraints imply that $V(\mathbf{x}) := \mathbf{x}^T P\mathbf{x}$ is a Lyapunov function for the system such that $V(\mathbf{x}(t)) \leq V(\mathbf{x}(0))$ for all $t \geq 0$. The bounds on P further imply that $\|\mathbf{x}(t)\|^2 \leq q^*\|\mathbf{x}(0)\|^2$. These LMI constraints are conservative in general, and hence q^* is a (possibly non-tight) upper bound on the MTEG.

2.5 Sate-Space Representation

Given that the dynamics of fluid flow systems are governed by the NSE, which are infinite-dimensional PDEs, we approximate the PDEs to a finite-dimensional linear ordinary differential equations (ODEs) of the form,

$$\dot{\mathbf{x}} = A\mathbf{x} + B\mathbf{u}, \tag{2.16}$$

$$\mathbf{y} = C\mathbf{x} + D\mathbf{u}. \tag{2.17}$$

Here, $\mathbf{x} \in \mathbb{R}^n$ is the state vector of dimension n, $\mathbf{u} \in \mathbb{R}^p$ is the control input vector of dimension p and $\mathbf{y} \in \mathbb{R}^q$ is the output vector of dimension q. The matrix $A \in \mathbb{R}^{n\times n}$ is the state matrix that maps the time evolution dynamics of the system, $B \in \mathbb{R}^{n\times p}$ is the input matrix that maps the control input to the respective states, $C \in \mathbb{R}^{q\times n}$ is the output matrix that maps the information from the states to the output, and $D \in \mathbb{R}^{q\times p}$ is the feed-through matrix that feeds the input to the output. In this study, unless specified otherwise, we use full-state feedback such that the output matrix $C = I$, where $I \in \mathbb{R}^{n\times n}$ is an identity matrix of dimension, and there is no feed-through term, i.e., $D = \underline{0}$ with $\underline{0} \in \mathbb{R}^{q\times p}$ is a matrix of zeros.

2.6 Controller Synthesis

The system described in Eq. (2.16) can be controlled to achieve desired objectives like stabilizing the system to disturbances, tracking reference input, etc., by appropriately choosing the control law $\mathbf{u}$. One of the most fundamental methods to classify controller action is based on the information the controller will have access to, such that the controller can formulate appropriate control action. The control laws based on information available are broadly classified as full-state feedback control, observer-based output feedback control, and output feedback control. As the name describes, a full-state feedback controller has access to the complete state of the dynamical system, while the observer-based output feedback controller uses estimators to estimate the system output to design controllers accordingly. Lastly, output feedback control techniques will have access to the information available from the sensor suite deployed, thereby selecting the information available to the controller.

The full-information linear quadratic regulator (LQR) has been investigated in various capacities, and has been shown to increase transition thresholds within the channel flow system [BL18, IR08a, MQMW11]. Observer-based output-feedback controllers have also been invoked with some success [BL18, HBH03, JSK99]. In [JSK99], the authors successfully design a linear quadratic Gaussian (LQG) controller on a reduced-order Poiseuille flow system—combining the optimal LQR law with optimal state estimates from a Kalman filter. More recently, it has been shown that observer-based feedback strategies may exacerbate TEG in the controlled system, due to an adverse coupling between the fluid dynamics and the control system dynamics [HY18]. As a potential alternative, static output feedback formulations of the LQR problem have shown some promise in overcoming the limitations of LQG strategies under certain flow conditions within the channel flow system [YH18, YH19].

In this work, we will predominantly deal with full-state information feedback control. The full-state feedback control law is of the form

$$\mathbf{u} = -K\mathbf{x}, \tag{2.18}$$

where, K is the control gain and $\mathbf{x}$ is the system state.

Many methods exist on determining an appropriate $\mathbf{u}$ for the problem at hand, e.g., proportional-integral-derivative control or a combination thereof, adaptive control methods, LQR, etc. Once the desired control gain K has been obtained using the appropriate control objective, the control law in Eq. (2.18) is substituted in Eq. (2.16) to obtain the closed-loop system of the form

$$\dot{\mathbf{x}} = \underbrace{(A - BK)}_{A_{cl}} \mathbf{x}. \tag{2.19}$$

Here A_{cl} is the closed-loop dynamics of the system. The idea here is to use the control input $\mathbf{u}$ to achieve tasks like stabilization, tracking, disturbance rejection, etc., since now the control input can affect the dynamics of the closed-loop system to impart desired change. We will see in the next chapter how a state feedback control technique is used to minimize the MTEG in the linearized channel flow system.

Chapter 3

Part I: Control-Oriented Reduced-Order Models

3.1 Introduction

The transition of flows from a laminar to a turbulent regime has been extensively studied and remains a topic of continuing interest. As addressed earlier, turbulent flows exhibit specific detrimental effects on systems, more specifically, an increase in skin friction drag in wall-bounded shear flows [SH01]. It has been observed that transition to turbulence in many shear flows occurs at a Reynolds number (Re) much below the critical Re predicted by linear (modal) stability analysis of a steady laminar base flow [PH69, RH93b]. This sub-critical transition is associated with non-modal amplification mechanisms that cause small disturbances to grow before undergoing an eventual modal decay, based on the linear analysis [TTRD93, HR94, Sch07]. This TEG of disturbances can trigger non-linear instabilities and lead to bypass transition by driving the flow state beyond the region of attraction of the laminar equilibrium profile [TTRD93, Cha02].

Numerous investigations have considered the possibility of reducing TEG and delaying transition by employing feedback control techniques. Excellent reviews of past works can be found in [Bew01, BH11, KB07]. Linear quadratic optimal control has been a common approach for such applications and has shown success in achieving the desired objective [BL18, IR08a, MQMW11]. Interestingly, although all of these investigations have shown the promise of feedback control for reducing TEG and delaying

transition, in the case of linear quadratic regulators (LQR), which is a widely used optimal control strategy, the objective function to be minimized is the balance of integrated perturbation energy and input energy. It therefore stands that linear-quadratic optimal control techniques and related synthesis approaches do not necessarily minimize—nor even reduce—TEG. Thus, the most commonly employed controller synthesis approaches aim to achieve an objective that does not necessarily address the TEG problem directly.

Given the central role of TEG and non-modal instabilities in the transition process, it seems that a more appropriate objective function for transition control would be to minimize the MTEG, as proposed in [WM07]. This objective has direct connections with notions of *worst-case* or *optimal perturbations*, which correspond to disturbances that result in the MTEG [BF92]. The objective also has connections with optimal forcing functions determined from input-output analysis [JB05], though these types of "persistent disturbances" will not be considered in the present work. The minimum-MTEG optimal control problem—which can be specified for either full-state or output feedback [WM07]—can be posed as an LMI. The LMI constitutes a convex optimization problem as shown in Section 2.4, however, instead of open-loop minimization MTEG as shown in Section 2.4.4, we use a controller to close the loop and minimize MTEG in the closed-loop system. The LMI based MTEG minimizing control law can be solved for using standard methods, such as interior-point methods [BEFB94b]. However, the specific LMI problem that arises for MTEG minimization is computationally intractable for high-order systems, such as fluid flows; the memory requirements associated with existing solution methods scale as system order to the sixth power [MQMW11].

Despite the computational challenge, control laws that minimize the MTEG can be desirable over linear quadratic optimal control techniques. MTEG-minimizing controllers have been found to outperform LQR controllers in reducing TEG within a channel flow configuration [MQMW11]. To achieve this, a modal truncation was performed to obtain a reduced-order model (ROM) that would make controller synthesis tractable for the linearized channel flow system [MQMW11]. Despite the noteworthy performance reported in their study, it is well-established that modal truncation methods tend to yield ROMs that are poorly suited for controller synthesis [BSS12, JHK$^+$15]. A demonstration of this point is given in Section 3.4. Thus, it may be possible to synthesize MTEG-minimizing controllers with even better performance than those reported

in [MQMW11] by exploiting an appropriately tailored *control-oriented* model reduction strategy.

Various ROM approaches have been studied in the literature (see [TBD+, RD17] for excellent reviews of such techniques within the context of fluid dynamics). However, developing ROMs that facilitate the design of MTEG-minimizing controllers require a tailored approach. Control-oriented ROMs within this context must address a dual need: (i) approximate the perturbation energy to concisely and adequately describe the energy-based control objective; and (ii) reduce dimensionality to faithfully represent the input-output dynamics, as needed for computationally tractable controller synthesis. Identifying states that contribute substantially to both the perturbation energy and a system's input-output properties (e.g., controllability and observability) is a non-trivial task [Row05]. As discussed in Section 1.3.1, a projection onto proper orthogonal decomposition (POD) modes is known to be optimal for capturing the energy of a given signal; however, projection-based model reduction based on POD modes often fails to capture a system's input-output dynamics, making such models poor candidates for controller synthesis [IR08b, RD17]. In contrast, balanced truncation can be performed to obtain ROMs that retain a system's input-output properties [Moo81, ASG06]. The balanced truncation procedure can be shown to be equivalent to a Petrov-Galerkin ROM based on a projection onto a subspace spanned by a reduced set of balanced modes. For high-dimensional fluid flow systems, the balanced POD (BPOD) and related methods provide efficient tools for computing these balanced modes [Row05, WP02, ASG06]. Alternative control-oriented model reduction techniques can also be devised to retain a system's input-output properties, e.g., using ideas from robust control [JHK+15, ASG06].

The ROMs in this work uses POD and balanced truncation in conjunction. First, an output-projection of the full-state onto a set of dominant POD modes is performed. Subsequently, a balanced truncation is performed to reduce the state dimension, while retaining the most controllable and observable modes that contribute to the input-output dynamics. As we will see, this dual approach results in control-oriented ROMs that can yield effective MTEG-minimizing controllers. The resulting models can represent the perturbation energy in terms of a small number of POD modes, thus providing a convenient approximation of the objective function. Further, state-dimension is reduced

to a computationally tractable level while retaining the most controllable and observable states that are critical for effective controller design. The proposed COROM method are developed to minimize the MTEG, using dedicated controllers, in the linearized channel flow system.

3.2 Channel Flow Model

Consider the flow between two infinitely long parallel plates separated by a distance of $2h$. We refer to the x, y, z directions as streamwise, wall-normal and spanwise directions, respectively. The channel flow coordinate system is shown in Figure 3.1. The dynamics of the flow are governed by the NSE and the continuity equation. The NSE is given by:

$$\frac{\partial \mathbf{u}}{\partial t} = -\mathbf{u} \cdot \nabla \mathbf{u} - \nabla p + \frac{1}{Re} \nabla^2 \mathbf{u} \tag{3.1a}$$

$$0 = \nabla \cdot \mathbf{u} \tag{3.1b}$$

where, ∇ is the gradient operator, ∇^2 is the Laplacian operator, the instantaneous velocity ($\mathbf{u} = \mathbf{u}(x, y, z, t)$) and pressure ($p = p(x, y, z, t)$) are functions of the spatial variables (x, y, z) and time (t). To study the dynamics of perturbation about a laminar equilibrium solution we decompose the instantaneous velocity as $\mathbf{u} = \bar{\mathbf{U}} + \mathbf{u}'$ and $p = \bar{p} + p'$. Here, $(\bar{\mathbf{U}}, \bar{p})$ is the base flow and $(\mathbf{u}', p')$ are the perturbations about the base flow such that $\mathbf{u}' = [u' \;\; v' \;\; w']^T$. We are interested in the linear evolution of perturbations about a steady laminar parabolic base flow $\bar{U}_i = U(y)\delta_{i1}$, where δ_{i1} is the Kronecker delta. The parabolic base flow is given as, $U(y) = U_{cl}\left(1 - \frac{y^2}{h^2}\right)$ with U_{cl} as the centerline velocity. By assuming the magnitude of perturbations is small i.e., $|\mathbf{u}'| \ll |\bar{\mathbf{U}}|$, non-dimensionalizing based on U_{cl} and h, and accounting for only the linear terms, we get

$$\frac{\partial u'}{\partial t} + U\frac{\partial u'}{\partial x} + v\frac{\partial U}{\partial y} = -\frac{\partial p}{\partial x} + \frac{1}{Re}\nabla^2 u \tag{3.2}$$

$$\frac{\partial v'}{\partial t} + U\frac{\partial v'}{\partial x} = -\frac{\partial p'}{\partial y} + \frac{1}{Re}\nabla^2 v' \tag{3.3}$$

$$\frac{\partial w'}{\partial t} + U\frac{\partial w'}{\partial x} = -\frac{\partial p'}{\partial z} + \frac{1}{Re}\nabla^2 w' \tag{3.4}$$

$$\frac{\partial u'}{\partial x} + \frac{\partial v'}{\partial y} + \frac{\partial w'}{\partial z} = 0 \tag{3.5}$$

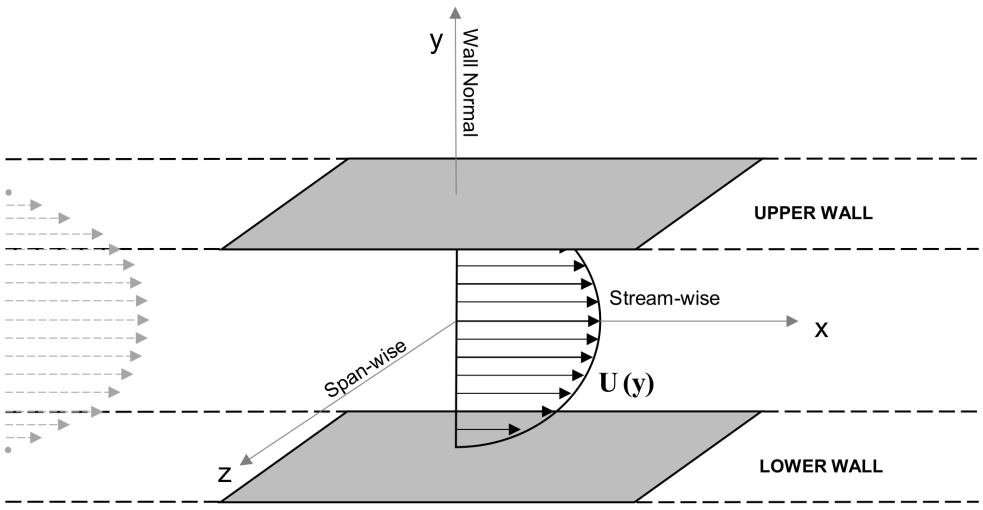

Figure 3.1: The coordinate system for the channel flow system

Taking the divergence of the continuity equation in Eq. (3.5) and using the y-momentum equation to eliminate the pressure term, we obtain an equivalent representation for the evolution equations, now in terms of the wall-normal velocity (v) and the wall-normal vorticity (η). A Fourier transform is applied in the streamwise and spanwise directions to obtain the well-known Orr-Sommerfeld and Squire equations [SH01],

$$\begin{aligned} \Delta\dot{\tilde{v}} &= \left[i\alpha U\Delta + i\alpha U'' + \frac{\Delta\Delta}{Re} \right]\tilde{v}, \\ \dot{\tilde{\eta}} &= \left[-i\beta U' \right]\tilde{v} + \left[-i\alpha U + \frac{\Delta}{Re} \right]\tilde{\eta}, \end{aligned} \tag{3.6}$$

where $\Delta = \frac{\delta}{\delta y^2} - \kappa^2$. Here, $\kappa^2 = \alpha^2 + \beta^2$, and (α, β) denotes the pair of streamwise

and spanwise wavenumbers, respectively. The no-slip boundary conditions in velocity-vorticity form are $\tilde{v}(y = \pm 1) = \frac{\partial \tilde{v}}{\partial y} \mid_{(y=\pm 1)} = \tilde{\eta} = 0$. The wall-normal direction is discretized using Chebyshev polynomials of the first kind [Boy00], allowing $\tilde{v}$ and $\tilde{\eta}$ to be approximated at N discrete collocation points. At each point, the approximation uses Chebyshev basis functions Γ_i and the respective unknown coefficients a_i. The resulting equations of motion can be expressed in the form $\dot{\mathbf{x}} = \mathcal{A}\mathbf{x}$, where $\mathbf{x}$ is a vector of Chebyshev coefficients; i.e., $\mathbf{x} = (a_{v_0}, \ldots, a_{v_N}, a_{\eta_0}, \ldots, a_{\eta_N})^T$.

One of the stages to bypass transition within the channel flow setting is the transient energy growth (TEG) of flow perturbations about the base-flow due to non-modal effects [SH01]. Following previous studies, we use the kinetic energy density as a measure of this TEG,

$$E(t) = \frac{1}{V} \int_V \rho \frac{u^2 + v^2 + w^2}{2} dV \ , \tag{3.7}$$

where ρ is the fluid density and V is the volume of a unit streamwise length of channel. In relation to earlier discussions, the kinetic energy density can be re-expressed as $E(t) := \mathbf{x}^T Q \mathbf{x}$, where $Q = Q^T \succ 0$ [MPW06, McK06].

To implement flow control, wall-normal blowing and suction actuation at the upper- and lower walls is introduced —consistent with prior investigations on controlling channel flow [MQMW11, JSK99, Bew01]. Following the modeling procedure in [MPW06], this can be modeled via the wall-transpiration boundary conditions $\tilde{v}(y = 1) = q_u$, $\tilde{v}(y = -1) = q_l$, $\frac{\partial \tilde{v}}{\partial y} \mid_{y=\pm 1} = 0$. Here, q_u and q_l are wall-normal velocities at the upper- and lower-wall, respectively. The final system formulation uses $\dot{q}_u$ and $\dot{q}_l$ as the control inputs, while reclassifying q_u and q_l as system states. This introduces two integrators—associated with the controls—within the system model. Finally, the actuated channel flow system can be expressed in state-space form, as in (2.16), with the state vector defined as $\mathbf{x} = (a_{v_0}, \ldots, a_{v_N}, a_{\eta_0}, \ldots, a_{\eta_N}, q_u, q_l)^T$ and the input vector defined as $\mathbf{u} = (\dot{q}_u, \dot{q}_l)^T$. It must be noted that the resulting system here is complex-valued, owing to the introduction of Fourier transformations in the streamwise and spanwise directions. As such, a final step is needed to transform the system into an equivalent real-valued state-space realization of the form in Eq. (2.16) i.e., $\dot{\mathbf{x}} = A\mathbf{x} + B\mathbf{u}$.

Further modeling details can be found in [MPW06].

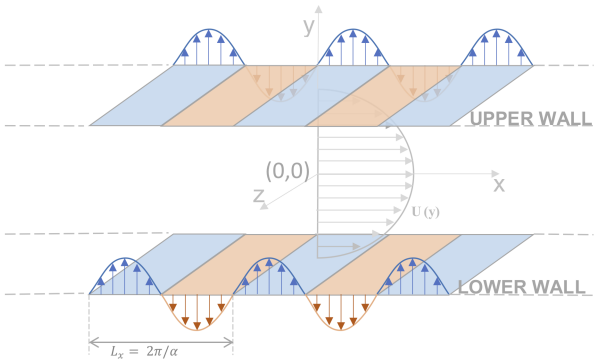

Figure 3.2: Schematic of the channel flow system with actuation

In the remainder, we consider this linearized channel flow model at a sub-critical Reynolds number of $Re = 3000$ (unless otherwise stated) for three different wavenumber pairs (α, β): $(1, 0)$, $(1, 1)$, and $(0, 2)$. The channel flow setup with actuation for the streamwise case is shown in Fig. 3.2. In all cases, the number of collocation points N is chosen so that the resulting state dimension is $n = 199$. The optimal spanwise disturbance to the uncontrolled system with $(\alpha, \beta) = (0, 2)$ yields the largest MTEG among all other streamwise, spanwise, and oblique wavenumber configurations. Hence, this spanwise disturbance is an important case to study for controller performance evaluation; The other two wavenumber pairs considered here have also been widely studied in the literature [MQMW11, HBH03].

3.3 Energy Minimizing Controllers

Given the linearized dynamics of flow perturbations $\mathbf{x}$ about a steady laminar base-flow in the form of Eq. (2.16). Owing to the role of transient energy growth in sub-critical transition, our aim here will be to reduce the MTEG using full-information feedback control laws of the form $\mathbf{u}(t) = -K\mathbf{x}(t)$, where K is a gain matrix determined by an appropriate synthesis strategy. In this study, two controller synthesis approaches will be considered: (i) linear quadratic regulation (LQR), and (ii) MTEG minimization via LMI-based synthesis.

3.3.1 Linear Quadratic Regulator

LQR is an optimal control a technique that has been commonly employed in a variety of flow control applications, including transition control. LQR controllers are designed to minimize the integrated balance between perturbation energy and control effort; i.e.,

$$\min_{\mathbf{u}(t)} J = \int_0^\infty (\mathbf{x}^T Q \mathbf{x} + \mathbf{u}^T R \mathbf{u}) dt \tag{3.8}$$

subject to the linear dynamic constraint in (2.16) and $R \succ 0$. The feedback control law that minimizes this cost function is given by $\mathbf{u} = -K\mathbf{x}$, where the control gain $K = R^{-1}B^T P$ and $P = P^T \succ 0$ is determined from the algebraic Riccati equation,

$$A^T P + PA - PBR^{-1}B^T P + Q = 0. \tag{3.9}$$

LQR is a widely used optimal control strategy owing to properties like guaranteed stability margins and robustness to parameter variations. However, it must be noted that the LQR formulation does not necessarily guarantee reductions in MTEG, let alone its minimization. In principle, a controller that minimizes the balance of integrated energies in (3.8) could still yield large energy peaks.

3.3.2 MTEG Minimizing Controller

A state feedback control gain for minimizing the MTEG in a closed-loop system can be found from the solution of a linear matrix inequality (LMI), as shown in Section 2.4. The solution approach leverages the relationship between MTEG and a system's condition number. From this, a control law can be devised to minimize the condition number of the closed-loop system to minimize the associated Θ in Eq. (2.2). In what follows, it is assumed that an appropriate transformation has been made so that $Q = I$ in the definition of kinetic energy E, as shown in Section. 2.3. A feedback control law that minimizes the upper bound Θ_u of the MTEG can be determined from the solution to

the LMI generalized eigenvalue problem [WM07]:

$$\begin{aligned} &\min \gamma \\ \text{subject to} \quad &I \preceq P \preceq \gamma I \\ &P = P^T \succ 0 \\ &AP + PA^T + BY + Y^T B^T \prec 0. \end{aligned} \tag{3.10}$$

This LMI problem can be solved using standard convex optimization methods, such as those available in the cvx software package for Matlab [GB14]. Here, γ upper bounds Θ_u. Thus, minimizing γ also minimizes Θ_u, which consequently minimizes the upper bound on Θ. The resulting full-state feedback control law is given by $\mathbf{u} = -YP^{-1}\mathbf{x}$, where Y and P are determined from (3.10).

Standard solution techniques for the LMI problem in (3.10) are presented in [BEFB94b]. However, available algorithms are computationally demanding, with memory requirements scaling as $\mathcal{O}(n^6)$ [MQMW11], making controller synthesis intractable for the high-dimensional systems of interest in flow control.

The present study aims to investigate the role of reduced-order models (ROMs) for facilitating controller synthesis by making the solution of this LMI problem tractable. Further, constructing reliable control-oriented ROMs requires consideration of the specific control objective. Since the LQR and MTEG-minimizing controllers to be studied here are based on energy-based control objectives, it stands that approximating the energy $E(t)$ will be an important consideration for reduced-order modeling. Section 3.5 presents a method for obtaining control-oriented ROMs for LQR and MTEG-minimizing controller synthesis. Before proceeding onto the COROM section, we will motivate the need for COROMs using a limiting example of modal truncation.

3.4 Limitations of modal truncation for MTEG-minimizing control

Modal truncation based on the eigendecomposition of the matrix $A = V\Lambda V^{-1}$ in Eq. (2.16) is a common approach for reduced-order modeling, primarily owing to its simplicity. Since the eigenvalues λ_i in the diagonal matrix Λ provide information about

the relative time-scales of the modal response, a simple strategy for modal truncation is to omit modes using time-scale arguments. For example, when long term behavior is of interest, then modes with fast decay rates and/or high oscillation frequencies can be omitted. ROMs constructed time-scale based modal truncation will not necessarily capture the input-output dynamics needed for controller synthesis. Thus, another common approach considers a measure of modal controllability/observability, given by the ratio [ASG06]

$$\zeta_i = \frac{\|C_i\|\|B_i\|}{|\mathrm{Re}\{\lambda_i\}|}, \tag{3.11}$$

where B_i and C_i correspond to the i^{th} row and column of the modal representations of the matrices B and C from Eq. (2.16) and Eq. (2.17), respectively. Modes with larger values of ζ_i contribute more to the input-output dynamics and should be be retained, whereas those with lower values of ζ_i can be truncated.

Here, we apply both of these modal truncation approaches to arrive at ROMs with order $r < n$ of the linearized channel flow system with $(\alpha, \beta) = (1, 0)$ and $Re = 3000$. For truncation modal truncation by time-scale arguments, we truncate the "fastest" modes (i.e., stable modes with relatively large $|\mathrm{Re}\{\lambda_i\}|$). For truncation by modal controllability/observability, we truncate the least controllable/observable modes (i.e., stable modes with relatively small ζ_i). Each of these ROMs is then used to design the LMI-ROM and LQR-ROM controllers. The resulting performance of each of these controllers is compared with the LQR-FOM controller in Figure 3.3. The model orders here were chosen based on convergence of the ROM open-loop frequency-response relative to the FOM. We note that for the results reported here, the FOM dimension is set to $n = 99$; without doing so, ROMs of size r, based on modal truncation converge with $r > 80$, which makes the LMI-based synthesis procedure intractable with the available computational resources. Figure 3.4 reports the resulting MTEG Θ as a function of r for ROMs constructed by each of the modal truncation approaches. Interestingly, the truncation of "fast modes" yields improved MTEG performance with the LMI-ROM than truncation based on ζ_i. These results indicate that modal truncation is a poor candidate for designing controllers to reduce TEG. Although in some cases these models can result in effective control laws, the model orders tend to be higher than the tailored approaches considered in this study. The short-comings of modal truncation—and other ROM

methods—for TEG reduction further motivates the need for control-oriented model reduction, like the approach presented in Section 3.5.

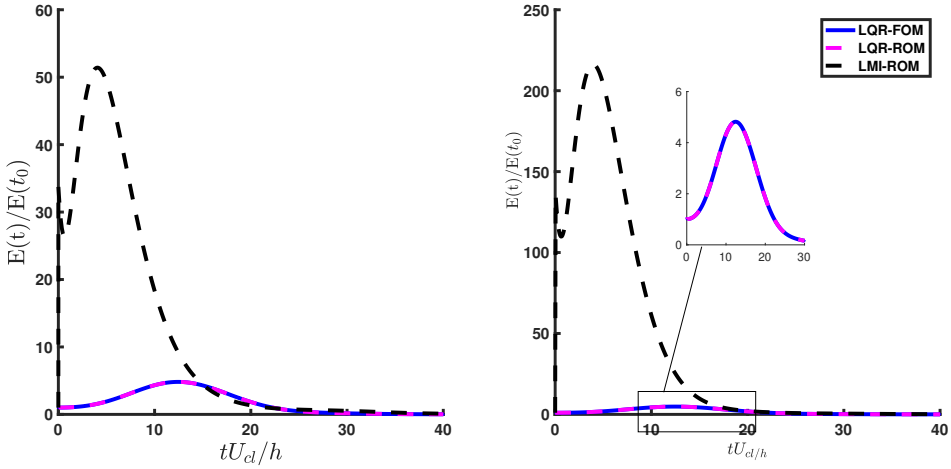

(a) $|\mathrm{Re}\{\lambda_i\}|$ modal truncation ($r = 50$) **(b)** ζ_i modal truncation ($r = 50$)

Figure 3.3: Worst-case closed-loop TEG response for $(\alpha, \beta) = (1, 0)$ and $Re = 3000$.

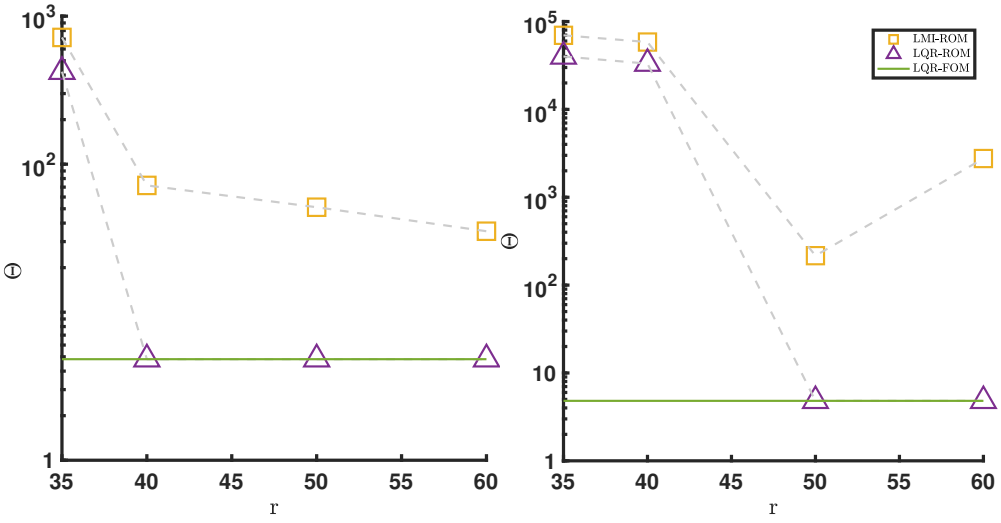

(a) $|\mathrm{Re}\{\lambda_i\}|$ modal truncation **(b)** ζ_i modal truncation

Figure 3.4: Closed-loop MTEG Θ as a function of ROM order r for $(\alpha, \beta) = (1, 0)$ at $Re = 3000$.

3.5 Control-Oriented Reduced-Order Models

3.5.1 Energy Matching Using Output Projection

The aim is to minimize the systems energy, $E := \mathbf{x}^T\mathbf{x}$, however, once the states are truncated to reduce the system dimension, the definition of the systems energy is not consistent anymore. Therefore, to retain the definition of energy of the original system, we will redefine the system's energy in terms of the output of the system. The basic idea underlying the ROMs proposed here is first to append an output equation to (2.16) to keep track of the state response in terms of $r < n$ POD modes,

$$\begin{aligned} \dot{\mathbf{x}} &= A\mathbf{x} + B\mathbf{u} \\ \mathbf{z} &= \Phi_r^T\mathbf{x}. \end{aligned} \tag{3.12}$$

Here, $\mathbf{z} \in \mathbb{R}^r$ is a vector of POD coefficients and $\Phi_r \in \mathbb{R}^{n\times r}$ is a matrix whose columns are the r dominant POD modes, defined with respect to an appropriate inner-product, such that

$$E(t) \approx \tilde{E}(t) := \mathbf{z}^T(t)\mathbf{z}(t). \tag{3.13}$$

Thus, rather than requiring full-state information to compute energy, only the r-dimensional output of POD coefficients is needed to approximate the energy response. This approach is sometimes described as an output projection onto POD modes since the output could also be viewed as projecting the full-state output onto the dominant POD modes [Row05]. It should be noted that output projection in (3.12) does not change the state dimension n of the model.

To find the POD modes, we use the snapshot POD approach [TBD$^+$]. Through heuristics, we found that POD mode obtained from snapshots of the system's impulse response matrix provided an adequate basis for the projection. Therefore, to compute the POD modes (Φ_r), we obtain the impulse response $G_i(t)$ from the i^{th} input to the full-state output for each of the p inputs. In generating this data, we first transform the state $\mathbf{x}$ into a coordinate system in which $Q = I$. These impulse response data are then collected and arranged within a single snapshot matrix $H := \begin{bmatrix} G_1(t) & G_2(t) & \cdots & G_p(t) \end{bmatrix}$.

The POD modes are then computed by taking the singular value decomposition (SVD) of $H = U\Sigma V^T$. The dominant POD modes are then determined as the leading $r \leq n$ left singular vectors—i.e., $\Phi_r = [\mathbf{u}_1, \mathbf{u}_2, \ldots, \mathbf{u}_r]$, where $\mathbf{u}_i$ are columns $i = 1, \ldots, r$ of U. We note that the POD modes could also be computed analytically, though the data-driven method of snapshots is most commonly used in practice [TBD$^+$]. Thus, important parameters for generating the impulse response data will be the length of the simulation (t_f) and sampling interval (δ_t), which will be discussed in the results section.

3.5.2 Balanced Truncation

Up to this point, we have shown that the system energy can be approximated using just r POD modes, with the associated POD coefficients are tracked as the system output $\mathbf{z}$. However, to make the LMI problem for MTEG-minimizing controller synthesis computationally tractable, we still need to reduce the state dimension of the system. In the study here, we will perform a balanced truncation of (3.12) and retain only the dominant s balanced modes. Such a truncation will ensure that the input-output dynamics are preserved, making the resulting s-dimensional ROM suitable for controller synthesis [ASG06]. To perform a balanced truncation, we first apply a balancing. transformation $\mathbf{x} = T\bar{\mathbf{x}}$. In the *balanced coordinates* $\bar{\mathbf{x}}$, the controllability Gramian $\bar{W}_c$ and the observability Gramian $\bar{W}_o$ are equal and diagonal. To determine the balanced realization, one must first compute the controllability Gramian W_c and observability Gramian W_o from the Lyapunov equations, $AW_c + W_cA^T - BB^T = 0$ and $W_oA + A^TW_o + C^TC = 0$, respectively. Once the Gramians are computed, the balancing transformation $\mathbf{x} = T\bar{\mathbf{x}}$ can be found in three steps [LHPW87]: (i) compute the lower triangular Cholesky factorizations of $W_o = L_oL_o^T$ and $W_c = L_cL_c^T$; (ii) compute the SVD of the products of Cholesky factors $L_o^TL_c = \bar{U}S\bar{V}^T$; and (iii) form the balancing transformation $T = L_c\bar{V}S^{\frac{1}{2}}$ and $T^{-1} = S^{\frac{1}{2}}\bar{U}^TL_o^T$.

In balanced coordinates, each mode's relative contribution to the input-output dynamics of the system is clear. We have $\bar{W}_c = \bar{W}_o = \mathrm{diag}(\bar{\sigma}_1, \ldots, \bar{\sigma}_n)$, where $\bar{\sigma}_1 \geq \bar{\sigma}_2 \geq \cdots \geq \bar{\sigma}_n > 0$ are the system's Hankel Singular Values (HSVs). Since the HSVs relay information about relative contributions to the input-output dynamics, truncating balanced modes with "small" HSVs provides a convenient strategy for reducing state-dimension while preserving the input-output dynamics [ASG06]. Upon performing the

balanced truncation, the dominant s balanced modes of the system are retained, and the $n-s$ modes corresponding to the lowest HSVs are truncated. The resulting state-space realization is given by,

$$\dot{\bar{\mathbf{x}}}_s = \bar{A}_s \bar{\mathbf{x}}_s + \bar{B}_s \mathbf{u} \tag{3.14}$$

$$\bar{\mathbf{z}}_s = \bar{C}_s \bar{\mathbf{x}}_s \tag{3.15}$$

where $\bar{\mathbf{x}}_s \in R^s$ is the reduced state vector and the system matrices are defined as $\bar{A}_s := T_s^{-1} A T_s$, $\bar{B}_s := T_s^{-1} B$, $\bar{C}_s := \Phi_r^T T_s$. Here, $T_s \in \Re^{n \times s}$ denotes a matrix whose s columns are the leading s columns of T, and $T_s^{-1} \in \Re^{s \times n}$ denotes a matrix whose s rows are the leading s rows of T^{-1}. Finally, the perturbation energy $E(t)$ can now be approximated from this control-oriented ROM as,

$$\bar{E} = \bar{\mathbf{x}}_s^T \bar{Q} \bar{\mathbf{x}}_s, \tag{3.16}$$

where $\bar{Q} = T_s^T \Phi_r \Phi_r^T T_s \in R^{s \times s}$. In this study, we take $s = r$, and so will solely report r as the dimension of the reduced-order model.

To assess feedback control performance for the MTEG that can be experienced in closed-loop, additional care must be taken when computing the optimal disturbances in this study. Since MTEG analysis is to be performed on the full order system, feedback controllers designed using the ROMs described here are first "lifted" to a control gain with compatible dimensions as the full order model. In this way, the optimal disturbance for the full order closed-loop system can be computed directly. Of course, to actually implement the resulting feedback controllers in practice, one would simply use the reduced-order gain matrix to take advantage of the reduced computational complexity at run-time.

The procedure outlined here will enable a means of obtaining control-oriented reduced-order models that can be used to synthesize feedback controllers, especially those aimed at achieving certain energy-based objectives—as with MTEG-minimization. We emphasize that the control-oriented model reduction procedure described here and other similar approaches have been explored in many previous studies [Moo81, Row05, WP02, IR08a, IR08b]. The contribution of the present study is to investigate the applicability of such model reduction techniques to minimize the MTEG using the LMI-based

synthesis procedure proposed in [WM07, MQMW11].

3.6 Results

Next, the control-oriented reduced-order modeling approach introduced in the previous section is investigated within the context of controlling TEG in a linearized channel flow presented in Section 3.2. In Section 3.6.1, the frequency responses of various ROMs are analyzed to assess open-loop modeling performance. Finally, ROM-based controller performance is investigated in Section 3.6.2 by comparing the MTEG resulting in the closed-loop system response. The associated flow responses are also studied and discussed.

3.6.1 Frequency Response

Here, we examine how the control-oriented ROMs introduced in Section 3.5 approximate the dynamics of the full-order model (FOM) for the linearized channel flow system, for which $n = 199$. Specifically, we examine whether the ROMs developed here capture the input-output behavior of the FOM accurately. In multi-input multi-output (MIMO) systems, the singular values σ of the system's transfer function over various frequencies provide a means of characterizing the input-output behavior of the system. The singular values provide information on the variation in the system's principal gains in any of the p input direction [SP05]. Here, we investigate these characteristics as a function of ROM order r from the input $\dot{q}_u$ to the flow-state (see Figure 3.5). In this work, the scaled frequency is given by $f^* = ftU_{cl}/h$. The frequency response data reveal that increasing the order r of the ROM decreases the approximation error concerning the FOM response. Indeed, the trend is more clear from Table 3.1, which summarizes the root mean square error (RMSE) between the ROM and FOM frequency responses. The acceptable accuracy of a ROM in approximating a FOMs response is mostly application-specific. For the case here, the RMSE metric suggests that ROMs of $r \geq 20$ perform moderately well. Further, even using the higher-order $r = 50$ models—which reflect excellent agreement with the FOM frequency-response—will make LMI-based controller synthesis tractable. The transfer function from input channel $\dot{q}_l$ to the flow-state exhibits similar convergence in the frequency-response.

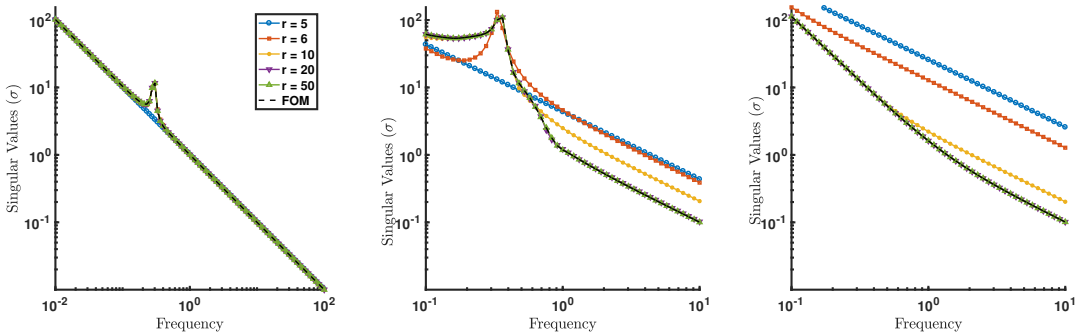

(a) $\alpha = 1,\ \beta = 0$ **(b)** $\alpha = 1,\ \beta = 1$ **(c)** $\alpha = 0,\ \beta = 2$

Figure 3.5: Frequency response from $\dot{q}_u$ to the flow-state at $Re = 3000$.

	$r = 5$	$r = 6$	$r = 10$	$r = 20$	$r = 50$
$\alpha = 1, \beta = 0$	1.079	0.049	0.0033	1.340×10^{-4}	5.726×10^{-6}
$\alpha = 1, \beta = 1$	18.765	14.135	2.990	0.0891	9.603×10^{-5}
$\alpha = 0, \beta = 2$	119.19	61.0560	13.332	1.705	0.0193

Table 3.1: RMSE between the frequency-response of the FOM ($n = 199$) and the ROM of order r at $Re = 3000$.

Finally, it should be noted that, for the ROMs presented here, the data-sampling parameters t_f and δ_t in the snapshot POD stage of the ROM procedure was tuned to ensure convergence of the ROM response to the FOM response. In the $Re = 3000$ setting, for streamwise waves and oblique waves $\delta_t = 0.01$ and $t_f = 30$ and 50 respectively. While for spanwise waves we use $\delta_t = 1$ and $t_f = 500$ to obtain adequate models. All times reported in this work are non-dimensionalized, and correspond to non-dimensional convective time units $\frac{tU_{cl}}{h}$.

3.6.2 Minimizing Maximum Transient Energy Growth

The synthesis of MTEG-minimizing controllers via the solution of the LMI-problem in (3.10) is enabled by the control-oriented ROMs reported in Section 3.6.1 above. The resulting controllers will be referred to as *LMI-ROM controllers* here. For benchmarking, we compare MTEG performance with two sets of LQR controllers—one designed based on the FOM ("LQR-FOM") and one designed based on the same ROM used for the LMI-based synthesis ("LQR-ROM"). Additionally, since the MTEG-minimizing

controller in the LMI-ROM was designed without constraining the control input, we relax the penalty on the input effort within the LQR cost function in (3.8) by setting $R = 10^{-6}I$, where I denotes the identity matrix. This is done in an effort to make a fair comparison between the LMI-ROM, LQR-ROM, and LQR-FOM controllers. Note, this differs from the approach taken in [MQMW11], in which the authors implemented a constrained version of the controller. All controllers are applied to the full-order channel flow model described in Section 3.2 above, then compared based on the MTEG Θ for each respective closed-loop system. In general, the optimal perturbation will differ between each closed-loop system and will also differ from that of the uncontrolled system. Here we use the optimal perturbation of the respective closed-loop system to perform MTEG analysis. In this study, each optimal perturbation is calculated using the algorithm presented in [WA11]. As shown in Figure 3.6, the LMI-ROM controller reduces the MTEG in the system relative to each of the LQR-based controllers for each of the wavenumber pairs considered. For $(\alpha, \beta) = (1, 0)$, the LMI-ROM controller reduces Θ by a factor of ≈ 1.88 in comparison with the LQR controllers (see Figure 3.6a). Similarly, the LMI-ROM reduces MTEG by a factor of ≈ 2.6 relative to the LQR controllers for $(\alpha, \beta) = (1, 1)$ (see Figure 3.6b). Finally, for $(\alpha, \beta) = (0, 2)$, the difference in MTEG reduction between the LMI-ROM controller and the LQR controllers is only marginally greater (See Figure 3.6c). This result is consistent with the findings in [MQMW11], for which wall-normal blowing/suction was less effective for TEG control than spanwise blowing/suction at the walls. For all controllers and all wavenumber pairs considered here, MTEG was reduced relative to the uncontrolled flow. These results are summarized in Table 3.2.

	r	Θ			
		Uncontrolled	LMI-ROM	LQR-FOM	LQR-ROM
$\alpha = 1, \beta = 0$	40	20.31	2.56	4.81	4.81
$\alpha = 1, \beta = 1$	58	107.00	7.58	20	20.28
$\alpha = 0, \beta = 2$	40	1762	271.2	287.1	287.1

Table 3.2: MTEG Θ for the uncontrolled and controlled channel flow system at $Re = 3000$.

Although the LMI-ROM controller outperforms both of the LQR controllers in reducing the MTEG (Θ) in the results above, these results depend on the order r of the ROM used for controller synthesis. To investigate this influence, we vary r in the

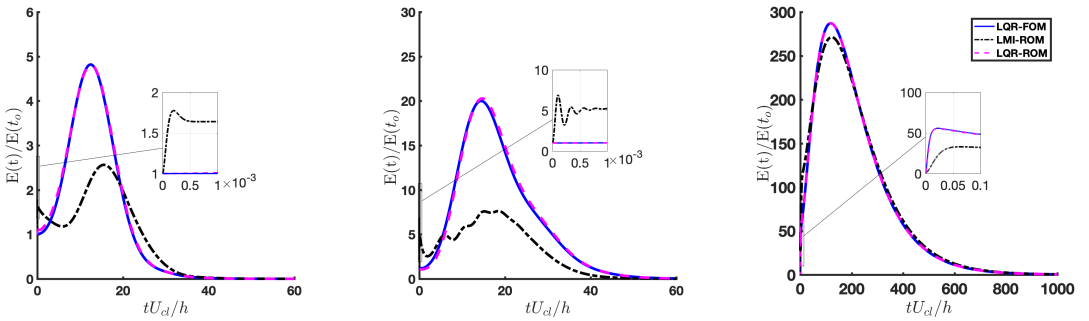

(a) $\alpha = 1, \beta = 0$ with $r = 40$. **(b)** $\alpha = 1, \beta = 1$ with $r = 58$ **(c)** $\alpha = 0, \beta = 2$ with $r = 40$

Figure 3.6: Worst-case closed-loop TEG responses at $Re = 3000$.

ROM design, then study controller performance on the FOM for streamwise and oblique waves—$(1, 0)$ and $(1, 1)$, respectively—still with $Re = 3000$. We only report values of r for which the open-loop ROMs successfully converge to the FOM dynamics, and so do not consider r smaller than these values here. Figure 3.7 shows that Θ decreases with increasing ROM order r using the LMI-ROM controller. The same is true for the LQR-ROM controller, but the convergence is more rapid. MTEG for the LQR-ROM converges to that of the LQR-FOM for $r = 20$ for streamwise and spanwise waves and $r = 25$ for oblique waves. We found that for streamwise and oblique wavenumber pairs considered, there exists a ROM order r such that the LMI-ROM controller will outperform both of the LQR controllers for MTEG reduction. We note that although the LMI-ROM yields a reduction in MTEG relative to both LQR-based controllers in the spanwise wave case, this case was also found to be relatively insensitive to the ROM order. Again, this finding is consistent with the results reported in [MQMW11], which found that spanwise blowing/suction actuation was required to achieve meaningful reductions in MTEG. Since the current investigation is focused on control-oriented ROM, we continue to focus on wall-normal blowing/suction actuation. Lastly, note that the fact that the LMI-ROM requires a larger r than the LQR-ROM for MTEG performance to converge is to be expected; TEG is a phenomenon intimately related to $\dot{E}(t)$, whose approximation requires higher-precision estimates of $E(t)$.

It is clear that the LMI-ROM controller in the above cases outperforms both of the LQR controllers. To investigate this further, we proceed to analyze the details of the

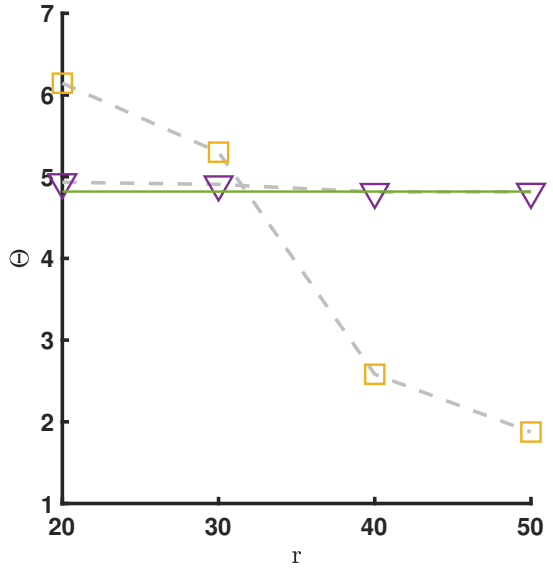

(a) $\alpha = 1, \beta = 0$.

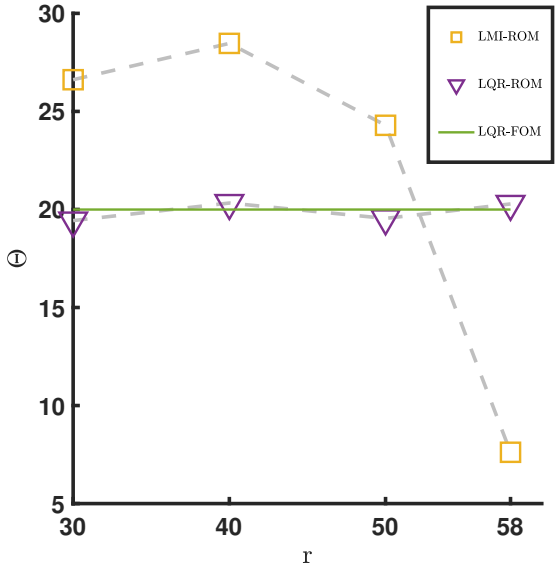

(b) $\alpha = 1, \beta = 1$

Figure 3.7: Closed-loop MTEG Θ as a function of ROM order r at $Re = 3000$.

wall-normal actuation and its influence on the flow perturbations.

3.6.3 Inspecting the control input

To investigate this further, we proceed to analyze the details of the wall-normal actuation and its influence on the flow perturbations. Figure 3.8 shows the actuated wall-normal velocity at the upper- and lower-walls—q_u and q_l, respectively—for each controller. The case of $(\alpha, \beta) = (1, 0)$, shown in Figure 3.8a, reveals that LMI-ROM controller results in blowing and suction at the upper- and lower walls that are equal in magnitude but opposite in direction. In contrast, each of the LQR-ROM and the LQR-FOM controllers produces almost identical (both in magnitude and direction) blowing and suction at the upper and lower walls. Interestingly, the LQR-ROM controls differ from the LQR-FOM controls for a short period at the beginning of the response, an expected artifact of the modal truncation. The 5% settling time on the actuation for the LMI-ROM controllers is ≈ 43 convective time units; the LQR controllers settle in ≈ 34 convective time units, indicating a shorter duration of control.

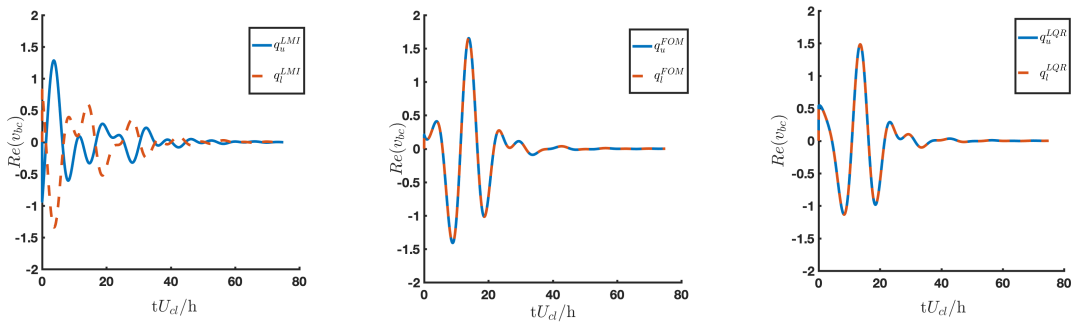

(a) LMI-ROM control **(b)** LQR-FOM control **(c)** LQR-ROM control

Figure 3.8: Actuated wall-normal velocity for $r = 40$, $(\alpha, \beta) = (1, 0)$, and $Re = 3000$.

In the oblique wave case of $(\alpha, \beta) = (1, 1)$, shown in Figure 3.9a, the LMI-ROM controller results in a maximum wall-normal blowing/suction velocity that is ≈ 1.6 times lower than either of the LQR controllers. From Figure ,3.9a we find that the q_u produces a control input of larger magnitude compared to q_l, i.e., the actuator on the upper-wall is inducing a larger velocity compared to the actuator on the lower-wall. In Figures, 3.9b and 3.9c the upper-wall and lower-wall actuators produce a velocity of

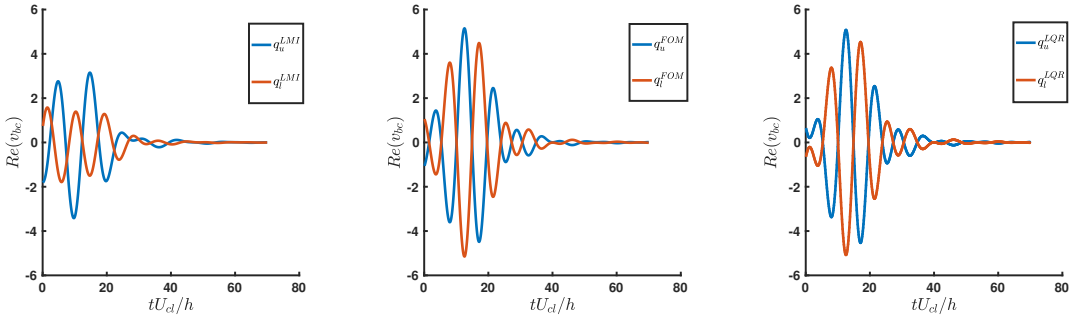

(a) LMI-ROM control **(b)** LQR-FOM control **(c)** LQR-ROM control

Figure 3.9: Actuated wall-normal velocity for $r = 58$, $(\alpha, \beta) = (1, 1)$, and $Re = 3000$.

similar magnitude but opposite directions relative to each other. In the oblique wave case, the 5% settling time of the actuation signal for the LMI-ROM controller is ≈ 41 convective time units, while the LQR-FOM and LQR-ROM each have a settling time of ≈ 37 convective time units. In the spanwise waves setting, shown in Figure 3.10, the LMI-ROM controller actuates the system similarly to both of the LQR controllers, but with a lower initial magnitude. For all controllers, wall-normal transpiration at the upper wall is identical to that at the lower wall (see Figure 3.10).

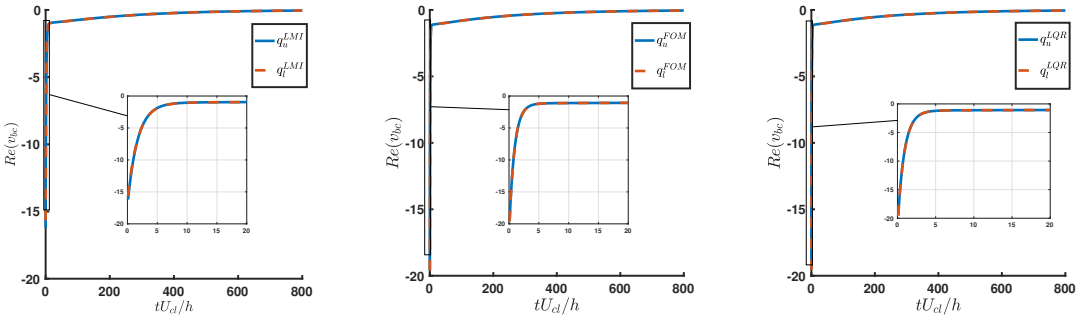

(a) LMI-ROM control **(b)** LQR-FOM control **(c)** LQR-ROM control

Figure 3.10: Actuated wall-normal velocity for $r = 40$, $(\alpha, \beta) = (0, 2)$, and $Re = 3000$.

3.6.4 Investigating the resulting flow field

Next, we examine the evolution of perturbations in streamwise velocity (u) to analyze the effect of the different controllers on the flow response. Figures 3.11 – 3.13 show the evolution of normalized u perturbations. The initial optimal perturbation has been normalized in these figures such that $E(0) = 1$. Figure 3.11 shows the response for the case of streamwise waves. Note that the LMI-ROM controller has a streamwise perturbation profile different from that of the LQR-ROM and the LQR-FOM. The u perturbations die out faster with the LMI-ROM controller than with either of the LQR controllers. The LQR-FOM and the LQR-ROM result in a similar evolution of u perturbation, as is to be expected from the similarity in TEG profiles we noted earlier in Figure 3.6a. In the case of oblique waves (see Figure 3.12), the LQR-ROM and LQR-FOM again yield a similar response in u-perturbations. In contrast to these responses, the LMI-ROM controller results in a reduced magnitude of u at the lower walls of the channel. Again, the LMI-ROM results in a faster decay of u perturbations than the LQR-ROM and LQR-FOM controllers. Finally, in the case of spanwise waves (see Figure 3.13), all the three controllers yield similar responses in u.

3.6.5 Accessing ROM and controller performance at various Re

Finally, we repeat our study for other Re values to ensure that the ROMs and controllers can be used in other settings as well. ROMs are developed and tuned to converge for $Re = 1000$, 5000, and $10,000$. Then, we follow the same procedure for control synthesis as in the $Re = 3000$ cases described earlier. Note that for the case of $Re = 10,000$, the flow is linearly unstable; thus, the balanced truncation procedure for the model reduction is only performed on the stable subspace of the linearized dynamics. Figures 3.14 and 3.15 report performance results for the cases of $(\alpha, \beta) = (1, 0)$ and $(1, 1)$, respectively. The results clearly show that the LMI-ROM controllers reduce TEG to a greater extent than the LQR controllers. However, with the increase in Re, the closed-loop response to the LMI-ROM control exhibits oscillations on a transient time scale, on the order of approximately 10^{-2} to 10^{-4} convective time units. The transient oscillations appear to be a property of the closed-loop system, which has a set of eigenvalues with large imaginary parts—on the order of 10^4—that lead to lightly

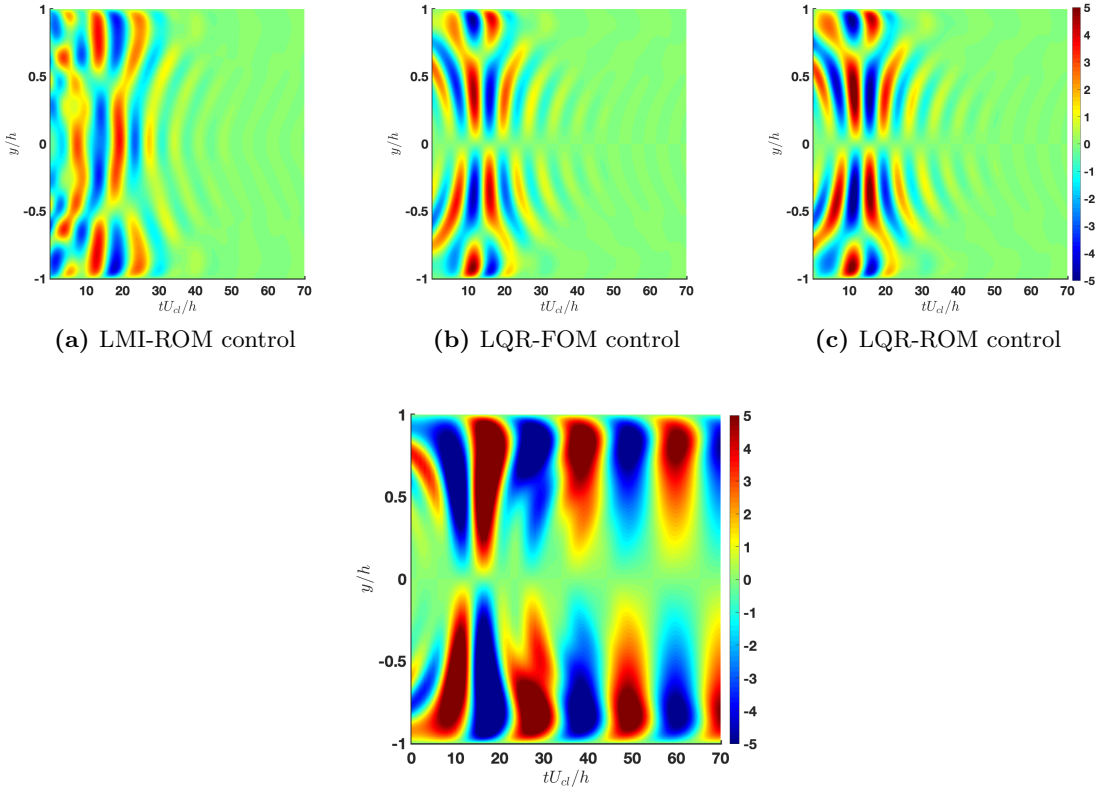

(a) LMI-ROM control **(b)** LQR-FOM control **(c)** LQR-ROM control

(d) Uncontrolled

Figure 3.11: Evolution of streamwise velocity perturbations (u) for $r = 40$, $(\alpha, \beta) = (1, 0)$, and $Re = 3000$.

damped oscillations. Further investigation is necessary to determine the the underlying cause of these transient oscillations and the observed spectral properties of the closed-loop system.

3.7 Conclusions

In this chapter, we have investigated the use of control-oriented ROMs for designing feedback controllers that minimize the MTEG of flow perturbations within a linearized channel flow. The ROMs were formed using an output projection onto POD modes, followed by a balanced truncation procedure to reduce the state dimension. POD modes were chosen to best approximate the perturbation energy, as needed for representing

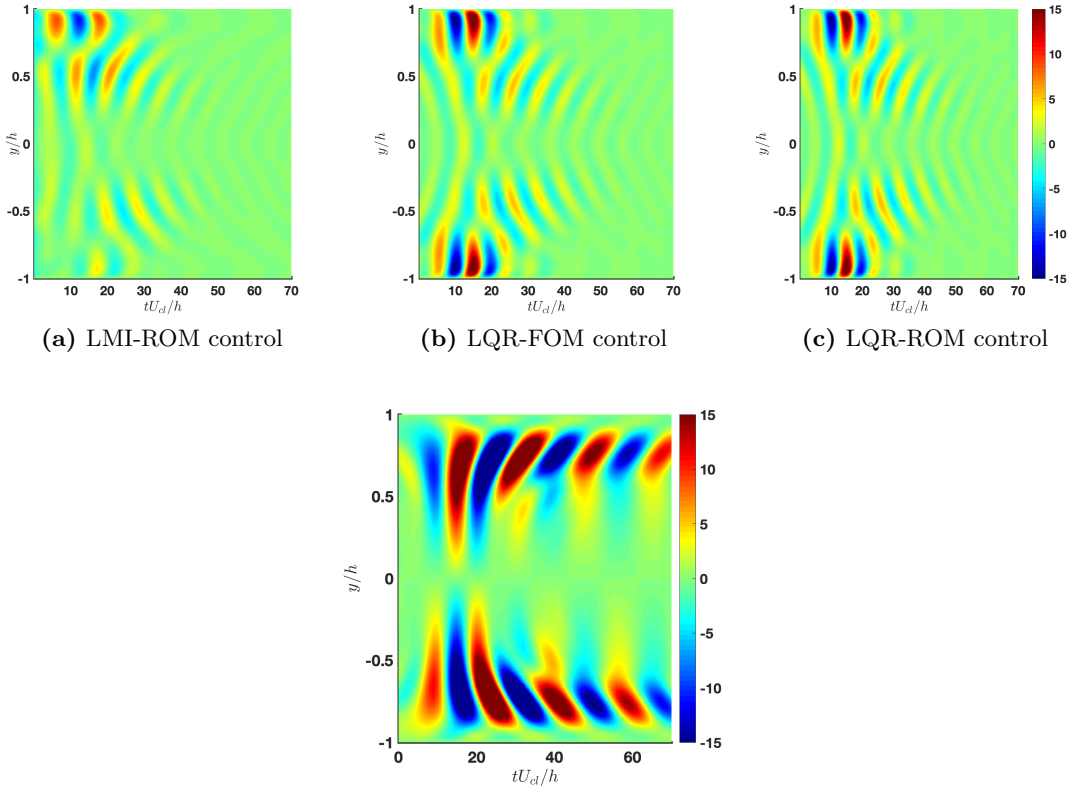

(a) LMI-ROM control **(b)** LQR-FOM control **(c)** LQR-ROM control

(d) Uncontrolled

Figure 3.12: Evolution of streamwise velocity perturbations (u) for $r = 58$, $(\alpha, \beta) = (1, 1)$, and $Re = 3000$.

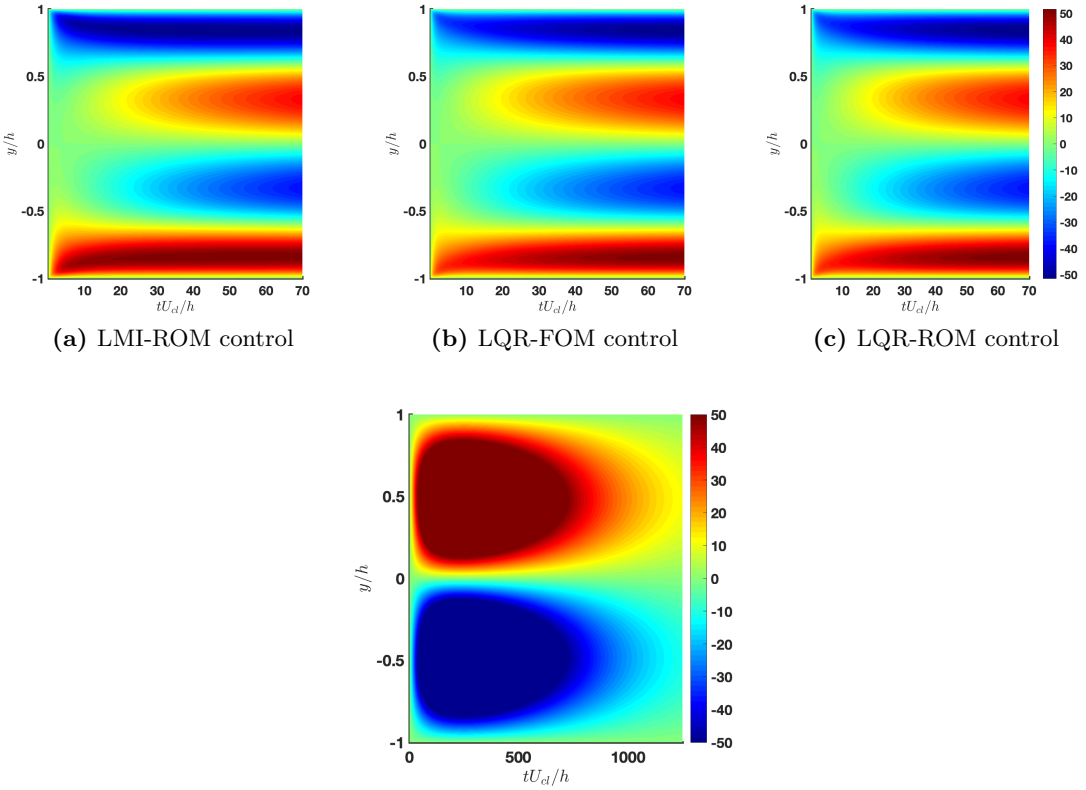

(a) LMI-ROM control **(b)** LQR-FOM control **(c)** LQR-ROM control

(d) Uncontrolled

Figure 3.13: Evolution of streamwise velocity perturbations (u) for $r = 40$, $(\alpha, \beta) = (0, 2)$, and $Re = 3000$.

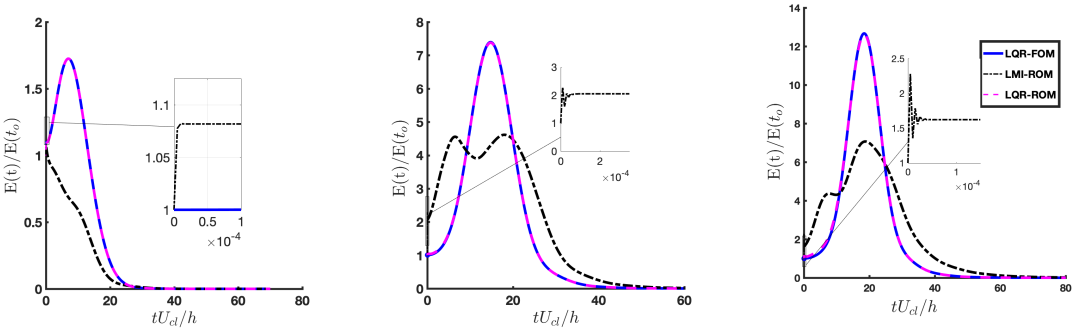

(a) $Re = 1000$ $(r = 40)$ **(b)** $Re = 5000$ $(r = 50)$ **(c)** $Re = 10,000$ $(r = 58)$

Figure 3.14: Worst-case closed-loop TEG responses for $(\alpha, \beta) = (1, 0)$.

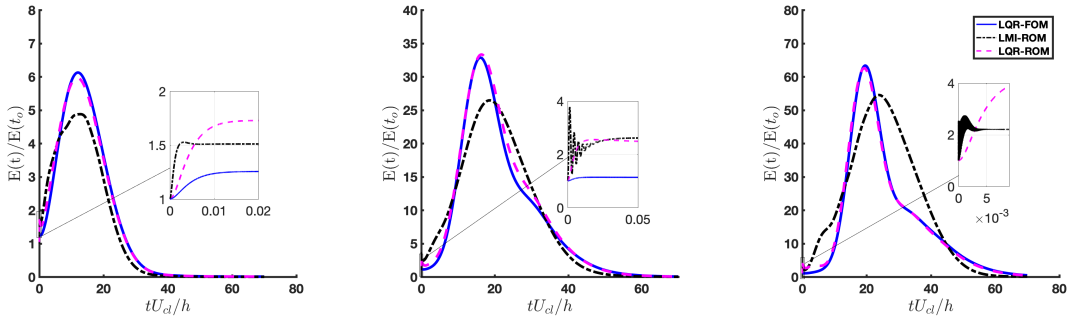

(a) $Re = 1000$ $(r = 40)$ **(b)** $Re = 5000$ $(r = 58)$ **(c)** $Re = 10,000$ $(r = 58)$

Figure 3.15: Worst-case closed-loop TEG responses for $(\alpha, \beta) = (1, 1)$.

the objective function for control. Note that this output projection does not alter the state dimension of the system. As such, a balanced truncation was performed to reduce the state dimension, retaining only state variables essential to preserving the system's input-output dynamics. ROMs of the linearized channel flow system enabled the synthesis of MTEG-minimizing controllers through the solution of an LMI problem that would otherwise have been computationally prohibitive. Specifically, the dimension of the full-order model ($n = 199$) was reduced to yield ROMs with order $r = 40 - 60$, depending on the specific configuration. This constitutes a significant reduction in the computational demand for the subsequent LMI-based controller synthesis, since the computational requirements for LMI-based controller synthesis scale as $\mathcal{O}(n^6)$. Further, the MTEG-minimizing controllers designed using the proposed ROMs were found to

outperform LQR controllers in suppressing TEG, even when these LQR controllers were designed based on the full-order system model. Although not explicitly reported here, the present investigation revealed that ROM-based MTEG-minimizing controllers can be sensitive to Re variations, leading to linearly unstable closed-loop systems when applied in "off-design" settings. As such, future investigations will need to focus on addressing these fragilities. It is expected that both the model reduction and controller synthesis approaches will need to be re-formulated to minimize MTEG robustly.

Another important takeaway observed from the DNS of the channel flow system suggests that growth of optimal disturbance alone cannot trigger a transition. The addition of a random perturbation of 1% of initial perturbation size can lead to transitions. Especially for oblique waves, with large perturbations, the linear feedback control strategy fails to suppress the transition and the flow transitions to a turbulent state [SH19]. Therefore, a simple study of the linear part alone, both for control and analysis, will not suffice. Therefore it is necessary to account for the nonlinear terms in the analysis as well. This will be the focus of the next few chapters.

Chapter 4

Part II: Quadratic Constraints Framework For Nonlinear Analysis of Transitional Flows

As we saw in the previous chapter, reducing TEG alone cannot delay the transition. This is predominantly due to the interplay between non-modal linear dynamics and quadratic nonlinearity in the incompressible NSE. In wall-bounded shear flows, the high degree of non-normality of the linearized NSE results in a transient energy growth (TEG) of small flow perturbations [SH01, Sch07, TTRD93], even when the dynamics are linearly asymptotically stable. As a result, TEG sends the trajectories to the stability boundary in the phase-space, after which secondary instabilities from the nonlinear terms lead to transition. Therefore, the linear analysis tends to over predict the critical Reynolds number (Re_c) for instability in many shear flows [Sch07, SH01, RH93b]. The fact that the flow transitions at Reynolds numbers (Re) below the predicted linear stability limit are partly attributed to the non-modal growth, which is necessary [Wal95b, Wal95a], but importantly we need to account for nonlinear terms that push the flow state away from the equilibrium base flow [TTRD93, SH01, Sch07, RH93b]. Nevertheless, non-modal TEG alone is not sufficient to cause transition: it is the interaction of non-modal TEG with the nonlinearity that triggers secondary instabilities and drives the state outside the region of attraction. Without the nonlinear terms, the notion of a finite region

of attraction would not make sense. Interestingly, although the nonlinearity is lossless and energy-conserving [SMML11, Wal95a], it can interact with the linear dynamics in such a way as to increase the maximum transient energy growth (MTEG) that can be realized [Ker18]. These transition scenarios cannot be fully analyzed without accounting for the nonlinear terms in the NSE.

Analysis methods have been proposed to account for the interplay between the linear and nonlinear terms using quadratic constraints in the context of systems with hard nonlinearities, uncertainties, nonlinear actuator dynamics [MR97]. In the fluid dynamics community, methods like Resolvent analysis, passivity analysis, and dissipation inequalities have leveraged the feedback mechanism between the linear and nonlinear terms in the flow. In this work, we leverage the interplay between linear and nonlinear terms to analyze nonlinear systems' stability. We extend the concept of quadratic constraints to analyze transitional flows.

The main idea behind this work is to account for previously ignored nonlinear terms and move towards a nonlinear analysis of the system. Here, we account for the nonlinear terms using their input-output properties, which are added as constraints to linear Lyapunov stability problem LMIs—allowing for a reduced-complexity analysis of the nonlinear system.

4.1 System Model and Lure' System

The Waleffe-Kim-Hamilton (WKH) model is a low-order mechanistic model for transition and sustained turbulence in shear flows. The model is based on observations from direct numerical simulations (DNS) of a plane Couette flow [WKH93], and was introduced to highlight the importance of nonlinear interactions with the non-normal linear dynamics in the NSE. The WKH model was studied in greater detail by Waleffe in [Wal95b] and is given by,

$$\begin{bmatrix} \dot{u} \\ \dot{v} \\ \dot{w} \\ \dot{m} \end{bmatrix} = \frac{1}{Re} \begin{bmatrix} 0 \\ 0 \\ 0 \\ \sigma \end{bmatrix} - \frac{1}{Re} \begin{bmatrix} \lambda u \\ \mu v \\ \nu w \\ \sigma m \end{bmatrix} + \begin{bmatrix} 0 & 0 & -\gamma w & v \\ 0 & 0 & \delta w & 0 \\ \gamma w & -\delta w & 0 & 0 \\ -v & 0 & 0 & 0 \end{bmatrix} \begin{bmatrix} u \\ v \\ w \\ m \end{bmatrix}. \tag{4.1}$$

Here, Re denotes the Reynolds number; u represents the amplitude of the spanwise modulation of streamwise velocity; v represents the amplitude of the streamwise rolls; w represents the the amplitude of the inflectional streak instability; and m represents the amplitude of the mean shear [Wal95b]. The constants λ, μ, ν, σ are positive parameters corresponding to viscous decay rates. The constants γ and δ represent nonlinear interaction coefficients and should have the same sign [Wal95b].

The WKH system in Eq. (4.1) captures the processes underlying sustained turbulence [Wal95b]: the rolls (v) create streaks (u) which eventually break down to maintain the rolls. In the WKH model, the mean shear m is not frozen in time and changes due to nonlinear interactions captured by the $-vu$ term. A few important aspects of this model are that the instability w grows from the streaks u via the γwu interaction term. It can also be observed that the same instability feeds streamwise rolls by nonlinear quadratic interactions δw^2. The nonlinear couplings between w and v are important in sustaining turbulence [Wal95b]. As we will show in Section 4.7, the importance of these same interactions in driving instabilities can be identified from our proposed analysis framework.

The WKH model admits a laminar equilibrium point at $(u, v, w, m)_e = (0, 0, 0, 1)$. For the proposed stability analysis, we perform a change of coordinates to translate the equilibrium point of Eq. (4.1) to the origin. The equilibrium point in these new coordinates is $\mathbf{x}_e = (0, 0, 0, 0)$ and the state is $\mathbf{x} = (u, v, w, \bar{m})$, where $\bar{m} = m - 1$. The system in this translated coordinate system is,

$$\underbrace{\begin{bmatrix}\dot{u}\\ \dot{v}\\ \dot{w}\\ \dot{\bar{m}}\end{bmatrix}}_{\dot{\mathbf{x}}} = \underbrace{\begin{bmatrix}-\frac{\lambda}{Re} & 1 & & \\ & -\frac{\mu}{Re} & & \\ & & -\frac{\nu}{Re} & \\ & & & -\frac{\sigma}{Re}\end{bmatrix}\begin{bmatrix}u\\ v\\ w\\ \bar{m}\end{bmatrix}}_{A\mathbf{x}} + \underbrace{\begin{bmatrix}0 & 0 & -\gamma w & v\\ 0 & 0 & \delta w & 0\\ \gamma w & -\delta w & 0 & 0\\ -v & 0 & 0 & 0\end{bmatrix}\begin{bmatrix}u\\ v\\ w\\ \bar{m}\end{bmatrix}}_{N(\mathbf{x})=Q(\mathbf{x})\mathbf{x}}, \tag{4.2}$$

which makes the non-normality of the linear dynamics explicit [Hen96]. The WKH system in Eq. (4.2) can be represented as

$$\dot{\mathbf{x}} = A\mathbf{x} + N(\mathbf{x}), \tag{4.3}$$

where the linear operator A is non-normal and asymptotically stable, and $N(\mathbf{x})$ is a quadratic nonlinearity given by $N(\mathbf{x}) = Q(\mathbf{x})\mathbf{x}$. Note that the nonlinear term is skew-symmetric: i.e., $Q(\mathbf{x}) = -Q(\mathbf{x})^T \in \mathbb{R}^{4\times 4}$. The linear and nonlinear terms can be partitioned into Lur'e form [Kha02], with the two systems acting in feedback with each other (see FIG. 4.1):

$$\dot{\mathbf{x}} = L(\mathbf{x}, \mathbf{z}) := A\mathbf{x} + \mathbf{z} \tag{4.4a}$$

$$\mathbf{z} = N(\mathbf{x}) \tag{4.4b}$$

where $\mathbf{z} \in \mathbb{R}^4$. This Lur'e decomposition of the WKH system is denoted as an upper linear fractional transformation $F_u(L, N)$. The advantage of writing this system in a Lur'e form is that Eq. (4.4a) alone is a linear dynamical system with an input $\mathbf{z}$. Although $\mathbf{z}$ is a nonlinear forcing given by Eq. (4.4b), we can instead account for it using input-output properties of $\mathbf{z} = N(\mathbf{x})$. In this way, we can perform a nonlinear analysis of the WKH model through analysis of linear dynamics in Eq. (4.4a) subject to constraints between $\mathbf{x}$ and $\mathbf{z}$ determined by Eq. (4.4b).

In all that follows, we study the proposed framework on the WKH system with two separate sets of parameters (see TABLE 5.1). Both sets of parameters have been investigated in prior studies: the Waleffe (W) parameters in [Wal95b], and the Baggett

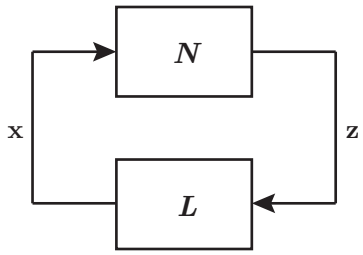

Figure 4.1: Lur'e representation of the WKH system $F_u(L, N)$.

and Trefethen (B&T) parameters in [BT97]. The W and B&T parameters each yield different behaviors in the system dynamics. The parameters chosen in this study result in notable differences in stability regions, permissible perturbation size, and transient energy growth [Wal95b, BT97].

In the remainder of this work, the only parameter varied for stability and transient energy growth analysis is Re. Other choices of parameters are possible and changing of the nonlinear interaction coefficients will lead to different types of bifurcations and correspondingly different stability regimes.

Parameter set	Parameter Value					
	λ	μ	ν	σ	δ	γ
W [Wal95b]	10	10	15	10	1	0.1
B&T [BT97]	1	1	1	1	1	1

Table 4.1: The two parameter sets and the value of the corresponding coefficients used in this work.

4.2 Nonlinear Stability Analysis: Lyapunov Stability

Lyapunov stability methods [Kha02] can be used to analyze the stability of a system given by Eq. (4.4). Here, the stability is analyzed around the equilibrium point $\mathbf{x}_e = \mathbf{0}$. To analyze stability using Lyapunov stability methods, we define a quadratic scalar energy function $V : \mathbb{R}^n \to \mathbb{R}$. The energy function $V(\mathbf{x}) = \mathbf{x}^T P \mathbf{x}$ is a candidate Lyapunov function [Kha02]. From theorem 1, we know the equilibrium point $\mathbf{x}_e = \mathbf{0}$ is asymptotically stable when $dV(\mathbf{x})/dt < 0 \; \forall \; \mathbf{x} \neq \mathbf{0}$, $t > 0$ and $P \succ 0$. In other words, the system is globally asymptotically stable around the equilibrium point $\mathbf{x}_e = \mathbf{0}$ if the

energy continuously decreases in time. The time derivative of the Lyapunov function for the nonlinear system in Eq. (4.4), along trajectories of the system is given by:

$$\begin{aligned} \frac{d}{dt}V(\mathbf{x}) &= 2\mathbf{x}^T P(A\mathbf{x}+\mathbf{z}) \\ &= 2\mathbf{x}^T P(A\mathbf{x}+N(\mathbf{x})). \end{aligned} \tag{4.5}$$

Including the effects of N($\mathbf{x}$) to analyze stability is crucial to understanding the global asymptotic stability of the nonlinear system. However, accounting for the nonlinear term N($\mathbf{x}$) complicates the stability analysis, and a quadratic Lyapunov function will not necessarily be a good choice as a candidate Lyapunov function. Here, we leverage the fact that the inputs and outputs of the nonlinearity N satisfy a set of quadratic constraints, thereby enabling stability analysis of the whole feedback interconnection $F_u(L, N)$ without the full complexity involved in an explicit treatment of the nonlinearity.

To do so, we first show that stability analysis benefits from consideration of the nonlinear term as energy-conserving and lossless, neither producing nor dissipating energy. The lossless property can be represented as a quadratic constraint to represent the nonlinear term within the Lyapunov analysis. The lossless constraint captures the global behavior of the nonlinearity. Further, we analyze the local behavior of the nonlinearity around a neighborhood by representing its local properties as "local" constraints. We also show that local nonlinear properties play a role in destabilizing the system, whereas a linear stability analysis predicts the WKH system to be globally asymptotically stable for all Re. Both global and local stability analysis and the results are discussed in the following sections.

In this work, the condition "$\forall t > 0$" is implied for all Lyapunov-based arguments, even without an explicit statement. Also, the relational operators $\prec 0$, $\succ 0$ ($\preceq 0$, $\succeq 0$) denote positive and negative (semi-) definite matrices, respectively.

4.3 Quadratic Constraints

4.3.1 Lossless Nonlinearity and Global Stability

The nonlinear term in Eq. (4.2) is skew-symmetric, therefore

$$\mathbf{x}^T N(\mathbf{x}) = \mathbf{x}^T Q(\mathbf{x})\mathbf{x} = 0, \ \forall \ \mathbf{x}. \tag{4.6}$$

The physical interpretation of this property is that the nonlinearity is energy conserving, serving only to redistribute energy between modes. This "lossless" property of the nonlinear term is also observed in many wall-bounded shear flows [SMML11]. The stability analysis reduces to the following question: Does the constraint in Eq. (4.6) imply $\dot{V}(\mathbf{x}) < 0$ in Eq. (4.5) for all $\mathbf{x} \neq \mathbf{0}$? The answer is yes, if there exists a $P \succ 0$ and a Lagrange multiplier ξ_0 (positive or negative) such that

$$2\mathbf{x}^T P(A\mathbf{x} + N(\mathbf{x})) + 2\xi_0 \mathbf{x}^T N(\mathbf{x}) < 0, \tag{4.7}$$

which essentially says that the energy function $V(\mathbf{x})$ decreases for any $\mathbf{x}$ and $N(\mathbf{x})$ satisfying the lossless constraint in Eq. (4.6).

Consider now that the lossless property in Eq. (4.6) can be expressed equivalently as a quadratic constraint between the inputs $\mathbf{x}$ and outputs $\mathbf{z} = N(\mathbf{x})$ of the nonlinearity:

$$\begin{pmatrix} \mathbf{x} \\ \mathbf{z} \end{pmatrix}^T \underbrace{\begin{pmatrix} \underline{0} & I \\ I & \underline{0} \end{pmatrix}}_{:=M_0} \begin{pmatrix} \mathbf{x} \\ \mathbf{z} \end{pmatrix} = 0, \ \forall \ \mathbf{x} \text{ and } \mathbf{z} \in \mathbb{R}^4, \tag{4.8}$$

where $\underline{0}, I \in \mathbb{R}^{4\times 4}$ denote the zero and identity matrices, respectively.

Thus, Eq. (4.7) can be recast as,

$$\begin{bmatrix} \mathbf{x} \\ \mathbf{z} \end{bmatrix}^T \left\{ \begin{bmatrix} A^T P + PA & P \\ P & \underline{0} \end{bmatrix} + \xi_0 M_0 \right\} \begin{bmatrix} \mathbf{x} \\ \mathbf{z} \end{bmatrix} < 0. \tag{4.9}$$

The lossless constraint $\mathbf{z}^T\mathbf{x} = 0$ is captured by the block matrix $M_0 \in \mathbb{R}^{8\times 8}$ defined in Eq. (4.8). The term in braces in Eq. (4.9) must be strictly negative definite for the strict inequality to be satisfied. However, for a matrix to be strictly negative definite, it is

necessary for all principle sub-matrices also to be strictly negative definite [Pru86, HJ90]. The bracketed term has $\underline{0}$ as a principle sub-matrix and hence the strict inequality in Eq. (4.9) cannot be satisfied. As such, we introduce a positive perturbation on Eq. (4.7) to relax the requirement for a strict inequality as,

$$2\mathbf{x}^T P(A\mathbf{x} + N(\mathbf{x})) + 2\xi_0 \mathbf{x}^T N(\mathbf{x}) + 2\epsilon \mathbf{x}^T P\mathbf{x} \leq 0, \tag{4.10}$$

where $\epsilon > 0$ This new condition is equivalent to $\dot{V}(\mathbf{x}) \leq -\epsilon V(\mathbf{x})$ for all $\mathbf{x} \neq \mathbf{0}$, which guarantees exponential stability with a minimum convergence rate of ϵ when satisfied.

The stability condition in Eq. (4.10) can be recast in terms of the quadratic lossless constraint in Eq. (4.8) to yield,

$$\begin{bmatrix} \mathbf{x} \\ \mathbf{z} \end{bmatrix}^T \left\{ \begin{bmatrix} A^T P + PA & P \\ P & \underline{0} \end{bmatrix} + \xi_0 M_0 + \begin{bmatrix} \epsilon P & \underline{0} \\ \underline{0} & \underline{0} \end{bmatrix} \right\} \begin{bmatrix} \mathbf{x} \\ \mathbf{z} \end{bmatrix} \leq 0. \tag{4.11}$$

Unlike the stability condition in Eq. (4.9), it is possible for this new stability condition in Eq. (4.11) to be satisfied because the inequality is non-strict. For Eq. (4.11) to hold, the matrix in braces has to be negative semi-definite. However, from the generalized Schur's complement [Gal10] we know that the bracketed term will be negative semi-definite if and only if both $A^T P + PA + \epsilon P \preceq 0$ and $P + \xi_0 I = 0$ for some $\xi_0 < 0$. Note that the condition $A^T P + PA + \epsilon P \preceq 0$ is the condition for verifying exponential stability of the linear system and by itself does not account for the nonlinearity; the addition of the quadratic constraints accounts for the lossless nonlinearity in this stability condition. In the limit $\epsilon \to 0$, this condition is equivalent to $A + A^T \prec 0$, which is a necessary and sufficient condition for unity maximum transient energy growth due to linear non-modal dynamics, as shown in Lemma 1. Thus, our analysis is consistent with the fact that unity linear MTEG is necessary for global stability in the nonlinear system. In light of the stability condition in (4.11), it follows that stability of the linear element L and a lossless nonlinearity can be formulated as an LMI feasibility problem in the variables $P \succ 0$ and ξ_0. In particular, the system $F_u(L, N)$ is globally asymptotically stable if

there exists $P \succ 0$ and ξ_0 such that the following LMI holds for a given $\epsilon > 0$:

$$\begin{bmatrix} A^T P + PA & P \\ P & \underline{0} \end{bmatrix} + \xi_0 M_0 + \begin{bmatrix} \epsilon P & \underline{0} \\ \underline{0} & \underline{0} \end{bmatrix} \preceq 0. \tag{4.12}$$

The feasibility of the LMI in Eq. (4.12) is only sufficient to establish the global asymptotic stability of the WKH system, as it only relies on the lossless property and does not depend on any other specific details of the nonlinearity. The condition in Eq. (4.12) is an LMI feasibility problem that can be solved using standard numerical tools. Unless otherwise specified, in the remainder of this work, we use CVX [GB14, GB08], which is a package for specifying convex optimizations, combined with the commercially available solver MOSEK [ApS19].

To analyze the global stability of the WKH system, we solve the LMI in Eq. (4.12) with $\epsilon = 10^{-6}$ for variables P and ξ_0 at different values of Re. On performing the global stability analysis using the lossless constraint, we find that the WKH model for the W parameter values (see TABLE 5.1) is globally asymptotically stable for $Re \leq 20$. This finding is consistent with $Re_c = 20$ for global asymptotic stability reported by Waleffe [Wal95b]. Similarly, we find that the WKH system with B&T parameters (see TABLE 5.1) is globally asymptotically stable for $Re \leq 2$.

Note that the linear WKH system is globally asymptotically stable for all Re, and so the nonlinear term is destabilizing. In the nonlinear WKH system, considering only the lossless constraint, it is shown that global stability cannot be established for $Re > 20$ for the W parameters and $Re > 2$ for the B&T parameters. To investigate this further, we propose a set of local constraints on the nonlinearity that enable a local stability analysis, as described in the next section.

4.3.2 Local Stability Analysis: Quadratic Constraints on Spherical Sets

The WKH system with the lossless constraint is globally asymptotically stable for $Re \leq 20$ for the W parameters and for $Re \leq 2$ for the B&T parameters. To analyze the system for larger Re, we propose a "local" stability analysis as follows: Select a local neighborhood $\|\mathbf{x}\|^2 \leq \alpha^2$ around the equilibrium point $\mathbf{x}_e = \mathbf{0}$. Local analysis restricts

the state $\mathbf{x}$ to lie in a local region α, which results in "local" constraints for $N(\mathbf{x})$ within this local region. The analysis condition, given below, attempts to use these local quadratic constraints to show that: (i) the system state remains within the local region and (ii) it converges asymptotically back to $\mathbf{x}_e = \mathbf{0}$. These quadratic constraints are tighter (more powerful) for smaller values of α and become looser (less powerful) as α becomes larger. Thus, these local analysis results provide a range of results between global asymptotic stability (roughly as $\alpha \to \infty$) and stability of the linearized system (roughly as $\alpha \to 0$). We will show later in this section that α can be used to estimate the region of attraction (ROA) for the equilibrium point.

Recall that the nonlinearity in the WKH model is quadratic and can be expressed as $\mathbf{z} = \mathbf{x}^T Q(\mathbf{x})\mathbf{x}$ (see Eq. (4.2)). To illustrate the approach, first consider the scalar example $z = x^2$ (green curve in FIG. 4.2). Within a given region $|\mathbf{x}| < \alpha$, the output satisfies $z^2 = x^4 < \alpha^2 x^2$. Which further implies that $|z| < \alpha|x|$, where α is the slope of the line. The bound *alpha* restricts the quadratic function, but this bound would graphically correspond to drawing a line of slope $+\alpha$ and $-\alpha$ (red lines in FIG. 4.2). The slope α can have a large or small value, as illustrated in FIGs. 4.2a and 4.2b, respectively. If x remains in the interval $[-\alpha, +\alpha]$, then the nonlinear function lies between these two linear lines with slope $\pm\alpha$ (gray shaded region in FIGs. 4.2a and 4.2b). The dashed blue line in both these figures represents the maximum possible value of the pair (x, z), such that $|x| \leq \alpha$ for a given slope. It can be seen that as the slope α is made larger (FIG. 4.2a), then the pair (x, z) also gets bigger, thereby moving the blue dashed line further away from the origin. Similarly, as the slope of α is made smaller (FIG. 4.2b), the pair (x, z) gets smaller, thereby moving the dashed line towards the origin, which corresponds to a reduction in the maximum value of z. Finally, note that the sector shrinks to zero as the slope α tends to zero. Thus, $\alpha \to 0$ corresponds to a nonlinear term with zero output—equivalent to a linear analysis. Conversely, as $\alpha \to \infty$, then this sector becomes arbitrarily large and provides essentially no information—corresponding to a global analysis.

The sector formed by lines of slope $\pm\alpha$ facilitates bounding the pair (x, z) to perform analysis in a localized setting, where the value of α also determines the amount of nonlinear behavior captured by the local constraint. The remainder of this section generalizes this basic concept to the multivariable quadratic terms that appear in the

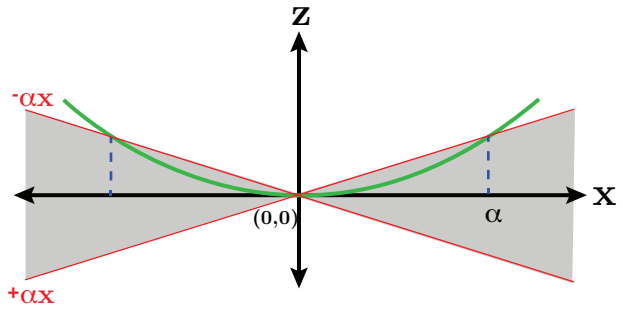

(a) Large slope α forms larger sectors

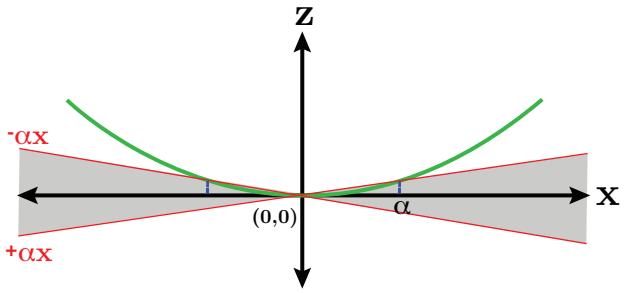

(b) Small slope α forms smaller sectors

Figure 4.2: Illustration of a scalar quadratic function $x = z^2$ (green) that lies inside the sector formed by lines of slope $-\alpha$ and α (red). The blue dashed lines mark the maximum value of the pair (x, z) for a given slope such that $|x| \leq \alpha$.

WKH model.

From Eq. (4.2), each individual nonlinear term can be expressed as a quadratic function:

$$\mathbf{z} = \begin{bmatrix} z_1 \\ z_2 \\ z_3 \\ z_4 \end{bmatrix} = \begin{bmatrix} \mathbf{x}^T Q_1 \mathbf{x} \\ \mathbf{x}^T Q_2 \mathbf{x} \\ \mathbf{x}^T Q_3 \mathbf{x} \\ \mathbf{x}^T Q_4 \mathbf{x} \end{bmatrix}. \tag{4.13}$$

Here each $Q_i \in \mathbb{R}^{4\times 4}$ is a symmetric matrix. Hence each Q_i has real eigenvalues, and the spectral radius $\rho(Q_i)$ denotes the largest (magnitude) of these eigenvalues [HJ90]. Moreover, quadratic terms with symmetric matrices are upper bounded as follows [HJ90]:

$$|z_i| = |\mathbf{x}^T Q_i \mathbf{x}| \leq \rho(Q_i)\mathbf{x}^T\mathbf{x}, \text{ for } i = 1 \text{ to } 4. \tag{4.14}$$

Next, assume the state $\mathbf{x}$ remains within a ball of radius α, i.e. $\mathbf{x}^T\mathbf{x} \leq \alpha^2$. We can then square Eq. (4.14) to obtain the following constraint:

$$z_i^2 \leq \underbrace{\rho(Q_i)^2\alpha^2}_{\kappa_i(\alpha)^2}\mathbf{x}^T\mathbf{x}, \text{ for } i = 1 \text{ to } 4. \tag{4.15}$$

This is a constraint involving squares of $\mathbf{x}$ and z_i. It can be written in a more useful quadratic constraint form. Let $\mathbf{e}_i \in \mathbb{R}^4$ is the standard basis with i^{th} element as 1 and $e_i e_i^T$ denotes the matrix with the diagonal (i,i) entry equal to one and all other entries equal to zero. The constraint in Eq. (4.15) is equivalent to:

$$\begin{bmatrix}\mathbf{x}\\ \mathbf{z}\end{bmatrix}^T \underbrace{\begin{bmatrix}\kappa_i(\alpha)^2 I & \underline{0}\\ \underline{0} & -\mathbf{e}_i\mathbf{e}_i^T\end{bmatrix}}_{M_i(\alpha)} \begin{bmatrix}\mathbf{x}\\ \mathbf{z}\end{bmatrix} \geq 0, \text{ for } i = 1 \text{ to } 4. \tag{4.16}$$

Throughout this work $\underline{0}$ and I are used to represent the zero and identity matrices of appropriate dimensions, respectively. The above multivariable quadratic constraint in Eq. (4.16) are the sector constraint [BEFB94a]. The above constraint provides a bound on the nonlinear term z_i that holds over the local region $\mathbf{x}^T\mathbf{x} \leq \alpha^2$. A local bound can be obtained for each of the four quadratic nonlinearities in Eq. (4.16). It should be noted that the lower right block in each $M_i(\alpha)$ matrix is non-zero, and so we can use the strict inequality $\dot{V}(\mathbf{x}) + \xi_0 M_0 + \sum_{i=0}^{4} \xi_i M_i < 0$. We will make use of these local constraints to study the local stability of the WKH system in section 4.4 and show that they can be used for transient energy growth analysis as well in Section 4.6.2.

4.4 Region of Attraction

The lossless property in Eq. (4.8) captures the global behavior of the quadratic nonlinearity. Given that the WKH system is not globally stable for $Re > 20$, it is still beneficial to understand its local stability properties. The linearization around $\mathbf{x}_e = \mathbf{0}$

is stable for all $Re > 0$ because A is Hurwitz. A more quantitative local stability analysis can be performed around $\mathbf{x}_e = \mathbf{0}$ using the local constraints derived in Eq. (4.16). Specifically, our goal is to estimate the region of attraction (ROA), which corresponds to the set of initial conditions whose trajectories converge back to $\mathbf{x}_e = \mathbf{0}$. We will consider the local constraints on the nonlinearity that hold over the sphere $\|\mathbf{x}\| \leq \alpha$. The local stability analysis for the nonlinear system can be performed by solving the following LMI feasibility problem:

$$\begin{aligned} & P \succeq I \\ & \xi_i \geq 0 \qquad (\text{for } i = 1 \text{ to } 4) \\ & \begin{bmatrix} A^T P + PA & P \\ P & \underline{0} \end{bmatrix} + \xi_0 M_0 + \sum_{i=1}^{4} \xi_i M_i(\alpha) \prec 0. \end{aligned} \tag{4.17}$$

Note that the local quadratic constraints depend on the radius α as explicitly denoted by $M_i(\alpha)$. If Eq. (4.17) has a feasible solution, then $V(\mathbf{x}) = \mathbf{x}^T P \mathbf{x}$ is a Lyapunov function. Moreover, the level set $S_\alpha := \{\mathbf{x} : V(\mathbf{x}) < \alpha^2\}$ is an inner approximation to the region of attraction (ROA). These facts are formally proved here.

The role of α in this analysis can be made more precise. Assume there is a feasible solution $P > 0$ for the linear matrix inequality in Eq. (4.17). Then the Lyapunov function $V(\mathbf{x}) = \mathbf{x}^T P \mathbf{x}$ satisfies $dV(\mathbf{x}(t))/dt < 0$ as long as $\mathbf{x}(t)^T \mathbf{x}(t) \leq \alpha^2$. This implies that trajectories converge back to $\mathbf{x}_e = 0$ if the initial conditions are sufficiently close to the origin. In particular, the constraint $P > I$ implies that $\mathbf{x}^T \mathbf{x} < V(\mathbf{x})$.

Theorem 2. *If $V(\mathbf{x}(0)) < \alpha^2$ then: (i) the trajectory $\mathbf{x}(t)$ remains in the local region $\|\mathbf{x}(t)\|^2 \leq \alpha^2$ and (ii) the trajectory $\mathbf{x}(t)$ decays to the origin. In summary, the set $S_\alpha := \{\mathbf{x} : V(\mathbf{x}) < \alpha^2\}$ is a domain of attraction.*

Proof. Define the set $S_\alpha := \{\mathbf{x} : V(x) < \alpha^2\}$. Assume $\mathbf{x}(0) \in S_\alpha$ and let $\mathbf{x}(t)$ denote the corresponding state trajectory from this initial condition. Assume there exists a time T_1 such that $\mathbf{x}(T_1) \notin S_\alpha$ and let T_0 be the smallest (infimum) of times such that $\mathbf{x}(t) \notin S_\alpha$. The solution $\mathbf{x}(t)$ is a continuous function of time and hence $\mathbf{x}(t) \in S_\alpha$ for all $t \in [0, T_0)$ and, moreover, $\mathbf{x}(t)$ is on the boundary of S_α so that $V(\mathbf{x}(T_0)) = \alpha^2$.

As noted above, $P > I$ implies that if $\mathbf{x}(t) \in S_\alpha$ then $\|\mathbf{x}(t)\|^2 < \alpha^2$. Therefore, the local quadratic constraints are valid for all $t \in [0, T_0]$. The constraints in Eq. (4.17) imply that, for a sufficiently small $\epsilon > 0$, the Lyapunov function satisfies $dV(\mathbf{x}(t))/dt \leq -\epsilon \mathbf{x}(t)^T \mathbf{x}(t)\ \forall\ t \in [0, T_0]$. Integrating yields the following bound for any $\mathbf{x}(0) \neq 0$:

$$V(\mathbf{x}(T_0)) \leq V(\mathbf{x}(0)) < \alpha^2 \tag{4.18}$$

This contradicts the assumption that $V(\mathbf{x}(T_0)) = \alpha^2$ and hence trajectories must remain in S_α. Moreover, the Lyapunov condition $dV/dt \leq -\epsilon \mathbf{x}(t)^T \mathbf{x}(t)\ \forall\ t \in [0, T_0]$ implies that the trajectories in this region decay asymptotically back to the origin. □

For a given Re and α, we solve the feasibility problem in Eq. (4.17). If the problem is feasible for a region of size α, we know that the problem is also feasible for a region whose size is smaller than α as well. This enables us to use bisection to obtain the lower bound on α. However, solving the feasibility problem via bisection for numerous α can be computationally cumbersome. Hence, we re-pose the problem for finding the largest lower bound on α as a quasi-convex generalized eigenvalue problem (GEVP) [BG93].

To find the estimate of the largest inner approximation for the ROA, we first decompose each local constraint matrix $M_i(\alpha)$ as

$$M_i(\alpha) = \alpha^2 \underbrace{\begin{bmatrix} \rho(Q_i)^2 & \underline{0} \\ \underline{0} & \underline{0} \end{bmatrix}}_{\tilde{M}_i} + \underbrace{\begin{bmatrix} \underline{0} & \underline{0} \\ \underline{0} & -\mathbf{e}_i \mathbf{e}_i^T \end{bmatrix}}_{\hat{M}_i}. \tag{4.19}$$

Now an estimate for the ROA can be obtained by using a change of variables $t = -\alpha^2$ and solving the GEVP,

$$
\begin{aligned}
&\text{minimize} \quad t \\
&\text{subject to } P \succeq I \\
&\qquad \xi_i \geq 0 \qquad (\text{for } i = 1 \text{ to } 4) \\
&\qquad \begin{bmatrix} A^T P + PA & P \\ P & \underline{0} \end{bmatrix} + \xi_0 M_0 + \sum_{i=1}^{4} \xi_i \hat{M}_i \prec t \sum_{i=1}^{4} \xi_i \tilde{M}_i,
\end{aligned} \tag{4.20}
$$

where ξ_i ($i = 1$ to 4) are Lagrange multipliers for the local constraints. These Lagrange multipliers also provide information on the relative contribution of each constraint in the local region, as will be discussed in Section 4.7. In this work, the GEVPs are solved using LMI-Lab [GN93].

The analysis condition in Eq. (5.9) can be used to estimate the largest lower bound of α as a function of Re. The resulting relationship between Re and α is shown in FIG. 4.3. Note that α decreases monotonically as Re tends to ∞. This implies that the local stability region shrinks as Re increases. On the other hand, α tends to ∞ as Re decreases to 20, as shown in FIG. 4.3a for the W parameter case. In the W parameter case, the local stability region increases in size as $Re \to 20$. This is consistent with the previous global stability result, where $Re \leq 20$ was globally stable using only the lossless constraint.

Similarly, we also analyze the local stability for the B&T parameters in FIG. 4.3b. Here, the system is globally stable for $Re \leq 2$, demarcated by the dashed red line in FIG. 4.3b. The same relation between α and Re is observed with the B&T parameter as with W parameters; that is, the size of α is decreasing with increasing Re.

4.5 Largest Permissible Perturbations

We have shown that the GEVP in Eq. (5.9) can be solved to obtain the largest lower bound on α. Now we aim to identify the largest perturbation size R_0, such that trajectories originating in a sphere of radius R_0 will converge back to the equilibrium. The sphere of radius R_0 is obtained by finding the largest inner approximation of the ROA—this sphere is a sub-level set of the ellipsoid $V(\mathbf{x}) \leq \alpha^2$. The size and shape of

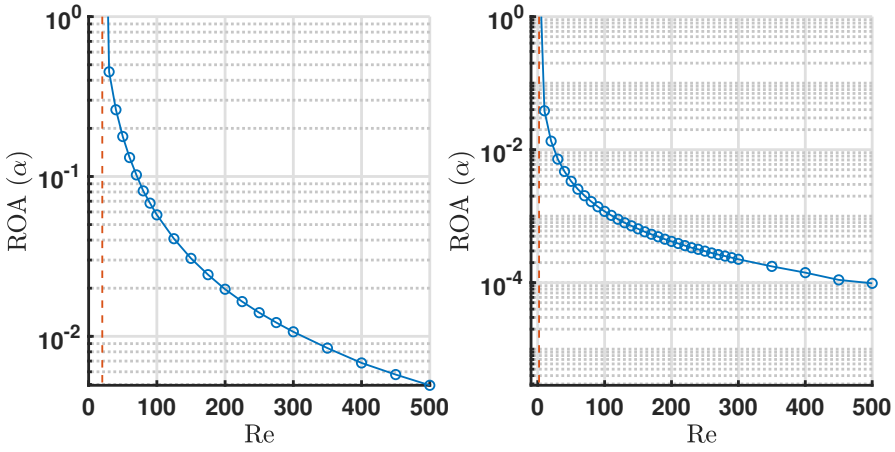

(a) W parameter **(b)** B&T parameter

Figure 4.3: As the Re is increased, the local stability region α decreases. The red dashed line shows the Re for global stability limit. In both (a) and (b) as we approach the global stability limit, the size of $\alpha \to \infty$. As $Re \to \infty$, the size of region $\alpha \to 0$, which corresponds to the linear analysis of infinitesimal perturbations.

the ellipsoid depend on the energy weight matrix P found in Eq. (5.9). We will show that the GEVP can be used to estimate the largest perturbation amplitude R_0 that drives the trajectory to the edge of stability.

Consider initial conditions inside a sphere of radius R_0 around the equilibrium point such that $||\mathbf{x}_0||^2 \leq R_0^2$. Let $q := \lambda_{max}(P)/\lambda_{min}(P)$ be the condition number of P with λ_{max} and λ_{min} being the largest and smallest eigenvalues of P, respectively. The condition number q of matrix P provides information on the skewness of the bounding ellipsoid. To bound the skewness of the elliptical set, we can simply bound P as $I \preceq P \preceq qI$. We now seek to determine the largest sphere of initial conditions $\|\mathbf{x}_0\|^2 \leq R_0^2$ such that trajectories remain inside the ROA. From the inequality $I \preceq P \preceq qI$ and $\dot{V}(\mathbf{x}) < 0$, it follows that $\|\mathbf{x}\|^2 \leq \mathbf{x}^T P \mathbf{x} \leq \mathbf{x}_0^T P \mathbf{x}_0 \leq q\|\mathbf{x}_0\|^2$, which implies that $\|\mathbf{x}\|^2 \leq q\|\mathbf{x}_0\|^2$. Therefore, we have $\|\mathbf{x}\|^2 \leq qR_0^2 = \alpha^2$, and we can find the largest allowable sphere of radius R_0. To do so, we can now use the decomposition of $M_i = \alpha^2 \tilde{M}_i + \hat{M}_i$ (see Eq. (4.19)) and the relation $\alpha^2 = qR_0^2$, then solve the following GEVP

$$
\begin{aligned}
&\text{minimize} \quad t_0 \\
&\text{subject to } I \preceq P \preceq qI \\
&\qquad \xi_i \geq 0 \qquad \text{(for i=1 to 4)} \\
&\qquad \begin{bmatrix} A^T P + PA & P \\ P & \underline{0} \end{bmatrix} + \xi_0 M_0 + \sum_{i=1}^{4} \xi_i \hat{M}_i \prec t_0 q \sum_{i=1}^{4} \xi_i \tilde{M}_i,
\end{aligned} \tag{4.21}
$$

where $t_0 = -R_0^2$. To solve for the largest permissible perturbation amplitude, we solve Eq. (4.21) over a grid of q values, then pick the solution corresponding to the largest R_0.

4.5.1 Benchmarking results

We verify our findings by comparing the R_0 obtained from the proposed quadratic constraints (QC) framework with the nonlinear optimal perturbations obtained using nonlinear direct-adjoint looping (DAL) and sum-of-squares (SOS) method. In the DAL method, as detailed in [KPW14, Ker18], a so-called "minimal seed" is obtained using the calculus of variations and a gradient method to find the nonlinear optimal perturbation on a sphere of radius R_0. If divergent trajectories are found for perturbations of size R_0, we update the upper and lower bounds on R_0 via bisection. Once the upper and lower bounds converge to some tolerance $\epsilon > 0$ (here $\epsilon = 10^{-8}$) and no divergent trajectories are found, we terminate the bisection procedure. Since DAL uses the exact nonlinear equations of motion, it provides accurate estimates for the minimal seed of the nonlinear system and the permissible amplitude; hence it is a good method to benchmark the QC framework results. In addition to the DAL method, we also compare with results from the SOS framework using quadratic energy functions [GC12]. Both the SOS and QC framework use Lyapunov-based methods to compute the largest sphere of radius R_0, which is an inner approximation of the ROA. Hence, these methods are conservative in their estimates of the permissible perturbation amplitude. A brief overview of the SOS technique is provided in the appendix A. Here, SOSOPT [BPST], a Matlab toolbox for SOS optimization problems, is used to obtain the results presented here.

In FIG. 4.4, we report the largest radius of initial conditions R_0^* versus Re using

the three methods mentioned above. For the B&T parameters, we show results of the DAL ($\triangle$), SOS framework ($\square$), and QC framework ($\bigcirc$) in FIG. 4.4b. However, for the W parameters, we compare the SOS framework and QC framework results only in FIG. 4.4a. This is because, for the W parameters, no divergent trajectories were found using DAL. Even though there are no divergent trajectories, the SOS framework and QC framework provide conservative estimates for R_0, as expected.

For the B&T parameters, the largest allowable perturbation size for $Re = 100$ is found to be $R_0^* \approx 1.5 \times 10^{-5}$ using the QC framework; this is a conservative estimate relative to $R_0^* = 10^{-4}$ in [BT97]. As seen in both figures in FIG. 4.4, we observe that the R_0^* predicted by the QC framework is conservative. Since the QC framework does not use detailed information of the nonlinear terms, it only uses a few constraints that characterize the nonlinear terms' input-output behavior– this behavior is expected. In exchange for this conservatism, the QC framework is less computationally expensive than the SOS and DAL methods, which are more computationally expensive and may not be suitable for large systems.

4.6 Maximum Transient Energy Growth

This section aims to determine the least upper bound on the maximum transient energy growth (MTEG) in the nonlinear system using the QC framework. We first review how the MTEG bounds can be obtained for a linear system by solving a GEVP. We then extend this GEVP to determine the MTEG in the nonlinear system using the QC framework.

As it can be seen, the linear part of the WKH system is non-normal; the system is stable and holds TEG due to the non-normality. Again, the system's energy is $E := \mathbf{x}^T\mathbf{x}$. Due to the non-normality in the system, estimating the maximum possible energy growth the system might hold is important. This problem of identifying the MTEG in the linear system is given in Section 2.4.4. This section extends the linear MTEG analysis presented in Section. 2.4.4 using quadratic constraints to study how the nonlinear systems MTEG is affected.

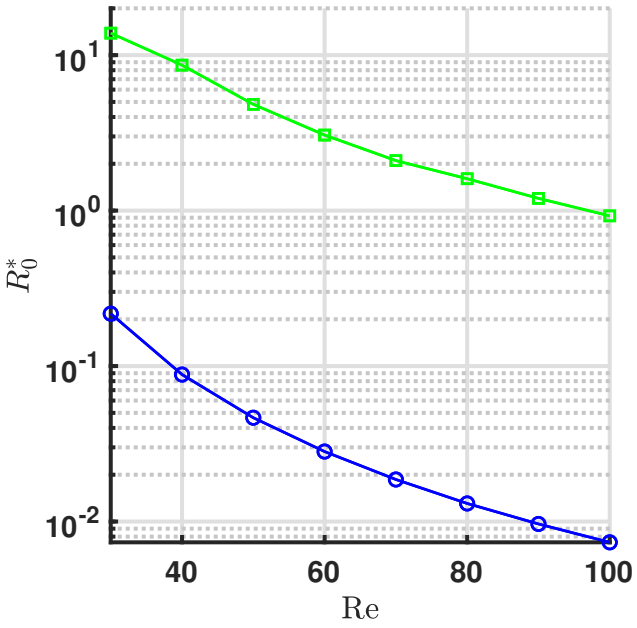

(a) W parameters

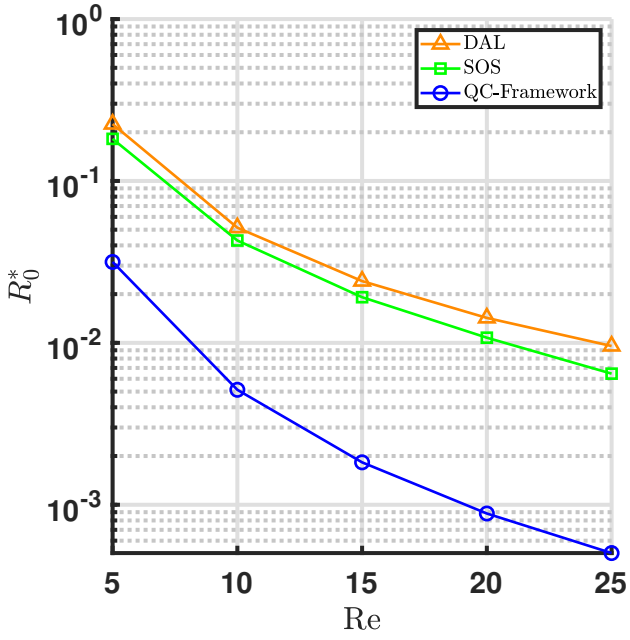

(b) B&T parameters

Figure 4.4: The maximum allowable perturbation size R_0 as a function of Re for W and B&T parameters compared against the SOS framework and DAL method.

4.6.1 Global MTEG Analysis using Quadratic Constraints

An optimization problem similar to Eq. (2.15) can be formulated to study the MTEG in the nonlinear WKH system. The lossless property for the nonlinear term in Eq. (4.8) can again be used as a global constraint. Taking a similar approach as in Section 4.3.1, we perturb the Lyapunov inequality to ensure a feasible solution can exist when only the lossless constraint is used. This yields the following optimization for a given $\epsilon > 0$:

$$\begin{aligned} q^* := \text{minimize} \quad & q \\ \text{subject to } & I \preceq P \preceq qI \ , \\ & \begin{bmatrix} A^T P + PA & P \\ P & \underline{0} \end{bmatrix} + \xi_0 M_0 + \begin{bmatrix} \epsilon P & \underline{0} \\ \underline{0} & \underline{0} \end{bmatrix} \preceq 0 \end{aligned} \tag{4.22}$$

Equation (4.22) is now a SDP in the variables (P, q, ξ_0). As before, the LMI constraints imply that the Lyapunov function evaluated at the initial time upper bounds the Lyapunov function for all $t \geq 0$. The bounds on P imply that $E(t) \leq q^* E(0)$ and are obtained employing a Lyapunov function that describes a trajectory bounding ellipsoid, known as an invariant set. As with the linear MTEG analysis in Eq. (2.15), the quadratic constraint analysis problem in Eq. (4.22) is expected to yield a conservative upper bound on MTEG.

4.6.2 Local MTEG Analysis using Quadratic Constraints

The ability to obtain MTEG bounds is of interest even beyond the globally stable regime considered in Section 4.6.1. Hence, we use the local properties of the nonlinearity derived in Section 4.4 to study the "local" MTEG performance in the nonlinear system.

A formulation similar to Eq. (4.22) can be used to study the effect of nonlinearity on MTEG in the nonlinear system. To perform the local MTEG analysis, additional local constraints are added to the optimization problem listed in Eq. (4.22). The local constraints that capture input-output properties of the nonlinear term are captured by matrices M_i (for $i = 1$ to 4) defined in Eq. (4.19). The addition of these constraints facilitates the study of local MTEG on the nonlinear system. The local MTEG for the nonlinear system is computed via the following convex optimization:

$$
\begin{aligned}
&\text{minimize} \quad q \\
&\text{subject to } I \preceq P \preceq qI \ , \\
&\qquad \xi_i \geq 0 \qquad (\text{for } i = 1 \text{ to } 4) \ , \\
&\qquad \begin{bmatrix} A^T P + PA & P \\ P & \underline{0} \end{bmatrix} + \xi_0 M_0 + \sum_{i=1}^{4} \xi_i M_i \prec 0.
\end{aligned} \tag{4.23}
$$

We will identify MTEG bounds for the system about a local equilibrium point $\mathbf{x}_e = \mathbf{0}$ by solving this optimization for $P,\ q, \xi_0,$ and ξ_i (for $i = 1$ to 4). The proof in theorem 2 also applies for Eq. (4.23), therefore ensuring the states always remain inside the invariant set for all time $t \geq 0$.

4.6.3 Results: MTEG analysis using quadratic constraints

Global MTEG analysis

By solving the SDP in Eq. (4.22) with $\epsilon = 10^{-6}$, we find that the MTEG bound is unity for all $Re < 20$ using the W parameters. It is interesting to note that the linear part of the WKH system exhibits unity MTEG for $Re < 20$ as well. Yet, the same MTEG bound from Eq. (4.22) is stronger because it applies to the nonlinear system $F_u(L, N)$ with a lossless nonlinearity. Similarly, from global MTEG analysis of the WKH system with B&T parameters, we find that the system is globally stable for $Re \leq 2$ and the system holds unity MTEG for $Re < 2$.

Local MTEG analysis

For a given Re and local region α, we solve Eq. (4.23) for the MTEG bounds for both the W and B&T parameters. In FIG. 4.5, we compare MTEG bounds from the QC framework with Monte Carlo simulations and the MTEG obtained from the DAL method [KPW14, Ker18]. From FIGs. 4.5a and 4.5b, we see that MTEG bounds obtained from Eq. (4.23) (solid blue lines) are conservative. In FIG. 4.5, the solid gray curves correspond to the TEG from random initial conditions sampled with $\|\mathbf{x}_0\| = \frac{\alpha}{\sqrt{q}}$, and the red curves correspond to MTEG resulting from the nonlinear optimal

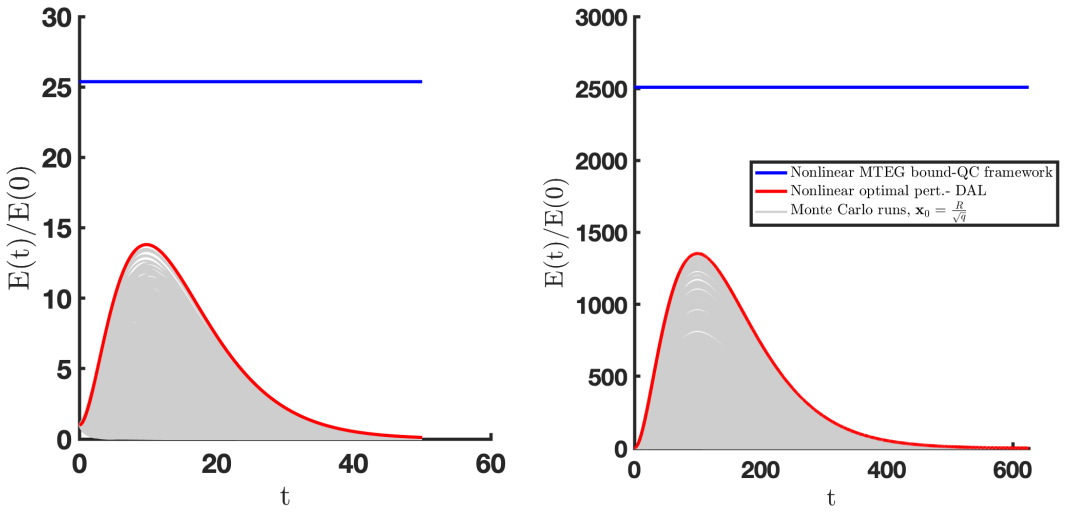

(a) W parameter, $Re = 100$ **(b)** B&T parameter, $Re = 100$

Figure 4.5: 5000 Monte Carlo simulations from various initial conditions such that $\|\mathbf{x}_0\|^2 \leq \frac{\alpha}{\sqrt{q}}$, with $\alpha = 10^{-2}$ and $\alpha = 10^{-4}$ for W parameter and B&T parameters respectively. The solid blue line shows the MTEG upper bound for nonlinear system predicted by the quadratic constraint framework proposed here. The solid gray curves show the Monte Carlo simulations for various initial conditions and the red curve shows the worst case MTEG of the nonlinear system.

perturbation obtained using DAL. For the W parameters and the B&T parameters, the MTEG bounds are reported for $\alpha = 10^{-2}$ and $\alpha = 10^{-4}$, respectively. The initial condition for the Monte Carlo simulations are obtained using the same α value and the corresponding q obtained from solving Eq. (4.23). Even though the QC framework provides a conservative estimate on the MTEG bounds, it can be an effective tool in analyzing transient energy growth in a more complex system where DAL and Monte Carlo based estimates are computationally cumbersome or in situations where exact information about the nonlinear terms may not be precisely known.

4.7 Lagrange Multiplier Analysis: Drawing Physical Insights Into Nonlinear Flow Interactions

In addition to providing a framework to analyze stability and transient energy growth, the quadratic-constraints-based methods can be used to gain insights into the physics

and dominating mechanisms underlying these dynamics. These insights are obtained by analyzing the Lagrange multipliers obtained from solving the GEVP in Eq. (4.21) as well as the SDP convex optimization problem in Eq. (4.23). The Lagrange multipliers provide information on the marginal cost of violating the associated constraints, thus indicating the relative importance of the corresponding constraints in the optimization problem. This allows for a quantitative analysis that can be used for identifying dominant nonlinear interactions. Here, we analyze the Lagrange multipliers for the W parameters since Waleffe discusses these nonlinear interaction terms in [Wal95b], providing a basis for comparison. However, the same conclusions are obtained from the Lagrange multiplier analysis of the B&T parameters as well.

The Lagrange multipliers obtained from solving Eq. (4.21) for R_0 with the W parameters over various Re are shown in FIG. 4.6. In FIG. 4.6a we observe that the importance of the nonlinear terms varies as Re is varied. In the initial phase for $Re < 175$, we see the dominating Lagrange multipliers are ξ_1 and ξ_2 corresponding to nonlinear interaction terms $-\gamma w^2 + v\bar{m}$ and δw^2, respectively. As Re increases, we see that the Lagrange multipliers ξ_2 (corresponding to δw^2) and ξ_3 (corresponding to $\gamma wu - \delta wv$) become more dominant with respect to the other multipliers. In FIG. 4.6a, it can be seen that ξ_2 is approximately 100 times more dominant than ξ_3 for $Re > 200$. Further, ξ_3 is orders of magnitude larger than the multipliers associated with the other nonlinearities. Over all Re, the most dominant Lagrange multiplier is ξ_2 (i.e., the nonlinear term δw^2), while the least dominating Lagrange multiplier is ξ_4 (i.e., nonlinear interaction $-vu$). Inspecting Lagrange multipliers alone may not provide the complete picture, as the Lagrange multipliers can be influenced by the scaling of the constraint matrix M_i. Hence, we also plot the singular values of $\xi_i M_i$—denoted by $\sigma_{max}(\xi_i M_i)$)—in FIG. 4.6b. The singular value analysis captures the overall contribution of each nonlinear interaction term, thereby also verifying these findings.

Similarly, in FIG. 4.7a, we show the Lagrange multipliers obtained from MTEG analysis (Eq. (4.23)) of the W parameters for $R = 0.01$. Again it can be observed that the nonlinear terms δw^2 and $\gamma wu - \delta wv$ — from ξ_2 and ξ_3, respectively —are the dominant flow interactions contributing to MTEG in the WKH system. We obtain similar findings related to dominating flow interactions when comparing Lagrange multipliers obtained from the R_0 analysis results from Eq. (4.21). Waleffe discusses the importance

of the nonlinearities δw^2 and $\gamma wu - \delta wv$ in feeding $\dot{v}$ and $\dot{w}$, thereby serving central roles in sustaining turbulence and conserving energy, respectively. We note that this analysis of Lagrange multipliers allowed the same dominant nonlinear flow physics to be identified without reliance upon any prior knowledge or physical insight. Similar trends are observed for other values of α. The same is true for the B&T parameters.

When we investigate the Lagrange multipliers for the MTEG bound from Eq. (4.23), we observe that the Lagrange multiplier ξ_3 (shown in FIG 4.7a) associated with the nonlinear term $\gamma wu - \delta wv$ consistently increases in magnitude with increasing Re, while Lagrange multipliers $\xi_0,\ \xi_1$ and ξ_4 always have magnitude ≤ 1. The multiplier ξ_3 has a magnitude of ≈ 110 at $Re = 150$ and it steadily increases by a factor of 6 at $Re = 280$. It should be noted that this increase in the magnitude of ξ_3—while other multipliers are relatively constant—shows the dominance of the associated nonlinear term. The same can be verified by studying the maximum singular values, $\sigma_{max}(\xi_i M_i)$ as shown in FIG. 4.7b.

To demonstrate the dominance of these nonlinear interactions, we perform MTEG analysis in Eq. (4.23) while retaining only the local constraints associated with the dominating nonlinear interactions ($\xi_2,\ \xi_3$) and neglecting the other local interactions ($\xi_1,\ \xi_4$). We choose $\alpha = 0.01$ as before, but now use only the lossless constraint along with constraints associated with ξ_2 and ξ_3 (see green line in FIG. 4.8) and compare results with the case where all the constraints are retained (see blue line in FIG. 4.8). The MTEG profile is based on analysis using two dominating nonlinear interactions ($\delta w^2,\ \gamma wu - \delta wv$), and the lossless constraint closely approximates the MTEG response of the whole nonlinear system. We observe similar qualitative trends for any other value of α for which the optimization problem is feasible and also for the B&T model parameters.

4.8 Conclusion

We presented a quadratic constraints framework to perform stability and transient energy growth analysis of nonlinear systems. The proposed framework facilitates stability and transient energy growth analysis in global and local settings around a given equilibrium point. The framework uses exact information from the linear dynamics, while nonlinear interactions are replaced by quadratic constraints that capture input-output

properties of the nonlinearity. The QC framework leverages the Lyapunov analysis, which provides guarantees on the estimates obtained and also enables circumventing the need for nonlinear simulations, which can be cumbersome for fluid systems.

We demonstrated the proposed analysis approach on the WKH model of transitional and turbulent flow. We first study the stability of the WKH model, for which the linear part is globally asymptotically stable for all Re. It is found that the nonlinear WKH system with W parameters is globally stable for $Re \leq 20$, consistent with previous results found in the literature. Similarly, the global stability of the WKH system for B&T parameters is verified for $Re \leq 2$. It is also observed that the energy-conserving nonlinear terms destabilize the system beyond the globally stable regime.

In order to assess stability and maximum transient energy growth performance beyond the globally stable regime, we introduced a new "local" analysis framework to analyze local stability and transient energy growth properties. The local analysis provides an inner approximation for the region of attraction (ROA), which is determined by solving a GEVP. In addition to the ROA analysis, the solution procedure can be used to estimate permissible perturbation amplitudes. These analysis methods were compared with more computationally intensive SOS and DAL methods.

We also introduced a method for estimating maximum transient energy growth bounds when the system is either globally stable or simply locally stable. The maximum transient energy growth (MTEG) bound was found to be unity below the critical Reynolds number for global stability. In the locally stable regime, we estimated the bounds on the MTEG and compared our results with those obtained from Monte Carlo simulations and DAL. Lastly, analyzing the Lagrange multipliers associated with each local constraint provided further insights into the physics. By comparing the relative magnitudes of the Lagrange multipliers, we were able to identify the dominating nonlinear interactions without any prior knowledge of the flow physics. The dominant nonlinear terms identified by this analysis agreed with the physical mechanisms originally described in [Wal95a].

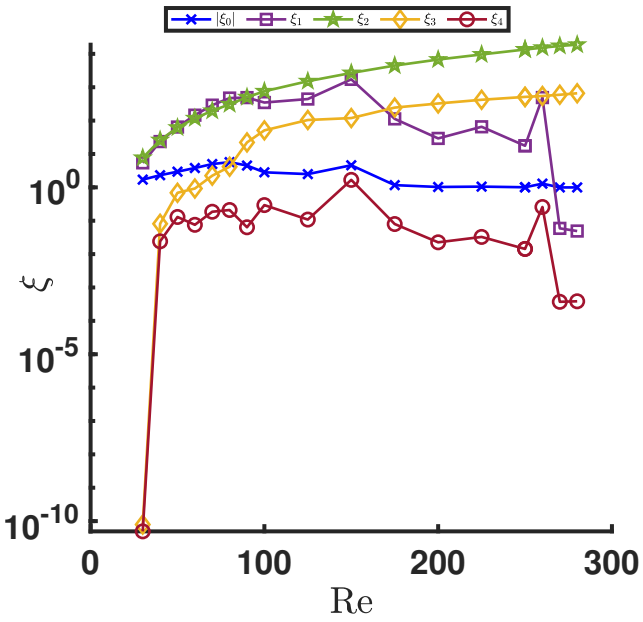

(a)

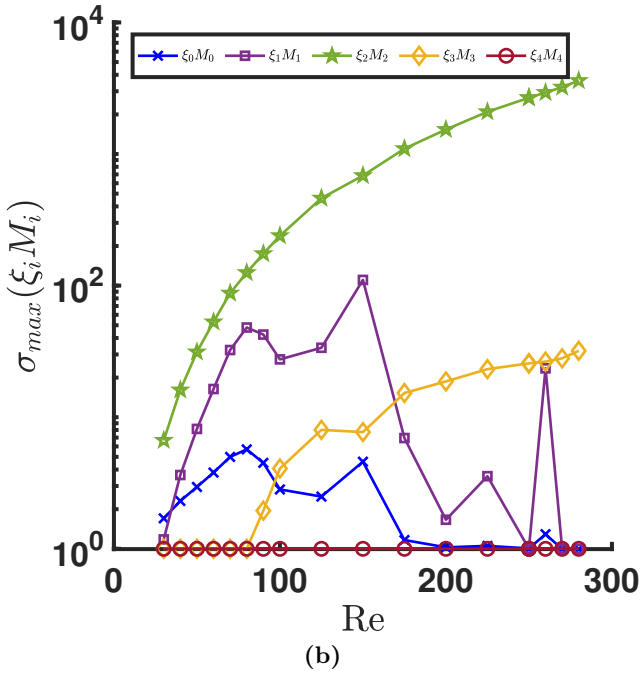

(b)

Figure 4.6: Results obtained from solving R_0 in Eq. (4.21) with W parameters. The dominating nonlinear terms for stability can be identified by analyzing Lagrange multipliers ξ_i in (a) and its associated singular values $\sigma_{max}(\xi_i M_i)$ in (b).

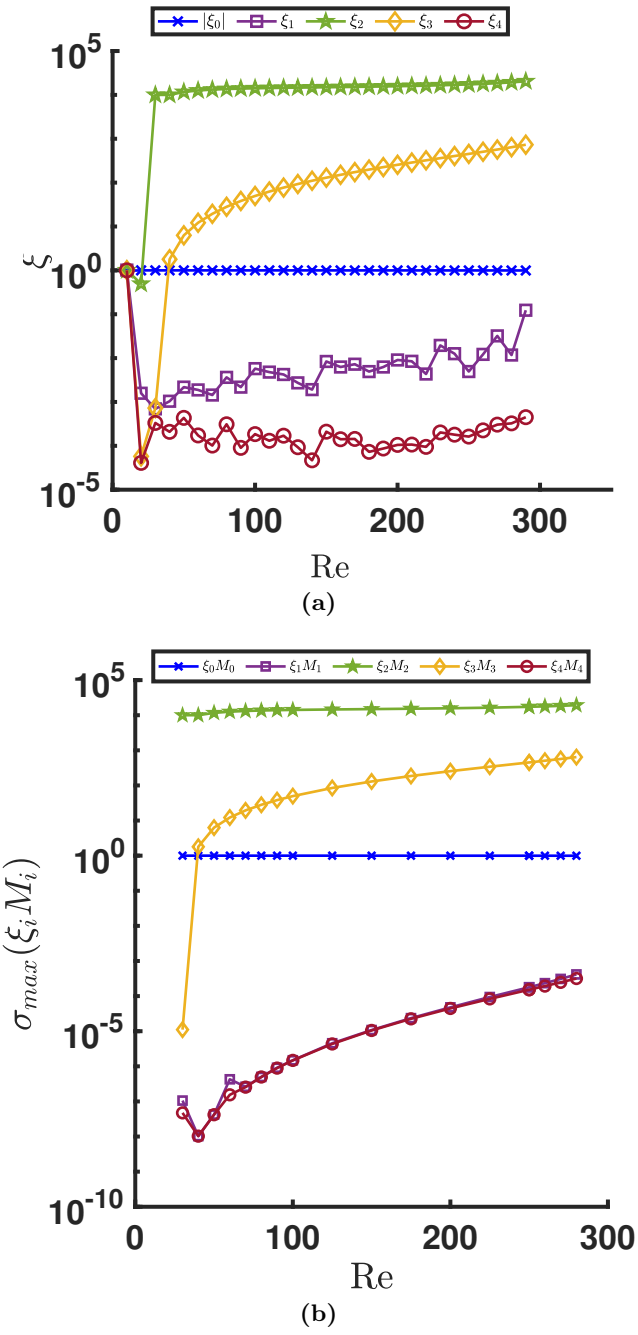

Figure 4.7: Results obtained from solving for q^* in Eq. (4.23). The dominant nonlinear terms for TEG can be identified by analyzing the dominant Lagrange multipliers ξ_i in (a) and its associated singular values $\sigma_{max}(\xi_i M_i)$ in (b).

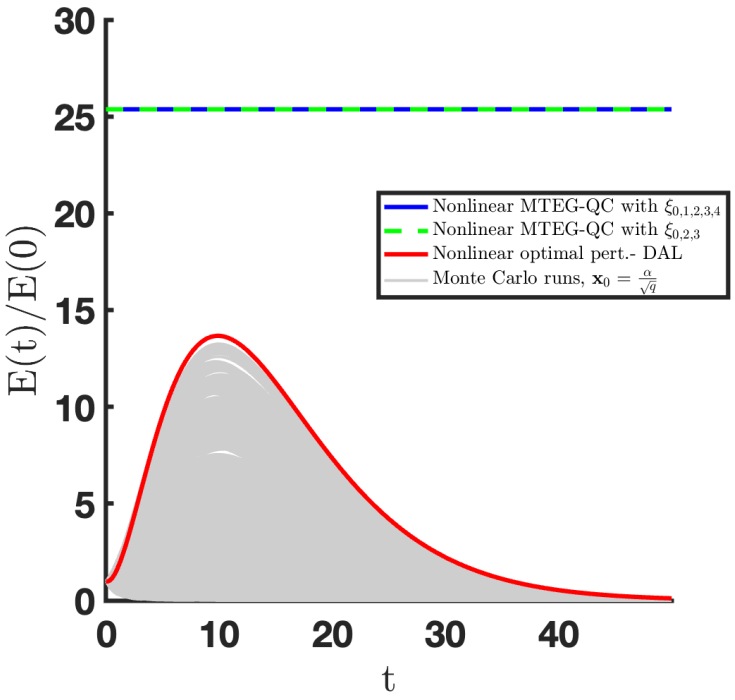

Figure 4.8: Local MTEG analysis for W parameters with global lossless constraint and the two most dominant local constraints compared against the MTEG of system with global and all local constraints for $Re = 100$ and $\alpha = 0.01$.

Chapter 5

Quadratic Constraints Generalized on Elliptical Sets

5.1 Introduction

The previous chapter has proposed exploiting quadratic constraints (QCs) between the inputs and outputs of the nonlinearity to conduct global and local stability analysis with reduced complexity. The trade-off for this computational expediency is a larger degree of conservatism in estimating the ROA and associated bounds on permissible perturbation amplitudes relative to more computationally demanding methods, such as SOS [GC12] and DAL [Ker18].

This chapter extends the QC formulation generalized to spherical sets, as proposed in the previous chapter, to ellipsoidal sets. The main idea behind this approach is as follows. The Lyapunov set defined as $V(\mathbf{x}) = \mathbf{x}^T P \mathbf{x}$ are ellipsoidal; however, in the previous chapter, we have been using spherical sets to obtain the outer and inner approximation of the Lyapunov sets—to obtain the ROA and largest permissible perturbations, respectively. The outer approximation previously used spherical sets of the form $\mathbf{x}^T \mathbf{x} \leq \alpha^2$. The fact that we are using a spherical set to obtain an outer approximation of the Lyapunov level set, which is ellipsoidal in shape, adds conservatism in our estimates. This is because the sphere has the same radius in all directions and will fit the ellipse poorly (fig. 5.1 illustrates this). Therefore, in this chapter, we introduce ellipsoidal sets of the form $\mathbf{x}^T E \mathbf{x} \leq \alpha^2$, which improve the accuracy by fitting the ellipsoidal

Lyapunov level set more tightly, thereby reducing conservatism.

In this chapter, it is shown that these new QCs formulated on ellipsoidal sets will reduce conservatism and improve estimates of both the ROA and the largest permissible perturbation. Formulating the problem for ellipsoidal sets leads to a bilinearity in the corresponding LMI; and special algorithms are necessary to solve the problem at hand. We propose two algorithms for performing this analysis: one is an iterative algorithm that solves a semi-definite program at each iteration to refine the ROA estimate, and the other is based on solving a single generalized eigenvalue problem (GEVP). Using the QCs generalized on ellipsoidal sets, we analyze ROA estimates and the largest permissible perturbation for system stability; the inner estimate of the ROA captures this perturbation. As an example, we will demonstrate our approach on two low-dimensional mechanistic transitional flow models: the 4-state Walleffe-Kim-Hamilton (WKH) model of shear flow [Wal95b] and the 9-state model of Couette flow [MFE04]. Finally, we measure the computational run-time and show that the proposed QC method obtains improved estimates over previous QC approaches as seen in previous chapter and in [LG20], while reducing computational time over SOS and DAL methods.

5.2 Elliptical Sets

The work in [LG20] improves upon the constraint proposed in the previous chapter in Eq. (4.19). However, the authors in [LG20] also generalize their constraints to spherical sets while obtaining improved results. In this work, we propose using ellipsoidal sets to obtain more refined estimates of the ROA and inner approximation of the ROA.

The next lemma generalizes the result in [LG20] by providing local constraints on an ellipsoidal set.

Lemma 2. *Let $E = E^T \succ 0$ be given and define the ellipsoid $\mathcal{E}_\alpha := \{\mathbf{x} \in \mathbb{R}^n : \mathbf{x}^T E \mathbf{x} \leq \alpha^2\}$. The nonlinearity N given in* (4.4b) *satisfies the following local QC for $i = 1, \ldots, n$:*

$$\begin{bmatrix} \mathbf{x} \\ \mathbf{z} \end{bmatrix}^T \begin{bmatrix} \alpha^2 (Q_i E^{-1} Q_i) & \underline{0} \\ \underline{0} & -\mathbf{e}_i \mathbf{e}_i^T \end{bmatrix} \begin{bmatrix} \mathbf{x} \\ \mathbf{z} \end{bmatrix} \geq 0, \ \forall \mathbf{x} \in \mathcal{E}_\alpha, \tag{5.1}$$

where $\mathbf{e}_i \in \mathbb{R}^n$ is the i^{th} standard basis vector.

Proof. Note that $\mathbf{z}^T\mathbf{e}_i\mathbf{e}_i^T\mathbf{z} = z_i^2$, where $z_i := \mathbf{x}^T Q_i \mathbf{x}$ is the i^{th} entry of $\mathbf{z} = N(\mathbf{x})$. Define $\mathbf{w} := E^{\frac{1}{2}}\mathbf{x}$ and $\hat{Q}_i := E^{-\frac{1}{2}} Q_i E^{-\frac{1}{2}}$ so that $z_i = \mathbf{w}^T \hat{Q}_i \mathbf{w}$. The Cauchy-Schwartz inequality yields the following bound:

$$z_i^2 \leq \|\mathbf{w}\|_2^2 \cdot \|\hat{Q}_i \mathbf{w}\|_2^2. \tag{5.2}$$

Note that $\|\hat{Q}_i\mathbf{w}\|_2^2 = \mathbf{x}^T Q_i E^{-1} Q_i \mathbf{x}$. Moreover, if $\mathbf{x} \in \mathcal{E}_\alpha$ then $\|\mathbf{w}\|_2^2 = \mathbf{x}^T E \mathbf{x} \leq \alpha^2$. Combining these facts with Eq. (5.2) yields $z_i^2 \leq \mathbf{x}^T[\alpha^2(Q_i E^{-1} Q_i)]\mathbf{x}$ for any $x \in \mathcal{E}_\alpha$. $\square$

This result corresponds to Lemma 1 in [LG20] for the special case $E = I$. This special case corresponds to a local constraint on a sphere of radius α. The generalization to local constraints on arbitrary ellipsoids, by adding a weight E such that $\mathbf{x}^T E \mathbf{x} \leq \alpha^2$, will be used to improve our estimates of the ROA.

5.3 LMI with Elliptical Constraints

We can combine Lyapunov theory with the local QCs from the previous section in order to compute an inner estimate $\hat{\mathcal{R}}$ for the ROA. Roughly, we will define a Lyapunov candidate $V(x) = \mathbf{x}^T P \mathbf{x}$ and use the QCs to show that $\dot{V}$ is negative definite along the trajectories of Eq. (4.3) in a neighborhood of the equilibrium point $\mathbf{x}_e = \mathbf{0}$. The inner estimate of the ROA will be given by a sphere of radius R, denoted $\hat{\mathcal{R}}_R := \{\mathbf{x} \in \mathbb{R}^n : \mathbf{x}^T\mathbf{x} \leq R^2\}$. The next theorem gives a matrix inequality condition to estimate the ROA using local QCs. This is based on a standard Lyapunov result (Theorem 4.1 in [Kha02]). To simplify notation, define the following matrices that appear in the QCs:

$$M_0 := \begin{bmatrix} \underline{0} & I \\ I & \underline{0} \end{bmatrix}, M_i(\alpha, E) := \begin{bmatrix} \alpha^2(Q_i E^{-1} Q_i) & \underline{0} \\ \underline{0} & -\mathbf{e}_i\mathbf{e}_i^T \end{bmatrix}. \tag{5.3}$$

Theorem 3. *Let $E = E^T \succ 0$, $\alpha > 0$, $\epsilon > 0$ be given. If $\exists P = P^T \in \mathbb{R}^{n\times n}$, $R > 0$, and*

$\xi_0, \ldots, \xi_n \in \mathbb{R}$ *such that:*

$$\begin{bmatrix} A^TP + PA & P \\ P & \underline{0} \end{bmatrix} + \xi_0 M_0 + \sum_{i=1}^{n} \xi_i M_i(\alpha, E) \preceq \begin{bmatrix} -\epsilon I & \underline{0} \\ \underline{0} & \underline{0} \end{bmatrix}, \tag{5.4}$$

$$\frac{1}{\alpha^2} E \preceq P \preceq \frac{1}{R^2} I, \tag{5.5}$$

$$\xi_i \geq 0, \ \textit{for } i = 1, \ldots, n \tag{5.6}$$

then $\hat{\mathcal{R}}_R \subset \mathcal{R}$.

Proof. Define the Lyapunov function $V(\mathbf{x}) := \mathbf{x}^T P \mathbf{x}$. Note that $\frac{1}{\alpha^2} E \preceq P$ implies $P \succ 0$. Multiply (5.4) on the left/right by $\begin{bmatrix} \mathbf{x}(t)^T & \mathbf{z}(t)^T \end{bmatrix}$ and its transpose to obtain:

$$\frac{d}{dt} V(\mathbf{x}(t)) + \xi_0 \begin{bmatrix} \mathbf{x}(t) \\ \mathbf{z}(t) \end{bmatrix}^T M_0 \begin{bmatrix} \mathbf{x}(t) \\ \mathbf{z}(t) \end{bmatrix}$$
$$+ \sum_{i=1}^{n} \xi_i \begin{bmatrix} \mathbf{x}(t) \\ \mathbf{z}(t) \end{bmatrix}^T M_i(\alpha, E) \begin{bmatrix} \mathbf{x}(t) \\ \mathbf{z}(t) \end{bmatrix} \leq -\epsilon \|\mathbf{x}(t)\|_2^2.$$

The second term with ξ_0 and M_0 is equal to zero due to the global lossless property of $N(\mathbf{x})$. Here, the scalar term ξ_0 can be either positive or negative. While the quadratic terms with ξ_i and $M_i(\alpha, E)$ ($i = 1$ to n) are each non-negative for any $\mathbf{x}(t) \in \mathcal{E}_\alpha$ by Lemma 2 and $\xi_i \geq 0$. Thus $\mathbf{x}(t) \in \mathcal{E}_\alpha$ implies $\frac{d}{dt} V(\mathbf{x}(t)) \leq -\epsilon \|\mathbf{x}(t)\|_2^2$.

The constraint $\frac{1}{\alpha^2} E \preceq P$ implies that if $V(\mathbf{x}) \leq 1$ then $\mathbf{x}^T E \mathbf{x} \leq \alpha^2$, i.e., $\{x \in \mathbb{R}^n : V(x) \leq 1\} \subset \mathcal{E}_\alpha$. Hence $\mathbf{x}_e = \mathbf{0}$ is locally asymptotically stable and the level set $\{\mathbf{x} \in \mathbb{R}^n : V(\mathbf{x}) \leq 1\}$ is contained in the ROA $\mathcal{R}$ (Theorem 4.1 in [Kha02]). Finally, the constraint $P \preceq \frac{1}{R^2} I$ implies that if $\mathbf{x}^T \mathbf{x} \leq R^2$, then $V(\mathbf{x}) \leq 1$. This yields the desired set containment:

$$\hat{\mathcal{R}}_R \subset \{\mathbf{x} \in \mathbb{R}^n : V(\mathbf{x}) \leq 1\} \subset \mathcal{R}.$$

□

This theorem provides an inner estimate of the ROA characterized by a sphere of radius R. A convex optimization can be used to compute the largest feasible R for

given values of (E, α, ϵ). Define $\lambda := \frac{1}{R^2}$ and note that maximizing R is equivalent to minimizing λ. Equations (5.4)-(5.6) are linear matrix inequalities (LMIs) in variables (P, ξ, λ). The following optimization is a semidefinite program (SDP):

$$\lambda^* := \min_{P,\xi,\lambda} \lambda \text{ subject to } (5.4) - (5.6). \tag{5.7}$$

An SDP is convex, and the global optimum λ^* can be computed efficiently using freely available solvers [BEFB94a, BV04]. The radius $R^* = \frac{1}{\sqrt{\lambda^*}}$ provides the largest spherical inner estimate of the ROA for the given local QC region (E, α) and $\epsilon > 0$. The parameter $\epsilon > 0$ is chosen to be a "small" positive number to ensure $\dot{V} < 0$. This term can be dropped if Eq. (5.4) is feasible with a strict inequality.

The main issue with this numerical method is that it requires the choice of the local QC region in terms of the ellipsoidal shape E and size α. If $E = I$, then the QCs are enforced on a sphere of radius α as shown in Figure 5.1. A small value of α will restrict the size of both the Lyapunov function level set and the spherical ROA inner estimate. On the other hand, a large value of α may cause the SDP to be infeasible. This occurs because the QC bounds on $N(x)$ become more conservative (less tight) for larger local regions. A one-dimensional line search can be used to compute the best value of α for a given local ellipsoid shape E. For example, the SDP in Eq. (5.7) can be solved with $E = I$ on a grid of values $\{\alpha_1, \ldots, \alpha_f\}$. Each solution yields an inner ROA estimate with radius $R^*(\alpha_i)$. The best α_i is the one that yields the largest inner ROA estimate: $\max_i R^*(\alpha_i)$.

The inner ROA estimate can be further improved by exploiting the ellipsoid shape as specified by E. Unfortunately Equations (5.4)-(5.6) are non-convex in (P, ξ, R, E, α). The first approach, denoted Algorithm A, iteratively updates the ellipsoid shape based on the Lyapunov function obtained from the previous iterate.

5.4 Algorithm A: Iterative-Refinement of R

The first step of Algorithm A is to provide an initial estimate for the SDP in Eq. (5.7), where the initial value of E is fixed to be I. Once the $E^{(1)} = I$ is fixed, we solve the SDP in Eq. (5.7) over a range of $[\alpha_1, \cdots, \alpha_f]$. Then the best $\alpha^{(1)}$ is found for $E = I$;

then their corresponding solution set $(P^{(1)},\ \xi^{(1)},\ R^{(1)})$ are saved.

For step 2 of Algorithm A, once the initial solution set $(P^{(1)},\ \xi^{(1)},\ R^{(1)})$ is obtained, the solutions are used to refine the guess for shape parameter E such that $E^{(2)} = P^{(1)}$. Following this we again solve the SDP in Eq. (5.7) with $E^{(2)}$ over a range of $[\alpha_1, \cdots, \alpha_f]$ and save the $(P^{(2)},\ \xi^{(2)},\ R^{(2)})$ corresponding to the largest $\alpha^{(2)}$. It is obvious, this is an iterative process and we keep repeating step 2 until we obtain a converged solution such that the solutions for R converges to a chosen threshold. This process is detailed as Algorithm A below.

Algorithm A: Iterative-Refinement for Estimating R
Initial Estimate: Define $M_i(\alpha, E)$ using $E^{(1)} = I$. Find the best $\alpha^{(1)}$ for the given local QCs $E^{(1)}$. Let $(P^{(1)}, \xi^{(1)}, R^{(1)})$ be the corresponding solutions of the SDP with $(E^{(1)}, \alpha^{(1)})$.
Refinement: Align the local QC set with the Lyapunov function solution: $E^{(2)} = P^{(1)}$. Find the best $\alpha^{(2)}$ for the updated local QCs $E^{(2)}$. Let $(P^{(2)}, \xi^{(2)}, R^{(2)})$ be the corresponding solutions of the SDP with $(E^{(2)}, \alpha^{(2)})$
Iterate: Repeat the refinement step with $E^{(i+1)} = P^{(i)}$ to yield $(\alpha^{(i)}, P^{(i)}, \xi^{(i)}, R^{(i)})$. This can be performed a fixed number of iterations or until the radius $R^{(i)}$ converges.

Note that the optimal solutions from the first step $(P^{(1)}, \xi^{(1)}, R^{(1)})$ are also feasible for the second step when $\alpha^{(2)} = 1$. The reason is that the constraint $\frac{1}{\alpha^2}E \leq P$ in Eq. (5.5) holds with equality when using $(P, E, \alpha) = (P^{(1)}, P^{(1)}, 1)$. Hence the inner estimate of ROA cannot shrink at the second step: $R^{(2)} \geq R^{(1)}$. Repeating this process gives a monotonically non-decreasing sequence of spherical inner estimates for the ROA: $R^{(i+1)} \geq R^{(i)}$. Note that each step of the iterative method has roughly the same computational cost as the first step. We have to solve one SDP for each value of α_i.

5.5 Algorithm B: One-Shot Approach for Estimating R

The second approach, denoted Algorithm B below, effectively performs only a single refinement of the local shape parameter E. This restriction allows the single refinement step to be formulated as a GEVP. This will typically reduce the computational cost,

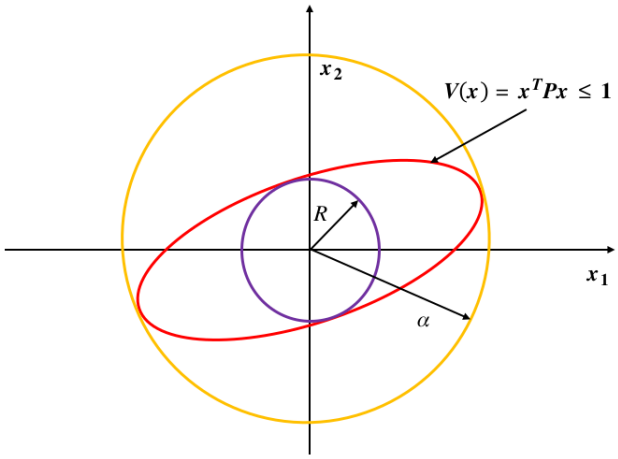

Figure 5.1: 2-D visualization of a spherical local region for the QCs corresponding to $E = I$ and $\alpha > 0$ (yellow), Lyapunov function level set $\{x \in \mathbb{R}^n : x^T P x \leq 1\}$ (red), and ROA inner estimate $\mathcal{R}_R$ (purple).

but possibly yield more conservative results (smaller estimates for $\hat{\mathcal{R}}_R$) as compared to Algorithm A. To formulate Algorithm B, first decompose the quadratic constraint matrix in Eq. (5.3) into two matrices as follows:

$$M_i(\alpha, E) = \alpha^2 \underbrace{\begin{bmatrix} Q_i E^{-1} Q_i & \underline{0} \\ \underline{0} & \underline{0} \end{bmatrix}}_{\tilde{M}_i} + \underbrace{\begin{bmatrix} \underline{0} & \underline{0} \\ \underline{0} & -\mathbf{e}_i \mathbf{e}_i^T \end{bmatrix}}_{\hat{M}_i}. \tag{5.8}$$

The first step is identical to step 1 of Algorithm A, as we solve the SDP in Eq. (5.7) with fixed $E = I$ over a grid of α and store the solutions from the SDP as $(P^{(1)}, \xi^{(1)}, R^{(1)})$.

The second step of Algorithm B fixes both the shape $E = P^{(1)}$ and Lyapunov function $P = P^{(1)}$. This aligns both the local QC ellipsoid shape E with the level sets of the Lyapunov function. The local regions for both are parameterized as $\{x \in \mathbb{R}^n : x^T P^{(1)} x \leq \alpha\}$. A sub-problem is to find the largest local region α over which the local quadratic constraints are valid and $\dot{V}(x(t)) < 0$. This is formulated by the following

optimization:

$$\begin{aligned} &\min_{\gamma,\xi_0,\ldots,\xi_n} \quad \gamma \\ &\text{subject to } \xi_i \geq 0 \qquad (\text{for } i = 1 \text{ to } n) \\ &\begin{bmatrix} A^TP + PA & P \\ P & \underline{0} \end{bmatrix} + \xi_0 M_0 + \sum_{i=1}^{n} \xi_i \hat{M}_i \prec \gamma \sum_{i=1}^{n} \xi_i \tilde{M}_i, \end{aligned} \tag{5.9}$$

where $\gamma = -\alpha^2$ and ξ_i ($i = 0$ to n) are Lagrange multipliers for the global and local constraints respectively. It is emphasized that $P = P^{(1)}$ is fixed and not a decision variable in the optimization. This is a GEVP [BG93] in variables α^2, $\xi_0, \ldots, \xi_n$. This one GEVP gives the largest level set α^* defined by $P = P^{(1)}$ over which the local quadratic constraints are valid and $\dot{V}(x(t)) < 0$. Let $\lambda_{max}(P^{(1)})$ denote the largest eigenvalue of $P^{(1)}$. For the obtaining the inner estimate R^*, note that the sphere $\hat{\mathcal{R}}_R$ is contained in $\{x \in \mathbb{R}^n : x^T P^{(1)} x \leq \alpha^{*2}\}$ if and only if $R \leq \frac{\alpha^*}{\sqrt{\lambda_{max}(P^{(1)})}}$. Therefore, in the third step, we can directly compute the largest radius of the inner ROA estimate $\hat{\mathcal{R}}_R$ from the optimal α^*. This is our second method to estimate the ROA and this second method is summarized below as Algorithm B.

Algorithm B: One-Shot Approach for Estimating R
Initial Estimate: Define $M_i(\alpha, E)$ using $E^{(1)} = I$. Find the best $\alpha^{(1)}$ for the given local QCs $E^{(1)}$. Let $(P^{(1)}, \xi^{(1)}, R^{(1)})$ be the corresponding solutions of the SDP with $(E^{(1)}, \alpha^{(1)})$. **Maximize Level Set:** Fix $P = E = P^{(1)}$ and solve the GEVP in Eq. (5.9) to obtain the maximal level set α^*. **Maximize ROA Inner Estimate:** Select $R^* = \frac{\alpha^*}{\sqrt{\lambda_{max}(P^{(1)})}}$.

5.6 Results

We evaluate the proposed analysis methods on two low-order mechanistic models of transitional flows that were used to demonstrate the QC analysis method in [LG20]:

the 4-state Waleffe-Kim-Hamilton (WKH) model [Wal95b] and the 9-state reduced-order model of a plane Couette flow [MFE04]. Both models have the form in Eq. (4.3), with non-normal linear dynamics and a quadratic lossless nonlinearity. We note that the linear dynamic matrix is parameterized by the Reynolds number Re: i.e., $A = A(Re)$. Additional details on the specific models used here can be found in [LG20].

5.6.1 9-State Model for Turbulent Shear Flows

To test the efficacy of the proposed method, we test the results on the 4-state WKH model and also a 9-state model obtained from Galerkin-Projections on the NSE. In this section, we briefly detail the 9-state model that has been used in this study.

The 9-state low dimensional model proposed by [MFE04] is based on Fourier modes and describes shears flows with no-slip boundary conditions that are forced using sinusoidal body forcing. The model uses non-dimensionalized NSE with sinusoidal body forcing that are projected onto a reduced sub-space using Galerkin projections resulting in a 9-state fluid flow model. The resulting 9 modes account for mean velocity profile and its modification, downstream vortices, streaks, instabilities of streaks and nonlinear interactions between the modes. It is shown the sub-critical transition is observed in this reduced-order model and the resulting model is of the form $\dot{\mathbf{x}} = A\mathbf{x} + \mathbf{z}$, as previously seen in Eq. (4.4a) and Eq. (4.4b). Here, the system state matrix is:

$$A = \frac{\Lambda}{Re} + W, \tag{5.10}$$

$$\Lambda = -diag(\beta^2, \frac{4\beta^2}{3} + \gamma^2, k^2_{\beta\gamma}, \frac{3\alpha^2 + 4\beta^2}{3}, k^2_{\alpha\beta}, \frac{3\alpha^2 + 4\beta^2 + 3\gamma^2}{3}, k^2_{\alpha\beta\gamma}, k^2_{\alpha\beta\gamma}, 9\beta^2) \tag{5.11}$$

$$W\mathbf{x} = N(\mathbf{x})\mathbf{c} + N(\mathbf{c})\mathbf{x}. \tag{5.12}$$

Here, $\alpha = \frac{2\pi}{L_x}$, $\beta = \frac{\pi}{2}$, $\gamma = \frac{2\pi}{Lz}$ are the wavenumbers in the streamwise, wall-normal and spanwise directions with $L_x = 1.85\pi$ and $L_z = 1.25\pi$. The length of the domain are chosen such that sustained turbulence is observed from numerical simulations [MFE04]. The constants $k_{\alpha\beta} = \sqrt{\alpha^2 + \beta^2}$, $k_{\alpha\beta\gamma} = \sqrt{\alpha^2 + \beta^2 + \gamma^2}$, $k_{\beta\gamma} = \sqrt{\beta^2 + \gamma^2}$. The vector $\mathbf{c}$ in W is the laminar states fixed point and corresponds to

$\mathbf{c} = \begin{bmatrix} 1 & 0 & 0 & 0 & 0 & 0 & 0 & 0 & 0 \end{bmatrix}^T$. The quadratic nonlinear terms $\mathbf{z} = N(\mathbf{x}) = Q(\mathbf{x})\mathbf{x}$ are given as follows:

$$[Q(\mathbf{x})\mathbf{x}]_1 = \sqrt{\frac{3}{2}}\frac{\beta\gamma}{k_{\beta\gamma}}x_2x_3 - \sqrt{\frac{3}{2}}\frac{\beta\gamma}{k_{\alpha\beta\gamma}}x_6x_8 \tag{5.13}$$

$$[Q(\mathbf{x})\mathbf{x}]_2 = \frac{10}{3\sqrt{6}}\frac{\gamma^2}{k_{\alpha\gamma}}x_4x_6 - \frac{\gamma^2}{\sqrt{6}k_{\alpha\gamma}}x_5x_7 - \frac{\alpha\beta\gamma}{\sqrt{6}k_{\alpha\beta}k_{\alpha\beta\gamma}}x_5x_8 - \sqrt{\frac{3}{2}}\frac{\beta\gamma}{k_{\beta\gamma}}(x_1x_3 + x_3x_9) \tag{5.14}$$

$$[Q(\mathbf{x})\mathbf{x}]_3 = \sqrt{\frac{2}{3}}\frac{\alpha\beta\gamma}{k_{\alpha\gamma}k_{\beta\gamma}}(x_5x_6 + x_4x_7) + \frac{\beta^2(3\alpha^2+\gamma^2) - 3\gamma^2k_{\alpha\gamma}^2}{\sqrt{6}k_{\alpha\gamma}k_{\beta\gamma}k_{\alpha\beta\gamma}}(x_4x_8) \tag{5.15}$$

$$[Q(\mathbf{x})\mathbf{x}]_4 = -\frac{\alpha}{\sqrt{6}}(x_1x_5 + x_5x_9) - \frac{10}{3\sqrt{6}}\frac{\alpha^2}{k_{\alpha\gamma}}x_2x_6 - \sqrt{\frac{3}{2}}\frac{\alpha\beta\gamma}{k_{\alpha\gamma}k_{\beta\gamma}}x_3x_7 - \sqrt{\frac{3}{2}}\frac{\alpha^2\beta^2}{k_{\alpha\gamma}k_{\beta\gamma}k_{\alpha\beta\gamma}}x_3x_8 \tag{5.16}$$

$$[Q(\mathbf{x})\mathbf{x}]_5 = \frac{\alpha}{\sqrt{6}}(x_1x_4 + x_4x_9) + \sqrt{\frac{2}{3}}\frac{\alpha\beta\gamma}{k_{\alpha\gamma}k_{\beta\gamma}}x_3x_6 + \frac{\alpha^2}{\sqrt{6}k_{\alpha\gamma}}x_2x_7 - \frac{\alpha\beta\gamma}{\sqrt{6}k_{\alpha\gamma}k_{\alpha\beta\gamma}}x_2x_8 \tag{5.17}$$

$$[Q(\mathbf{x})\mathbf{x}]_6 = \frac{10}{3\sqrt{6}}\frac{\alpha^2-\gamma^2}{k_{\alpha\gamma}}x_2x_4 - \sqrt{\frac{2}{3}}\frac{2\alpha\beta\gamma}{k_{\alpha\gamma}k_{\beta\gamma}}x_3x_5 + \frac{\alpha}{\sqrt{6}}(x_1x_7 + x_7x_9) + \sqrt{\frac{3}{2}}\frac{\beta\gamma}{k_{\alpha\beta\gamma}}(x_1x_8 + x_8x_9) \tag{5.18}$$

$$[Q(\mathbf{x})\mathbf{x}]_7 = \frac{\alpha\beta\gamma}{\sqrt{6}k_{\alpha\gamma}k_{\beta\gamma}}x_3x_4 + \frac{-\alpha^2+\gamma^2}{\sqrt{6}k_{\alpha\gamma}}x_2x_5 - \frac{\alpha}{\sqrt{6}}(x_1x_6 + x_6x_9) \tag{5.19}$$

$$[Q(\mathbf{x})\mathbf{x}]_8 = \frac{\gamma^2(3\alpha^2-\beta^2+3\gamma^2)}{\sqrt{6}k_{\alpha\gamma}k_{\beta\gamma}k_{\alpha\beta\gamma}}x_3x_4 + \sqrt{\frac{2}{3}}\frac{\alpha\beta\gamma}{k_{\alpha\gamma}k_{\alpha\beta\gamma}}x_2x_5 \tag{5.20}$$

$$[Q(\mathbf{x})\mathbf{x}]_9 = \sqrt{\frac{3}{2}}\frac{\beta\gamma}{k_{\beta\gamma}}x_2x_3 - \sqrt{\frac{3}{2}}\frac{\beta\gamma}{k_{\alpha\beta\gamma}}x_6x_8 \tag{5.21}$$

This gives us the complete system of equations necessary. Further modeling details can be found in [MFE04].

5.6.2 Region of Attraction

We begin by using the GEVP in Eq. (5.9) to estimate the size α^* of the ROA over a range of Re. This is done by applying steps 1 and 2 of Algorithm B. Figures 5.2a and

5.2b show the results of this analysis (light blue) for the WKH and 9-state Couette flow models, respectively. These results are compared against ROA estimates based on the quadratic constraints proposed in Liu and Gayme [LG20] (green), and those proposed in the previous chapter (also published in [KSH21]) are referred to as Kalur, Seiler, and Hemati (red). This comparison indicates that the ROA estimate based on refinement of the local QC region in steps 1 and 2 of Algorithm B leads to less conservative estimates on α^*. Of note here is that although the Liu & Gayme analysis reduces the conservatism in the analysis relative to the Kalur, Seiler, & Hemati analysis (proposed in previous chapter), the formulation based on ellipsoidal sets reduces conservatism relative to both of these methods by a substantially larger degree for both mechanistic models.

5.6.3 Largest Permissible Perturbation

Next, we apply Algorithm A and Algorithm B to estimate the inner approximation R^* as a function of Re. This analysis is equivalent to computing a bound on the permissible perturbation amplitude or sphere of "safe" initial conditions. In Figure 5.3, the radius of the largest $\hat{\mathcal{R}}_R$ is denoted as R^* and is obtained from solving Algorithm A and compared with SOS and DAL estimates for the WKH and 9-state Couette flow models, respectively. The DAL method solves a variational problem for the nonlinear optimal perturbation used as a benchmark for comparison. The SOS analysis uses the toolbox available in [BPST]. To solve Eq. (5.7) for the WKH model and 9-state models, we use 200 logarithmically spaced values of α between 10^{-5} and 10^{1}. We compute the ROA estimate using the largest radius obtained on this grid, i.e., $R^* := \max_i R(\alpha_i^*)$. The results in Figure 5.3 show that the ellipsoidal sets improve the estimates of $\hat{\mathcal{R}}_R$ compared to the spherical sets given in [KSH21, LG20]. This is true even at the initial iterate, which yields improvements of approximately 4 times and 2.5 times for the WKH and 9-state models, respectively. Additional refinement iterations improve the results even further; however, we set the tolerance for convergence to 10^{-4}, and also observe only a marginal improvement after three iterations of Algorithm A (gray curve). For the 9-state model, there is an improvement factor of roughly 2.4 and 3.3 using Algorithm A (blue curve) over the QC methods of Liu & Gayme and Kalur, Seiler & Hemati. Additionally, the improvement factor of R^* is ≈ 3.38 using Algorithm A as compared to the other two QC constraints for the WKH model.

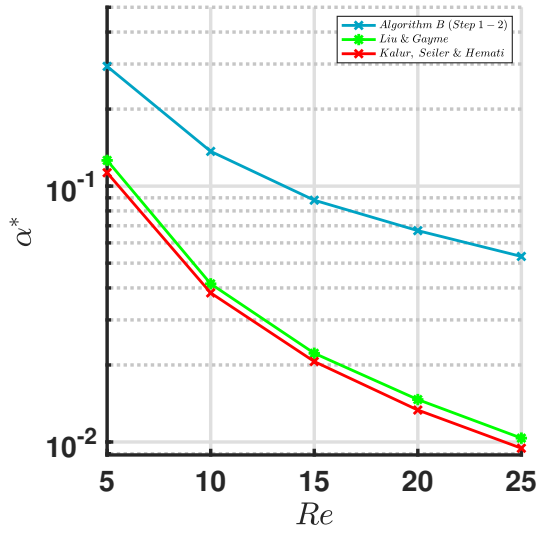

(a) WKH Model

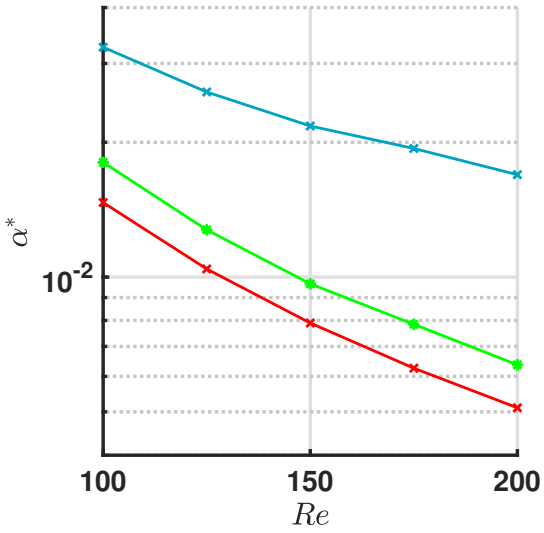

(b) 9-state Couette Flow Model

Figure 5.2: The ellipsoidal constraints using step 1 and 2 of Algorithm B shows significant improvement in region of attraction (ROA) estimates.

In Figure 5.3, we also compare the results obtained using Algorithm A with SOS and DAL methods. We find that each iteration of Algorithm A reduces the conservatism of the QC estimates, but the inner estimate is still conservative relative to the SOS and DAL methods. More specifically, the largest radius R^* obtained from the SOS (black

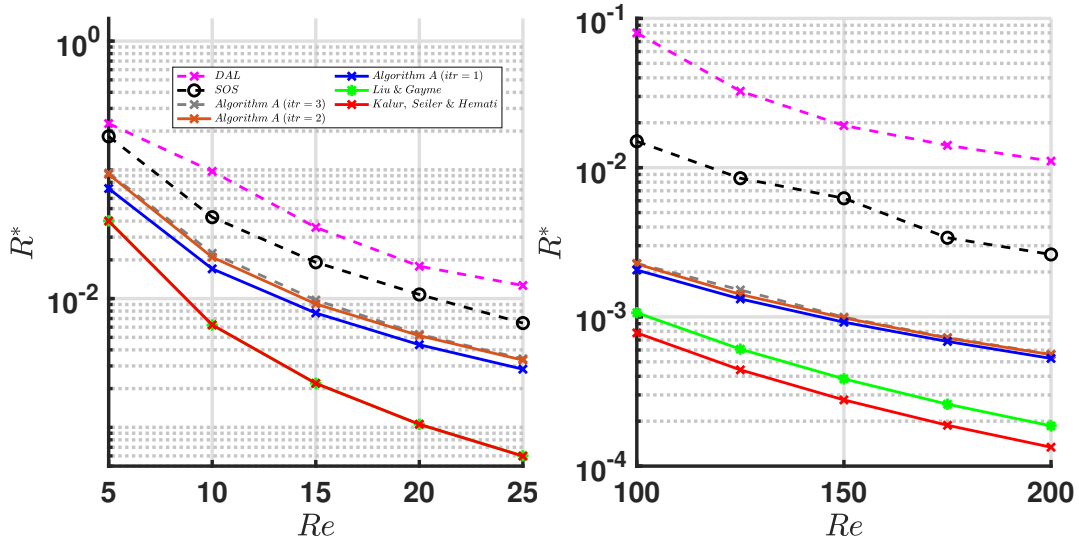

(a) WKH Model **(b)** 9-state Couette Flow Model

Figure 5.3: The inner estimates of ROA obtained using Algorithm A show improved estimates compared to methods based on spherical sets.

dashed curve) method and Algorithm A with 1 iteration (blue curve) differ by an average factor of ≈ 2.45 and ≈ 6.1 for the WKH and 9-state models, respectively. The differences in the R^* estimates become even greater for the DAL approach, with the DAL estimates (magenta curve) being larger by a factor of ≈ 3.5 and ≈ 23 than the Algorithm A estimates for the WKH and 9-state models, respectively. We note that SOS and DAL methods provide superior estimates of R^* because both of these methods use precise information of the nonlinearity and exact equations of motion. This contrasts with the QC-based approaches, whereby only input-output properties of the nonlinear terms are used.

Next, we assess estimates of R^* using Algorithm B (see Figure 5.4). The second step in Algorithm B avoids the computationally demanding step of solving over a grid of α, as is required in Algorithm A. Instead, Algorithm B directly determines the best α for the given shape E and Lyapunov energy matrix P and thus provides an efficient "one-shot" approach to estimate R^*. Since Algorithm B does not facilitate further iterations, in general, it provides conservative results compared to Algorithm A. However,

Table 5.1: Total run-time for calculating R^* by the various methods studied.

Method	Run-time to convergence (secs)	
	WKH	9-state
Algorithm A (solver: Mincx Matlab)	2.89	63.48
Algorithm B (solver Mincx & gevp Matlab)	1.85	37.99
DAL	9.82	137.6
SOS	116.8	5.82×10^4

Algorithm B substantially reduces conservatism to prior formulations of the QC analysis presented in [KSH21, LG20]. Figure 5.4 shows that estimates from Algorithm A and 2 differ by a factor of roughly 1.16–on average–for the 9-state Couette flow model. Although not reported here, we made similar observations in our analysis of the WKH model, where the difference was roughly a factor of 1.06 between Algorithm A and 2 estimates of R^*.

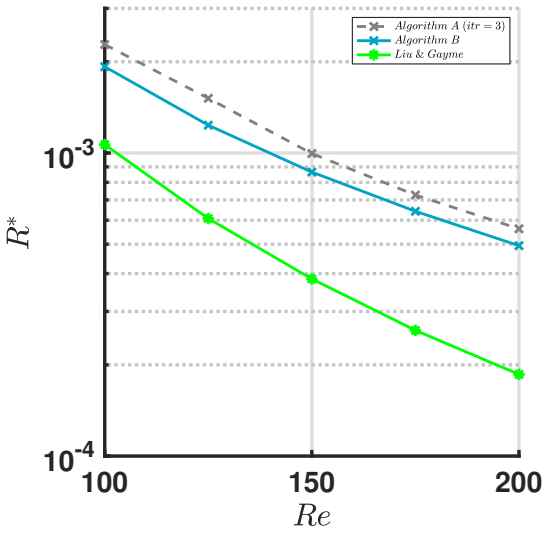

Figure 5.4: The inner estimate of ROA obtained using Algorithm B for the 9-state model is conservative compared to the refinement using Algorithm A.

Finally, we assess the computational run-time performance of the various methods investigated in this study. All computations were performed on an ASUS ROG M15 laptop with Intel 2.6 GHz i7-10750H CPU and 16 GB RAM. Overall, both Algorithm A and B proposed in this work require less total run-time than DAL and SOS methods. This savings becomes especially apparent in analyzing the 9-state model. Although the

Table 5.2: Average solver time per iteration for calculating R^* by the various methods studied.

Method	Run-time to convergence (secs)	
	WKH	9-state
Algorithm A (solver: Mincx Matlab)	0.76×10^{-2}	0.15
Algorithm B (solver Mincx & gevp Matlab)	2.3×10^{-2}	0.49
DAL	8.64×10^{-4}	0.18×10^{-2}
SOS	2.9	1.45×10^{3}

SOS and DAL methods yield more accurate estimates, these methods scale poorly with the state dimension compared to the QC analysis methods. The SOS method for WKH has a wall-time of about 116.8 seconds compared to 5.82×10^4 seconds for the 9-state model (as seen in table 5.1). Similarly, the solver run times for each iteration of the WKH model is 2.9 seconds compared to 1.45×10^3 seconds for the 9-state model (see table 5.2). Thus, in the case of the SOS method, roughly doubling the states results in the total computation time increasing by a factor of ≈ 500. In contrast, the total run-time of the QC-based Algorithm A increased by a factor of roughly 20 between the 4-state WKH model and the 9-state model, as seen in table 5.1. For the 9-state model, when we compare the run-time for Algorithm A to the SOS method, we see that the QC method is approx 900 times faster. We note that the run-time for the DAL method appears to increase by a factor of roughly 15 when going from the 4-state WKH model to the 9-state model, which actually seems to scale better than even the QC method; however, it is important to note that the DAL method can be sensitive to the final simulation time, perturbation size, tolerances, etc. Thus, tuning the DAL method can be a time intensive process, especially when system parameters (e.g., Re) are changed. The time required to tune the DAL process to obtain the precise estimates reported in this study is not reflected in the times listed in Table 5.1. Overall, we conclude that the QC-based Algorithms A and B require less end-to-end time than SOS and DAL methods and yield R^* solutions that are approximately within one order of magnitude of the SOS and DAL estimates. From table 5.2, we can see that the average solver time per iteration for Algorithm A & B is almost half of both the SOS and DAL method when tested on both the WKH and 9-state model.

5.7 Conclusion

This chapter proposes an improvement to the quadratic constraint (QC) framework for nonlinear fluid flow analysis. This was done by generalizing the local QCs from spherical sets (proposed in [KSH21, KSH20, LG20]) to ellipsoidal sets, which reduced conservatism and improved estimates of the ROA. Additionally, two algorithms are proposed and investigated for performing the ROA analysis. The less conservative but more computationally demanding algorithm—Algorithm A—iteratively refines the solution by solving a sequence of semi-definite programs. In contrast, the more computationally efficient algorithm—Algorithm B—solves a single generalized eigenvalue problem (GEVP) and yields estimates of the ROA and permissible perturbation amplitude in a single pass. Both Algorithms 1 and 2 were found to outperform the QC analysis methods proposed in [KSH21] and [LG20] in terms of accuracy. Algorithm B did so at no additional computational cost over these prior QC-based analysis methods. Both of the proposed algorithms surpassed prevailing SOS and DAL methods in terms of computational run-time.

Chapter 6

Quadratic constraints based stability analysis of Burgers equations

6.1 Introduction

The previous two chapters introduce the QC formulation to generalized to spherical and elliptical sets, respectively. This chapter establishes a proof of concept by applying the quadratic constraints framework to nonlinear PDEs like the viscous Burgers Equations. We choose the viscous Burgers PDE as our system of choice as it closely models turbulence exhibited in the NSE. The viscous Burgers PDE is related to the NSE in terms of having similar characteristics. The nonlinear terms in both equations arise from convective acceleration, and the transition phenomena are observed in both the Burgers PDE and NSE. Albeit, the 1D viscous Burgers equation is a much simpler system to analyze compared to the NSE. Apart from modeling fluid flows, the Burgers PDE is also used to model traffic flow. Since the viscous Burgers PDE is representative of many nonlinear PDEs and has multiple applications, the proposed QC framework is applied to study the stability of the viscous Burgers equations.

The viscous Burgers PDE is first converted to a set of ODEs using finite difference approximation techniques such as the central difference approximation. It is observed

that the resulting set of ODEs, after the application of central difference, are still large dimensional systems. This large dimension makes the application of the QC framework intractable. Therefore, the set of ODEs are reduced in dimension by using proper orthogonal decomposition (POD); we can now use this POD-based ROM with the QC framework to analyze systems stability.

In summary, in this chapter, we combine part I (reduced-order models) and Part II (reduced-complexity modelling) of the thesis to analyze the stability of a nonlinear PDE. More specifically, we use reduced-order modeling techniques of POD-based model reduction on the viscous Burgers equations and then apply the proposed reduced-complexity modeling framework to perform local stability analysis, which entails finding the largest ROA and largest permissible perturbations.

6.2 Burgers Equation

The viscous Burgers equation is a one-dimensional nonlinear advection-diffusion partial differential equation occurring in various areas of applied mathematics. Due to the advective nonlinear term, which is quadratic, we also observe the phenomena of shocks and their dissipation due to the diffusive terms. The Burgers equations' ability to have discontinuities (shocks) and transition makes it an appealing yet simpler prototype of the Navier-Stokes equations. The Burgers equation is given as

$$\frac{\partial \mathbf{u}}{\partial t} = \nu \frac{\partial^2 \mathbf{u}}{\partial \mathbf{x}^2} + \mathbf{u} \frac{\partial \mathbf{u}}{\partial \mathbf{x}}. \tag{6.1}$$

Where, $\mathbf{u}(t, \mathbf{x})$ is the velocity of the traveling wave, ν is the diffusion term, $\mathbf{x}$ is the spatial domain, and t is the time. The quadratic term in Eq. (6.1) arises from convective acceleration, as also seen in the NSE.

Since Eq. (6.1) is a partial differential equation, it has to be discretized in space and time to obtain solutions. We use finite difference approximation, specifically the central difference scheme, to obtain solutions. As we will see in the next section, central difference approximation results in a set of ordinary differential equations (ODEs), which are then solved using standard numerical integrators like *ode45* in Matlab.

6.2.1 Finite difference approximation

Finite difference approximation is used for approximating derivatives for numerical solutions of partial differential equations. Let $f(x)$ be a smooth function evaluated at x, and h be a constant spacing between the neighbouring point and x itself, then central difference is given by $\delta_h[f](x) = f(x + \frac{1}{2}h) + f(x - \frac{1}{2}h)$. It can also be seen from the Taylor series analysis that the truncation error for central difference is of $O(h^2)$. Here, we solve Eq. (6.1) using central finite difference. Application of central difference for each terms in Eq. (6.1) results in the following stencil

$$\frac{\partial u_i}{\partial x} = \frac{(u_{i+1} - 2u_i + u_{i-1})}{\Delta x^2} \tag{6.2}$$

$$\frac{\partial^2 u_i}{\partial x^2} = \frac{(u_{i+1} - 2u_i + u_{i-1})}{\Delta x^2}. \tag{6.3}$$

Here, $i = 0, \cdots, N+1$ is the index of the i^{th} point on the domain, Δx is the constant spacing between two neighbouring points $\mathbf{x}_i$ and $\mathbf{x}_{i+1}$ in the domain. Plugging Eqs. (6.2) and (6.3) into Eq. (6.1), we get a set of ordinary differential equation of the form:

$$\frac{\partial \mathbf{u}_i}{\partial t} = \frac{\nu}{\Delta x^2}(\mathbf{u}_{i+1} - 2\mathbf{u}_i + \mathbf{u}_{i-1}) - \frac{\mathbf{u}_i}{2\Delta x}(\mathbf{u}_{i+1} - \mathbf{u}_{i-1}), \text{ for } i = 0, \cdots, N+1. \tag{6.4}$$

It should be noted that Eq. (6.4) can be written in the form of $\dot{\mathbf{x}} = A\mathbf{x} + \mathbf{z}$ (as shown in Eq. (4.4a)), where $\mathbf{z}$ is the quadratic nonlinearity (as shown previously in Eq. (4.4b)). The quadratic nonlinear terms for the i^{th} point are given by $\mathbf{z}_i$, which can be decomposed into its quadratic form

$$\mathbf{z}_i = \frac{\mathbf{u}_i}{2\Delta \mathbf{x}}(\mathbf{u}_{i+1} - \mathbf{u}_{i-1}) = \frac{1}{2\Delta x}\begin{bmatrix} u_{i-1} & u_i & u_{i+1} \end{bmatrix} \underbrace{\begin{bmatrix} 0 & 1/2 & 0 \\ 1/2 & 0 & -1/2 \\ 0 & -1/2 & 0 \end{bmatrix}}_{Q} \begin{bmatrix} u_{i-1} \\ u_i \\ u_{i+1} \end{bmatrix}. \tag{6.5}$$

It should be noted that the quadratic nonlinear terms for the i^{th} point depend of the $i,\ i-1,\ i+1$ points. In this case, the boundary conditions are set to 0 i.e., $\mathbf{u}_0 = \mathbf{u}_{N+1} = 0$. Hence, we remove the points corresponding to the boundary points from the state such that the resulting state is given as $\mathbf{x} = \begin{bmatrix}\mathbf{u}_1 & \cdots & \mathbf{u}_N\end{bmatrix}^T$. The quadratic term can now be represented in the quadratic form using the states $\mathbf{x}$ and weighting matrix Q, as follows

$$\mathbf{z} = \begin{bmatrix} z_1 \\ \vdots \\ z_N \end{bmatrix} = \begin{bmatrix} \mathbf{x}^T Q_1 \mathbf{x} \\ \vdots \\ \mathbf{x}^T Q_N \mathbf{x} \end{bmatrix}. \tag{6.6}$$

Since the PDE is now converted to an ODE, we know all the necessary information to propagate the resulting system in time. We simulate the Burgers equation on a spatial grid of $N = 129$ points and use a sinusoidal initial condition. The length of the spatial domain is 1 with $\Delta x = \frac{1}{N-1}$. The resulting advecting and diffusing waves at different time instances is shown in fig. 6.1

We observe that resolving $N = 129$ gives a good approximation of the traveling wave; however, resolving the grid more coarsely leads to errors. The dimension $N = 129$ is still very large for using the quadratic constraints framework. Hence, we will have to use reduced-order modeling to obtain a lower-dimensional representation of the Burgers equation to apply the QC framework. This will be the topic of discussion in the next section.

6.3 Reduced-order models using POD

This section uses proper orthogonal decomposition-based reduced-order modeling to obtain a lower-dimensional representation of the Burgers system. As discussed in section. 3.5, the POD basis is optimal for capturing the energy. A Galerkin projection onto these modes has shown to be effective for reduced-order modeling of the Burgers equations [AM15]. To obtain the POD modes, we use the following procedure:

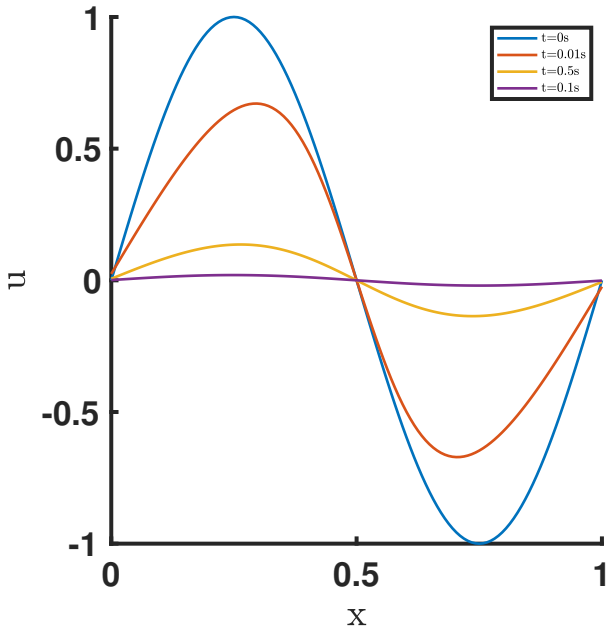

Figure 6.1: Burgers equation simulated with $\nu = 0.1$ and sinusoidal initial conditions. The advecting and diffusing waves are shown at four different time instances of $t = 0s,\ 0.01s,\ 0.05s, 0.1s$, respectively.

1. Create snapshot matrix X by collecting state trajectories from time $t = 0,\ \cdots,\ K$

$$X = \begin{bmatrix} \mathbf{x}(t_0) & \mathbf{x}(t_1) & \cdots & \mathbf{x}(t_K) \end{bmatrix}. \tag{6.7}$$

2. Perform singular value decomposition of snapshot matrix X such that $[U, \Sigma, V] = \text{svd}(X)$.

3. The POD modes Φ is given by the first r columns of the matrix U.

Here, $\Phi \in \mathbb{R}^{N \times r}$ are the POD modes. Next, the transformation $\Phi \mathbf{x}_r = \mathbf{x}$ is used to obtain the new reduced-order state $\mathbf{x}_r \in \mathbb{R}^r$. The dynamics of the system in the POD basis is given as

$$\dot{\mathbf{x}}_r = A_r \mathbf{x}_r + \underbrace{\begin{bmatrix} \mathbf{x}_r^T \tilde{Q}_1 \mathbf{x}_r \\ \vdots \\ \mathbf{x}_r^T \tilde{Q}_r \mathbf{x}_r \end{bmatrix}}_{\mathbf{z}_r} \tag{6.8}$$

Here, the matrix $A_r = \Phi^T A \Phi$ and the matrix $\tilde{Q}_j = \sum_{i=1}^{N} \phi_{ij} \Phi^T Q_i \Phi$, for $j = 1, ..., r$. The resulting system has dimension $r = 5$, the value of r is chosen by inspecting the singular values and retaining 99% of the system energy. Once the ROM is obtained, we can propagate the system in time and then "lift" the system's trajectories back to the original basis using inverse projections. From fig. 6.2, we can see that the ROM of size $r = 5$ approximates the FOM of size $N = 129$ accurately, such that the errors between in the ROM and FOM are in order of 10^{-13}.

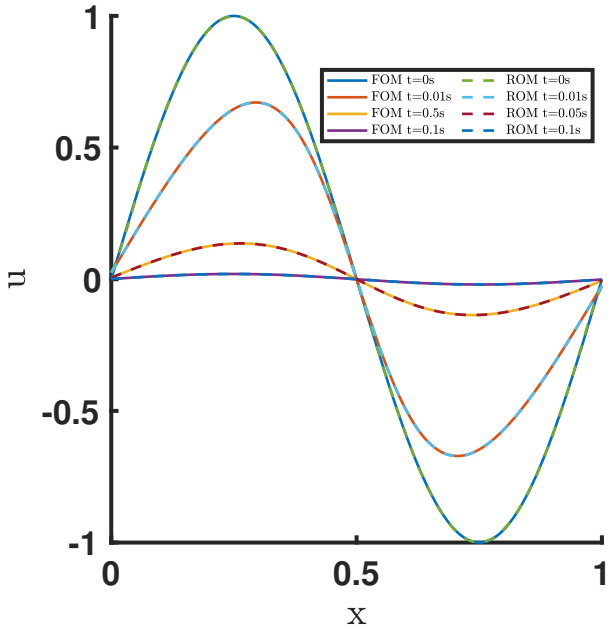

Figure 6.2: The full-order model (FOM) in solid lines of the Burgers equation and a reduced-order model (ROM) with $r = 5$ in dashed lines are shown at 4 different instances. There is a good agreement between the FOM and ROM, as seen in the figure.

6.4 Results

After successfully reducing the system's dimensionality, we can now apply the QC framework introduced in chapters 4 and 5 to study the stability of the reduced-order Burgers system. For Eq. (6.1), $Re = \frac{1}{\nu}$, therefore the parameter Re of the Burgers system is varied to study how the systems stability is changing based on variations in Re.

In this section, we study the stability of the Burgers equation by analyzing the largest permissible perturbations. The largest permissible perturbations are studied using the proposed spherical and ellipsoidal sets. Note that the Burgers equation does not have a lossless nonlinearity, as seen in the previous systems' analyzed in this thesis. Hence, only a local stability analysis of the reduced-order Burgers equations is performed. First, analysis is performed on how the size of the largest permissible perturbation changes with variation to Re. Finally, we also compare the largest permissible perturbation obtained from the QC framework with the SOS method.

6.5 Largest permissible perturbations using spherical and ellipsoidal sets

In this section, we obtain the estimates for the largest permissible perturbation for the Burgers system using the QC framework with constraints generalized to both spherical and ellipsoidal constraints.

6.5.1 Largest Permissible perturbations over spherical sets

First, the spherical constraints have to be obtained for the reduced-order Burgers system. As shown in Eq. (5.1), the local constraints for reduced-order Burgers system on spherical sets are given as

$$M_i^{\text{Sph}}(\alpha) = \begin{bmatrix} \alpha^2 \rho(\tilde{Q}_i)^2 I & \underline{0} \\ \underline{0} & -\mathbf{e}_i \mathbf{e}_i^T \end{bmatrix}, \text{ for } i = 1, \cdots, r. \tag{6.9}$$

The spherical constraints are used to solve Eq. (4.21), to obtain the estimate of the largest R using spherical sets.

6.5.2 Largest permissible perturbation over ellipsoidal sets

To improve over the estimates obtained from spherical sets, we now use the elliptical sets. The elliptical constraints for the Burgers system are as follows:

$$M_i^{\mathrm{Ell}}(\alpha, E) = \begin{bmatrix} \alpha^2(\tilde{Q}_i E^{-1} \tilde{Q}_i) & \underline{0} \\ \underline{0} & -\mathbf{e}_i \mathbf{e}_i^T \end{bmatrix}, \text{ for } i = 1, \cdots, r. \tag{6.10}$$

To obtain estimates of the largest permissible perturbations, the following SDP is solved

$$\begin{aligned} \lambda^* := & \min_{P,\xi,\lambda} \lambda, \\ \text{subject to } . & \begin{bmatrix} A^T P + PA & P \\ P & \underline{0} \end{bmatrix} + \sum_{i=1}^{r} \xi_i M_i^{\mathrm{Ell}}(\alpha, E) \preceq \begin{bmatrix} -\epsilon I & \underline{0} \\ \underline{0} & \underline{0} \end{bmatrix}, \\ & \frac{1}{\alpha^2} E \leq P \leq \frac{1}{R^2} I, \\ & \xi_i \geq 0, \text{ for } i = 1, \cdots, r. \end{aligned} \tag{6.11}$$

The constraints in Eq. (6.11) are different from Eq. (5.7). In that, the nonlinear terms in the Burgers equations are not lossless, and hence the equation does not have global lossless constraints. Therefore, we are accounting only for the local properties of the nonlinear terms in the Burgers equations to obtain an estimate of the largest permissible perturbations.

Algorithm A solves the SDP in Eq. (6.11) over 3 steps of (i) initial estimate, (ii) refinement, and (iii) iterate, as shown in Algorithm A. The algorithm terminates after the estimate for R converges to a tolerance of 10^{-3}. Over the 3 steps in Algorithm A, we use 200 logarithmically spaced points between $\alpha_1 = 10^{-1}$ and $\alpha_{200} = 10^{1}$ to solve the SDP in (6.11). From fig. 6.3, it can be seen that the constraints generalized on ellipsoidal sets improve the estimates of R^* by approximately an order of magnitude compared to the constraints on spherical sets. In the Burgers system, it is observed that the gap between R^* obtained from the constraints on spherical sets and constraints on elliptical sets is small at low Re. However, as the Re increases, we see that the constraints on

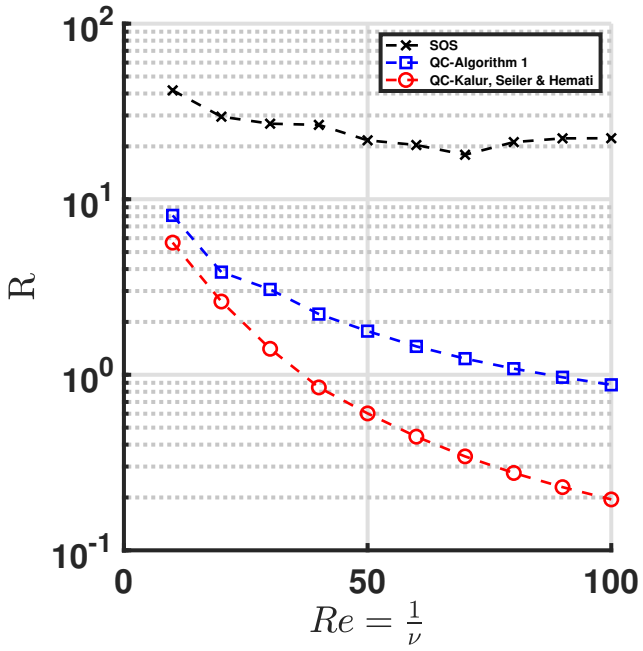

Figure 6.3: The figure shows the largest permissible perturbations obtained from the quadratic constraint framework and sum-of-squares method. It is seen that the constraints on elliptical sets provide a significant improvement over constraints on spherical sets.

ellipsoidal sets show improved estimates than those on spherical sets. This becomes important when analyzing the Burgers systems at larger Re, as we get much improved estimates at higher Re. Finally, we compare the results from the QC framework with the SOS method. The SOS method also uses Lyapunov functions of the system like the QC framework proposed herein. The reduced-complexity modeling of nonlinear terms via the QC framework shows an evident conservatism in the estimates of R^* when we compare with the SOS method. However, the SOS method requires the exact nonlinear dynamics, while the QC framework requires only input-output constraints of the nonlinear terms. As seen earlier in chapter 5, the QC method provides improved estimates significantly reduced computational costs compared to the SOS method, the same is true for estimating the largest permissible perturbations on the Burgers equations.

6.6 Conclusions

This chapter shows that we can apply the quadratic constraints framework to nonlinear partial differential equations such as the Burgers equation. The Burgers equation is chosen as it is a gateway towards more complex PDEs such as the NSE. At first, discretize the Burgers PDE using central-difference approximations to obtain a set of representative ODEs. While we get a good approximation of the PDE using central difference approximation, it is observed that the resulting system is still large for applying the QC framework. Hence, we obtain reduced-order models of the Burgers system by performing a Galerkin-projection onto the POD basis. The resulting reduced-order system requires only 5 modes to capture the dynamics of the original Burgers system. After model reduction, the system is now amenable to apply the QC framework proposed herein.

After a ROM is obtained, a local stability analysis is performed using the QC framework. The largest permissible perturbation analysis is performed using constraints generalized on spherical and ellipsoidal sets. The analysis shows us that the nonlinear terms have a destabilizing effect as the Re increases; since the permissible perturbation amplitude shrinks with an increase in the Re. The ellipsoidal constraints are shown to improve the estimates in comparison to constraints generalized on spherical sets. Lastly, the QC frameworks estimate of the largest permissible perturbation is compared with the SOS method. As expected, the QC framework provides a conservative estimate although at a significantly reduced computational cost.

Chapter 7

Conclusion and Future Directions

The NSE, which govern fluid flows, are high dimensional and have complex nonlinear interactions (which are not well understood). The sub-critical transition has been observed in wall-bounded shear flows, both in numerical simulations and experiments. This sub-critical transition is attributed to both the linear and nonlinear part, which cause non-modal growth and induces secondary instabilities, respectively. The focus of this thesis is to delay, suppress and understand the process of transition. To enable delaying or suppressing transition, we develop control-oriented reduced-order models in chapter 3. These reduced-order models enable developing controllers to minimize the MTEG caused by the non-modal growth in the linear part. These controllers that minimize MTEG are computationally expensive and require memory of the order$O(n^6$, where n is the dimension of the system. Hence, the MTEG minimizing controllers are not readily useable on the full-order original systems, and hence reduced-order models are necessary. Therefore, in chapter 3, we propose a reduced-order modeling method that enables the implementation of the MTEG minimizing controllers. Developing these ROMs is not trivial since MTEG is directly related to systems energy related to the states.To overcome this, we use output projection, i.e., using POD coefficients as the output and defining energy based on the output—thereby retaining energy definition after truncating states. We then later investigate the efficacy of the ROMs in modeling the FOM and show that a ROM with $40 - 60$ states (depending on specific configuration) does a good job of mimicking the FOM of 199 states. We show that the controllers developed using this ROM method effectively minimize MTEG compared to optimal

control strategies like LQR. Lastly, we also analyze the flow physics by investigating how the controller changes the flow field after minimizing MTEG. Therefore, chapter 3 addresses the problem of large dimensions by developing ROMs. Chapters 4 and 5, addresses the challenge of accounting for the complex nonlinear terms with reduced complexity. As mentioned earlier, these nonlinear terms introduce secondary instabilities and understanding how these nonlinear terms affect the system's stability is the aim of the next chapters. In chapter 4, this work introduces the quadratic constraints framework, where the stability analysis problem accounts for the nonlinear terms by using its input-output properties as quadratic constraints appended to Lyapunov matrix inequalities. In chapter 4, the quadratic constraints are generalized to spherical sets. We estimate the region of attraction, size of the largest permissible perturbations, MTEG the system holds, and uncover underlying physics using the Lagrange multiplier analysis. It is also observed that the quadratic constraints generalized to spherical sets are conservative in their estimates, and this is improved upon in chapter 5.

Chapter 5 introduces the quadratic constraints generalized to ellipsoidal sets—which reduce conservatism. This is demonstrated by analyzing the region of attraction and size of the largest permissible perturbations. However, generalizing these constraints to ellipsoidal sets introduces a bi-linearity in the Lyapunov matrix inequalities. To overcome this, we propose two algorithms that enable solving the matrix inequalities. The algorithms proposed to solve the matrix inequalities iteratively and to use a one-shot approach, respectively. We show that the one-shot algorithm provides estimates at a reduced computational cost compared to the iterative algorithm, albeit offering slightly conservative estimates compared to the iterative method. Lastly, we also compare the performance of the proposed framework with that of the SOS method and DAL method. It is demonstrated that the quadratic constraints framework though conservative in its estimates (in comparison to SOS and DAL methods), the proposed method surpasses both the SOS and DAL method in terms of computational run-time, especially for high dimensional systems.

In Chapter 6 of this thesis, we apply the proposed quadratic framework on the viscous Burgers PDE. We show how the stability of the nonlinear PDEs can be studied using the proposed QC framework. For analyzing the stability of nonlinear PDEs, it is found that the need to address both challenges that motivate this thesis, i.e., the

challenge of (i) dimensionality reduction and (ii) reduced-complexity modeling so that nonlinear terms are accounted for. First, we use finite-difference approximation techniques such as central differencing to convert the PDE into a set of representative ODEs. The resulting ODEs are still typically high dimensional in nature; this makes application o the QC framework intractable. Therefore, we perform POD-based model reduction to obtain a low-dimensional representation of the original system. Once the ROM of the Burgers system is obtained, we then apply the QC framework on the ROM-Burgers system to account for the nonlinear terms in a reduced-complexity setting. We study the stability of the Burgers system by analyzing the ROA and largest permissible perturbations of the system using both constraints generalized on spherical sets and ellipsoidal sets. As seen earlier, we observe that the constraints generalized on the ellipsoidal sets improve the estimates of the ROA and largest permissible perturbations compared to the constraints on spherical sets. Finally, we compare the largest permissible perturbations obtained from the QC framework with computationally cumbersome but more accurate SOS methods. As expected, the QC framework, which uses only input-output properties of the nonlinear terms, provides estimates at a reduced computational cost. The estimates by the QC framework are conservative since the exact nonlinear dynamics of the system are not used to compute the previously mentioned stability margins.

7.1 Future Directions

It may still be possible to refine the quadratic constraints method beyond what is presented in this study. Future work may benefit from incorporating additional constraints to refine the proposed QC analysis even further. Additional constraints capture the properties of the nonlinear terms or even exploit certain properties in terms of structure like sparsity, repeating patterns, and pathways in which energy is transferred or exchanged between various terms.

The general QC framework proposed here shows promise in analyzing complex systems with quadratic and lossless nonlinearities, such as the incompressible NSE. The wall-bounded shear flows, especially the channel flow problem, have been shown to have a lossless nonlinear term. It is of great interest to extend this quadratic constraint framework to such complex fluid flows. When extended to time-varying fluid flows, the

quadratic constraint framework will form integral quadratic constraints [MR97]. Extending this to complex flows like the channel flow system is complicated and beyond the scope of this work. However, it should be noted that computational challenges are involved in generalizing this quadratic-constraint-based analysis for high-dimensional fluids systems. The primary hurdle rests in the fact that computational demands of general-purpose solvers for the convex optimization methods proposed here scale with $\mathcal{O}(n^6)$, where n is the state dimension [BV04]. Potential avenues forward may rely upon accurate reduced-order models, dedicated solvers, or some combination thereof. Nonetheless, the ideas proposed here establish exciting avenues for fluid flow analysis that—with further development—are expected to provide valuable insights about complex flow physics.

Many complex systems are difficult to model from first principles, e.g., combusting and reacting flows in engines, rotating detonation engines, single-injector rocket combustion, etc. Towards developing models for these complex systems, a lot of work has been done in data-driven nonlinear reduced-order modeling to learn the system operators, especially for systems with polynomial nonlinearities. The proposed quadratic constraints framework can be easily extended to analyze systems inferred from data-driven approaches and also provides guaranteed stability margins for operation and ensures robustness.

Traditionally controller verification for larges systems like fluid flows is an expensive process, as multiple expensive high fidelity simulations in various configurations have to be performed to ensure the controllers designed are robust to factors like various initial conditions, a wide range of parameters, etc. The proposed quadratic constraint framework has been shown to help in situations where controller verification is necessary. In addition to the stability analysis, the quadratic constraint framework can develop controllers on the nonlinear system like the incompressible NSE. The quadratic constraint framework has shown promise for controller verification, in [MSH21] the controllers' performance is verified over various parameter ranges in the nonlinear system using the quadratic constraint framework. This is exciting as it helps to verify controller performance, with guaranteed bounds, without running expensive computational simulations.

Bibliography

[AM15] Farshid Abbasi and Javad Mohammadpour. Nonlinear model order reduction of burgers' equation using proper orthogonal decomposition. *American Control Conference, Chicago*, 2015.

[ApS19] MOSEK ApS. *The MOSEK optimization toolbox for MATLAB manual. Version 9.0.*, 2019.

[ASG06] A C Antoulas, D C Sorensen, and S Gugercin. A survey of model reduction methods for large-scale systems. Technical report, 2006.

[AVGaP19] Mohamadreza Ahmadi, Giorgio Valmorbida, Dennice Gayme, and antonis Papachristodoulou. a framework for input-output analysis of wall-bounded shear flows. *Journal of Fluid Mechanics*, 2019.

[BEFB94a] S Boyd, L El Ghaoui, E Feron, and V Balakrishnan. *Linear Matrix Inequalities in System and Control Theory*, volume 15. 1994.

[BEFB94b] Stephen Boyd, Laurent El Ghaoui, Eric Feron, and Venkataramanan Balakrishnan. *Linear Matrix Inequalities in System and Control Theory*. Society for Industrial and Applied Mathematics, jan 1994.

[Bew01] Thomas R. Bewley. Flow control: New challenges for a new Renaissance. *Progress in Aerospace Sciences*, 37(1):21–58, 2001.

[BF92] Kathryn M. Butler and Brian F. Farrell. Three-dimensional optimal perturbations in viscous shear flow. *Physics of Fluids A: Fluid Dynamics*, 4(8):1637–1650, aug 1992.

[BG93] Stephen Boyd and Laurent El Ghaoui. Method of centers for minimizing generalized eigenvalues. *Linear Algebra and Applications, special issue on Linear Algebra in Systems and Control*, 1993.

[BH11] S Bagheri and D S Henningson. Transition delay using control theory. *Philosophical Transactions: Mathematical, Physical and Engineering Sciences*, 369, 2011.

[BHL93] Gal Berkooz, Philip Holmes, and John L Lumley. The proper orthogonal decomposition in the analysis of turbulent flows. Technical report, 1993.

[BL18] Thomas R Bewley and Sharon Liu. Optimal and robust control and estimation of linear paths to transition. *Journal of Fluid Mechanics*, 365:305–349, 2018.

[Bla99] F. Blanchini. Set invariance in control. *Automatica*, 35(11):1747 – 1767, 1999.

[Boy00] John P Boyd. *Chebyshev and Fourier Spectral Methods*. Dover Publications, 2000.

[BPST] G. Balas, A. Packard, P. Seiler, and U. Topcu. Robustness analysis for nonlinear systems.

[BSS12] A. Barbagallo, D. Sipp, and P. J. Schmid. Reduced order models for closed loop control: Comparison between pod, bpod, and global modes. *Progress in Flight Physics*, 3:503–512, 2012.

[BT97] Jeffrey S. Baggett and Lloyd N. Trefethen. Low-dimensional models of subcritical transition to turbulence. *Physics of Fluids*, 1997.

[BV04] Stephen Boyd and Lieven Vandenberghe. *Convex optimization*. Cambridge University Press, 2004.

[CF21] Ryan James Caverly and James Richard Forbes. Lmi properties and applications in systems, stability, and control theory, 2021.

[Cha02] S. J. Chapman. Subcritical transition in channel flows. *Journal of Fluid Mechanics*, 451:35–97, 2002.

[Che84] Chi-Tsong Chen. *Linear System Theory and Design*. CBS College publishing, 1984.

[CL19] Andrew Chavarin and Mitul Luhar. Resolvent Analysis for Turbulent Channel Flow with Riblets. *AIAA Journal*, 2019.

[Dam16] Christopher J. Damaren. Laminar-turbulent transition control using passivity analysis of the orr-sommerfeld equation. *Journal of Guidance, Control, and Dynamics*, 39(7):1602–1613, 2016.

[Dam19] Christopher J. Damaren. Transition control of the Blasius boundary layer using passivity. *Aerospace Systems*, 2(1):21–31, 2019.

[Gal10] Jean Gallier. The Schur complement and symmetric positive semidefinite (and Definite) matrices. *Complement*, 2010.

[GB08] Michael Grant and Stephen Boyd. Graph implementations for nonsmooth convex programs. In V. Blondel, S. Boyd, and H. Kimura, editors, *Recent Advances in Learning and Control*, Lecture Notes in Control and Information Sciences, pages 95–110. Springer-Verlag Limited, 2008.

[GB14] Michael Grant and Stephen Boyd. CVX: Matlab software for disciplined convex programming, version 2.1. `http://cvxr.com/cvx`, March 2014.

[GC12] P. J. Goulart and S. Chernyshenko. Global stability analysis of fluid flows using sum-of- squares. *Physica D*, 241:692–704, 2012.

[GN93] Pascal Gahinet and Arkadii Nemirovskii. General-purpose LMI solvers with benchmarks. In *Proceedings of the IEEE Conference on Decision and Control*, 1993.

[HBH03] Markus Hogberg, Thomas R. Bewley, and Dan S Henningson. Linear feedback control and estimation of transition in plane channel flow. *Journal of Fluid Mechanics*, 481:149–175, 2003.

[Hem06] Maziar S. Hemati. *Vortex-Based Aero- and Hydrodynamic Esimation*. PhD thesis, Univeristy of California, Los Angeles, 2006.

[Hen96] Dan Henningson. Comment on transition in shear flows. nonlinear normality versus non-normal linearity. *Physics of Fluids*, 1996.

[HJ90] Roger A. Horn and Charles R. Johnson. *Matrix analysis*. Cambridge University Press, 1990.

[HJS16] Peter H Heins, Bryn Ll Jones, and Ati S Sharma. Passivity-based output-feedback control of turbulent channel flow. *Automatica*, 69:348–355, 2016.

[HR94] Dan S. Henningson and Satish C. Reddy. On the role of linear mechanisms in transition to turbulence. *Physics of Fluids*, 6(3):1396–1398, mar 1994.

[HWR14] Maziar S. Hemati, Matthew O. Williams, and Clarence W. Rowley. Dynamic mode decomposition for large and streaming datasets. *Physics of Fluids*, 26(11), 2014.

[HY18] Maziar S. Hemati and Huaijin Yao. Performance Limitations of Observer-Based Feedback for Transient Energy Growth Suppression. *AIAA Journal*, 2018.

[IR08a] Miloš Ilak and Clarence W Rowley. Feedback control of transitional channel flow using balanced proper orthogonal decomposition. *AIAA Theoretical Fluid Mechanics Conference, Seattle, WA, AIAA paper 2008-4230*, 2008.

[IR08b] Miloš Ilak and Clarence W Rowley. Modeling of transitional channel flow using balanced proper orthogonal decomposition. *Physics of Fluids*, 20:34103, 2008.

[JB05] Mihailo R. Jovanović and Bassam Bameih. Componentwise energy amplification in channel flows. *Journal of Fluid Mechanics*, 534:145–183, jun 2005.

[JHK+15] Bryn Ll Jones, P H Heins, E C Kerrigan, J F Morrison, and A S Sharma. Modelling for robust feedback control of fluid flows. *Journal of Fluid Mechanics*, 769:687–722, 2015.

[JJW91] Slotine Jean-Jacques and Li Weiping. *Applied Nonlinear Control*. Prentice-Hall, 1991.

[Jos76] D. D. Joseph. *Stability of fluid motions I*. Springer-Verlag, New York, 1976.

[JSK99] Sanjay S Joshi, Jason L Speyer, and John Kim. Finite Dimensional Optimal Control of Poiseuille Flow. *Journal of Guidance, Control, and Dynamics*, 22(2), 1999.

[JSN14] Mihailo R. Jovanović, Peter J. Schmid, and Joseph W. Nichols. Sparsity-promoting dynamic mode decomposition. *Physics of Fluids*, 26(2):024103, feb 2014.

[KB07] John Kim and Thomas R. Bewley. A linear systems approach to flow control. *Annual Review of Fluid Mechanics*, 39(1):383–417, 2007.

[Ker18] R.R. Kerswell. Nonlinear nonmodal stability theory. *Annual Review of Fluid Mechanics*, 2018.

[Kha02] Hassan K. Khalil. *Nonlinear systems*. Prentice Hall, 2002.

[KPW14] R. R. Kerswell, C. C.T. Pringle, and A. P. Willis. An optimization approach for analysing nonlinear stability with transition to turbulence in fluids as an exemplar. *arXiv:1408.3539*, 2014.

[KSH20] A. Kalur, P. Seiler, and M.S. Hemati. Stability and performance analysis of nonlinear and non-normal systems using quadratic constraints. *AIAA Aerospace Sciences Meeting, AIAA Paper 2020-0833*, Jan 2020.

[KSH21] A. Kalur, P. Seiler, and M. Hemati. Nonlinear stability analysis of transitional flows using quadratic constraints. *Physical Review Fluids*, 6:044401, 2021.

[LG20] Chang Liu and Dennice F. Gayme. Input-output inspired method for permissible perturbation amplitude of transitional wall-bounded shear flows. *Phys. Rev. E*, 102:063108, Dec 2020.

[LHPW87] A Laub, M Heath, C Paige, and R Ward. Computation of system balancing transformations and other applications of simultaneous diagonalization algorithms. *IEEE Transactions on Automatic Control*, 32(2):115–122, feb 1987.

[Lum67] J. L. Lumley. The structure of inhomogeneous turbulent flows. *In Atmospheric Turbulence and Radio Wave Propagation (A. M. Yaglom and V. I. Tatarsky eds.)*, 1967.

[McK06] John McKernan. *Control of Plane Poiseuille Flow: A Theoretical and Computational Investigation.* PhD thesis, Cranfield University, 2006.

[MFE04] Jeff Moehlis, Holger Faisst, and Bruno Eckhardt. A low-dimensional model for turbulent shear flows. *New Journal of Physics*, 6:56–56, May 2004.

[Moo81] B. Moore. Principal component analysis in linear systems: Controllability, observability, and model reduction. *IEEE Transactions on Automatic Control*, 26(1):17–32, feb 1981.

[MPW06] John McKernan, George Papadakis, and James F. Whidborne. A linear state-space representation of plane Poiseuille flow for control design: a tutorial. *International Journal of Modelling, Identification and Control*, 1(4):272, 2006.

[MQMW11] F Martinelli, M Quadrio, J Mckernan, and J F Whidborne. Linear feedback control of transient energy growth and control performance limitations in subcritical plane Poiseuille flow. *Physics of Fluids*, 2011.

[MR97] Alexandre Megretski and Anders Rantzer. System Analysis via Integral Quadratic Constraints. Technical Report 6, 1997.

[MS10] B. J. McKeon and A. S. Sharma. A critical-layer framework for turbulent pipe flow. *Journal of Fluid Mechanics*, 2010.

[MSH21] T. Mushtaq, Peter Seiler, and Maziar Hemati. Feedback control of transitional flows: A framework for controller verification using quadratic constraints. *AIAA Conference*, 2021.

[Par00] Pablo A. Parillo. *Structured Semidefinite Programs and Semialgebraic Geometry Methods in Robustness and Optimization.* PhD thesis, California Institute of Technology, 2000.

[PH69] V C Patel and M R Head. Some observations on skin friction and velocity profiles in fully developed pipe and channel flows. *Journal of Fluid Mechanics*, 38(1):181–201, 1969.

[PP05] A. Papachristodoulu and S. Pranja. A tutorial on sum-of-squares technique for system analysis. *American Control Conference*, 2005.

[Pru86] John E. Prussing. The principal minor test for semidefinite matrices. *Journal of Guidance, Control, and Dynamics*, 9(1):121–122, 1986.

[RD17] Clarence W Rowley and Scott T M Dawson. Model Reduction for Flow Analysis and Control. *Annual Review of Fluid Mechanics*, 49:387–417, 2017.

[RH93a] Satish C. Reddy and Dan S. Henningson. Energy growth in viscous channel flows. *Journal of Fluid Mechanics*, 252(-1):209, jul 1993.

[RH93b] Satish C. Reddy and Dan S. Henningson. Energy growth in viscous channel flows. *Journal of Fluid Mechanics*, 252(-1):209, jul 1993.

[RMB+09] Clarence W. Rowley, Igor Mezi, Shervin Bagheri, Philipp Schlatter, and Dan S. Henningson. Spectral analysis of nonlinear flows. *Journal of Fluid Mechanics*, 641:115–127, 2009.

[Row05] C W Rowley. Model reduction for fluids using balanced proper orthogonal decomposition. *Int. J. on Bifurcation and Chaos*, 15(3):997–1013, 2005.

[SB14] Peter J. Schmid and Luca Brandt. Analysis of Fluid Systems: Stability, Receptivity, SensitivityLecture notes from the FLOW-NORDITA Summer School on Advanced Instability Methods for Complex Flows, Stockholm, Sweden, 2013. *Applied Mechanics Reviews*, 66(2):021003, mar 2014.

[Sch07] Peter J Schmid. Nonmodal Stability Theory. *Annual Review of Fluid Mechanics*, 39:129–62, 2007.

[SH01] Peter J. Schmid and Dan S. Henningson. Eigensolutions to the Viscous Problem. pages 55–98. 2001.

[SH19] Yiyang Sun and Maziar S. Hemati. Feedback control for transition suppression in direct numerical simulations of channel flow. *Energies*, 12(21), 2019.

[SLC+19] Yiyang Sun, Qiong Liu, Louis N. Cattafesta, Lawrence S. Ukeiley, and Kunihiko Taira. Resolvent analysis of compressible laminar and turbulent cavity flows. sep 2019.

[SM13] A. S. Sharma and B. J. McKeon. On coherent structure in wall turbulence. *Journal of Fluid Mechanics*, 2013.

[SMML11] Ati Sharma, F. Morrison, J, B. J. McKeon, and W.H. Limebeer, D.J.N. Koberg. Relaminarisation of $re_t = 100$ channel flow with globally stabilising linear feedback control. *Physics of Fluids*, 2011.

[SP05] Sigurd. Skogestad and Ian. Postlethwaite. *Multivariable feedback control : analysis and design*. John Wiley, 2005.

[TBD+] Kunihiko Taira, Steven L Brunton, Scott T M Dawson, Clarence W Rowley, Tim Colonius, Beverley J Mckeon, Oliver T Schmidt, Stanislav Gordeyev, Vassilios Theofilis, and Lawrence S Ukeiley. Modal Analysis of Fluid Flows: An Overview.

[TE05] Lloyd N. (Lloyd Nicholas) Trefethen and Mark Embree. *Spectra and pseudospectra : the behavior of nonnormal matrices and operators*. Princeton University Press, 2005.

[THB+19] Kunihiko Taira, Maziar S. Hemati, Steven L. Brunton, Yiyang Sun, Karthik Duraisamy, Shervin Bagheri, Scott T. M. Dawson, and Chi-An Yeh. Modal Analysis of Fluid Flows: Applications and Outlook. mar 2019.

[TRS90] J. J. Thibert, J. Reneaux, and V. Schmitt. ONERA Activities on Drag Reduction. In *17th Congress of International Council of Aeronautic Science*, pages 1053–64, Stockholm, 1990. ICAS.

[TTRD93] L N Trefethen, A E Trefethen, S C Reddy, and T A Driscoll. Hydrodynamic stability without eigenvalues. *Science (New York, N.Y.)*, 261(5121):578–84, jul 1993.

[Tu13] Jonathan H Tu. Dynamic Mode Decomposition : Theory and Applications. (September):1–141, 2013.

[WA11] James F. Whidborne and Nathalie Amar. Computing the maximum transient energy growth. *BIT Numerical Mathematics*, 51(2):447–457, jun 2011.

[Wal95a] Fabian Waleffe. Hydrodynamic stability and turbulence: beyond transients to a self-sustaining process. *Studies in Applied Mathematics*, 1995.

[Wal95b] Fabian Waleffe. Transition in shear flows. Nonlinear normality versus non-normal linearity. *Physics of Fluids*, 7(12):3060–3066, 1995.

[WKH93] Fabian Waleffe, John Kim, and J. Hamilton. On the origins of streaks in turbulent shear flows. *Turbulent Shear Flows Springer*, 1993.

[WM07] James F. Whidborne and John McKernan. On the Minimization of Maximum Transient Energy Growth. *IEEE Transactions on Automatic Control*, 52(9):1762–1767, sep 2007.

[WP02] K Willcox and J Peraire. Balanced Model Reduction via the Proper Orthogonal Decomposition. *AIAA JOURNAL*, 40(11), 2002.

[YH18] H. Yao and M. S. Hemati. Revisiting the separation principle for improved transition control. *AIAA Paper 2018-3693*, 2018.

[YH19] Huaijin Yao and Maziar S Hemati. Advances in Output Feedback Control of Transient Energy Growth in a Linearized Channel Flow. *AIAA Paper 2019-0882*, 2019.

Appendix A

Sum-of-squares (SOS) Method

Parillo [Par00] introduced the sum-of-squares (SOS) technique to analyze nonlinear systems using Lyapunov methods. As we have briefly discussed earlier, Lyapunov methods are robust methods upon which nonlinear systems theory is built upon. Parillo, in his work, identified that the SOS technique generalizes to solving LMIs, which can be solved with existing well-known algorithms that run in polynomial time [BEFB94a]. The SOS technique formulates the problems in terms of polynomials, which can be represented as SDPs.

The stability problem of a system $\mathbf{x} = f(\mathbf{x})$ is taken as an example to illustrate the SOS technique. As discussed in Theorem 1, the above system is stable if there exists a $V(\mathbf{x}) > 0$ such that $\dot{V}(\mathbf{x}) \leq 0$ and this is equivalent to finding a P such that $A^T P + PA < 0$ for a system $\mathbf{x} = A\mathbf{x}$. The associated Lyapunov function then is given by $V(\mathbf{x}) = \mathbf{x}^T P \mathbf{x}$ and therefore both V and $\dot{V}$ are SOS as seen from the definition below.

Definition 3. *For $x \in \mathbb{R}^n$, a multivariable polynomial $p(x)$ is SOS if there exists some polynomial $f_i(x),\ i = 1, \cdots, n$ such that $p(x) \sum_{i=1}^{n} f_i(x)^2$.*

When $f(x)$ and V are polynomials, then the problem to check for non-negativity is NP-hard [PP05]. However, the non-negativity condition can be replaced by the SOS condition—this enables both testing and constructing a Lyapunov function—which is solved as an SDP feasibility problem.

Proposition 1. *[Par00] $p(x)$ is SOS if and only if there exists a $Q = Q^T \geq 0$ and a vector $\mathbf{w}(x)$ such that $p(x) = \mathbf{w}(x)^T Q \mathbf{w}(x)$*

We illustrate this with an example taken from [PP05]. To identify if $p(x_1, x_2) = 2x_1^4 + 2x_1x^3x_2 - x_1^2x_2^2 + 5x^4$ is a SOS we define $\mathbf{w}(x) = \begin{bmatrix} x_1^2 & x_2^2 & x_1x_2 \end{bmatrix}$, following which we can write $p(x)$ in terms of $\mathbf{w}(x)^T Q \mathbf{w}(x)$ and the goal is to find a matrix Q that is positive semi-definite and satisfies the polynomial. This will give us a relation for elements of Q that have to be satisfied, the conditions to be satisfied are as follows,

$$\begin{aligned} q_{11} &= 2, \\ q_{22} &= 5 \\ q_{13} &= 1, \\ q_{23} &= 0, \\ 2q_{12} + q_{33} &= -1. \end{aligned}$$

Therefore searching for q_{12} and q_{33} that satisfies the relation is equivalent to identifying if $p(x)$ is SOS, which implies $p(x) \geq 0, \ \forall x \in \mathbb{R}^n$.

Conversion of SOS problems to SDPs can be performed manually; in general, they are cumbersome, and therefore software that aid such computations are necessary to automate this process. We use SOSOPT [BPST], a Matlab Toolbox for formulating and solving SOS polynomial optimizations in this work. The [BPST] toolbox enables analysis for nonlinear analysis problems such as computing regions of attractions, largest permissible perturbations, reachability sets, input-output gain for polynomial nonlinear systems.

Appendix B

Direct-adjoint looping Method

The direct-adjoint looping or DAL is a fully nonlinear optimization technique used to identify initial conditions that can trigger transition to another state—*an optimal perturbation*. Excellent overviews of the DAL method can be found in [KPW14, Ker18]. To explain the DAL technique used in this work, the article in [KPW14] is briefly summarized for the readers benefit.

Given perturbation dynamics of the form

$$\frac{d\mathbf{x}}{dt} = F(\mathbf{x} : X_0, \mu). \tag{B.1}$$

Here, the perturbations $\mathbf{x}$ is given about a stable equilibrium $\mathbf{X}_0$ such that $\mathbf{x} = \mathbf{X} - \mathbf{X}_0$, and $\mathbf{X} \in \mathbb{R}^n$ is the instantaneous state with μ as system parameter. The distance of $X(t)$ from X_0 is measured using the norm $\|\mathbf{x}(t)\| := \sqrt{\sum_{n=1}^{N} x_i^2}$. The DAL optimization process aims to maximize distance over all perturbations that begin at a distance d such that $\|\mathbf{x}(0)\| = d$. This maximum distance travelled by states of Eq. (B.1) is found for some time $t = T$. The problem of identifying the maximum distance and satisfying constraints of Eq. (B.1) and constraints of $\|\mathbf{x}(0)\| = d$ is obtained by maximizing the following Lagrangian

$$\mathcal{L} := \|\mathbf{x}(T)\|_2^2 + \int_0^T \nu \cdot \left(\frac{d\mathbf{x}}{dt} - F\right) dt + \lambda(\|\mathbf{x}(0)\|_2^2 - d^2). \tag{B.2}$$

With $\nu(t)$ and λ as Lagrange multipliers that impose the aforementioned constraints. To obtain the maximum value of $\mathcal{L}$, the following conditions have to be satisfied simultaneously [KPW14]

$$\frac{d\mathbf{x}}{dt} = F(\mathbf{x} : X_0, \mu), \tag{B.3}$$

$$\|\mathbf{x}\| = d, \tag{B.4}$$

$$\frac{d\boldsymbol{\nu}}{dt} + \boldsymbol{\nu} + \boldsymbol{\nu} \cdot \frac{\partial F}{\partial \mathbf{x}} = 0 \text{ for } t = (0, T), \tag{B.5}$$

$$2\lambda\mathbf{x}(0) - \boldsymbol{\nu}(0) = 2\mathbf{x}(T) + \boldsymbol{\nu}(T) = 0. \tag{B.6}$$

Since the system is nonlinear, the above conditions have to be solved iteratively. The following steps are used to obtain the largest perturbation that destabilizes a system.

1. Propagate the primal system in Eq. (B.1) with an initial guess $\mathbf{x}(0)$ to produce $\mathbf{x}(T)$.

2. Perform backward integration of the dual system $\frac{d\boldsymbol{\nu}}{dt} + \boldsymbol{\nu} = -\boldsymbol{\nu} \cdot \frac{\partial F}{\partial \mathbf{x}}$ from $t = T$ to $t = 0$.

3. Power-iteration method is used to find direction of maximum ascent of $\mathcal{L}$.

In this work, we repeat the DAL process for various disturbance size d. If a trajectory is found to be unstable, we perform bisection on d until we converge to a d^* that gives us the largest permissible perturbation to ensure that all system trajectories starting from $\|\mathbf{x}(0)\| = d^*$ are stable.